The Interaction of Oceanic Jets with the Midlatitude Storm Tracks

A thesis submitted for the degree of

Doctor of Philosophy of Imperial College London

by

Christopher H. O'Reilly

Department of Physics

Imperial College London

Blackett Laboratory, Prince Consort Road, London. SW7 2AZ

MAY, 2013

I certify that this thesis, and the research to which it refers, are the product of my own work, and that any ideas or quotations from the work of other people, published or otherwise, are fully acknowledged in accordance with standard referencing practices.

Signed:

Copyright

The copyright of this thesis rests with the author and is made available under a Creative Commons Attribution-Non Commercial-No Derivatives licence. Researchers are free to copy, distribute or transmit the thesis on the condition that they attribute it, that they do not use it for commercial purposes and that they do not alter, transform or build upon it. For any reuse or distribution, researchers must make clear to others the licence terms of this work.

Abstract

Two mechanisms through which oceanic jets and the atmospheric storm tracks interact in midlatitudes are considered. Firstly, the response of a two-layer ocean model to large-scale stochastic forcing, a simplified model of forcing by the North Atlantic Oscillation, is investigated. Long Rossby waves are excited at the eastern boundary of the square model basin and the waves are baroclinically unstable. A novel aspect is that the instability leads to the generation of zonal jets throughout the domain. Unlike other theories of jet generation, the jets are actually wave-like in nature, and result directly from the instability. The "jets" appear when averaging the zonal velocity field over fixed periods of time. The longer the averaging period, the weaker the jets as the latter are actually time-varying. The jets occur for a wide range of stochastic forcing strength and the presence or not of a time mean circulation. The mechanism described here thereby provides an explanation for the recent observations of alternating zonal jets.

The response of the Pacific storm track to the variability of the Kuroshio Extension jet is then studied. An index of the Kuroshio Extension front strength is produced using sea surface temperature and sea surface height observations. The index reflects the strengthening and weakening of the SST gradient associated with the bimodal states of the Kuroshio, and composites of the atmospheric state are presented during its positive and negative phases. The anomalous response of the transient eddy heat transport resembles a zonal dipole structure. With a weaker (stronger) SST front, the eddy heat transport is increased in the eastern (western) Pacific region, consistent with reduced (enhanced) low-level baroclinicity. The response of the large-scale atmospheric circulation is a barotropic blocking-type pattern in the east Pacific, which is interpreted in terms of the barotropic "eddy-straining" mechanism and eddy-mean flow interaction.

For Betty, Harry, Jim and Margaret

Acknowledgements

With certainty, I can say that without the advice, support and patience of Arnaud Czaja this thesis would not have been possible. Arnaud has afforded me more of his time and coffee than I have deserved; his open-mindedness and infectious enthusiasm have been a constant inspiration. I am indebted to Joe LaCasce for his QG model code and for numerous helpful ("virtual") discussions about the results. I am also thankful to the other members of the research group, past and present, who have all kindly listened to and *constructively* criticised many of my half-baked ideas, in particular Gabrielle Messori, Rhys Parfitt, Luke Sheldon, Iselin Medhaug, Ruth Geen, Chris Dancel and Ute Hausmann.

During my studies I have had a most enjoyable time, which is largely down to my office friends. James Farley Nicholls has been a great friend and distraction. Together we dreamt up various elaborate punts, in both partnership and opposition[1]. Cathy Ansell has been an absolute star and has dutifully put up with the highs and lows of both my research and afternoon "pick 'n' mix" sessions. She has also been my chief caffeine collaborator (e.g. "the coffee cup column", "the (dark) Tetley's period" etc.), keeping me up to date with The Daily Mail website and above all being an incredibly supportive friend. She can also now make an adequate brew. Daniel Jabry deserves gratitude for not getting frustrated with us leaving our caffeine paraphernalia on his desk and for generally being a top man. I am also thankful to Jack Cutler for keeping us all abreast of his upcoming novel and for his various tales, particularly one that forced me to spend a lot less time in the sauna, resulting in a much-needed productivity boost.

Away from The Huxley Building, I am grateful to my flat mates for what I have learned from them, putting up with me and for being good friends. I am thankful to Frederico Sanches for teaching me never to rush things, except in the kitchen; to the pyromaniac acid-

[1]Sadly John Kuhn didn't rush for exactly 5 yards in Super Bowl XLV, nor could I perform 100 press-ups after 4 weeks training.

spilling bone-cutter Gareth "Holcano" Hollis[2] for his reserved demeanour and humility; to David Bewick for teaching me, through the example of his seemingly boundless misogyny, that it is often only our ambition that limits us; to "The Zurry" for his humourous B.S. and limitless shisha.

Lastly, I am grateful for the support of my friends and family. In particular, I am thankful to Christine and John for all their love and support during my studies. They're the best.

[2]Holcano: an enduring flame, always explosive (Gareth Hollis, personal communication, 2013).

Table of contents

Abstract 4

Acknowledgements 6

1 Introduction 20

2 Background 23
2.1 Quasigeostrophic dynamics . . . 23
2.1.1 Quasigeostrophic scaling . . . 23
2.1.2 Two-layer quasigeostrophic equations . . . 26
2.1.3 Non-dimensional variables . . . 30
2.1.4 Rossby waves in two layers . . . 30
2.1.5 Two-layer baroclinic instability . . . 31
2.2 Zonal jets in the ocean . . . 38
2.3 The impact of the ocean on the midlatitude storm tracks . . . 44

3 Emergence of zonal ocean jets due to atmospheric forcing 53
3.1 Quasigeostrophic model setup . . . 53
3.1.1 Numerical model . . . 53
3.1.2 Large-scale atmospheric forcing . . . 54
3.2 Stochastic wind forcing simulations . . . 58
3.2.1 Fofonoff gyres and sponge layers . . . 58
3.2.2 Rossby basin modes . . . 61
3.2.3 Rossby wave instability . . . 64
3.2.4 Emergence of alternating zonal jets at surface . . . 68
3.2.5 Scale of jets and sensitivity to forcing amplitude . . . 70
3.3 Mean and stochastic wind forcing simulations . . . 76
3.3.1 Instantaneous and time-averaged flow . . . 76
3.3.2 Meridional tilt of zonal jets . . . 79

3.3.3 Comparison with mean-only simulations 80
3.4 Discussion and summary 82

4 Covariability of the Kuroshio Extension jet and SST front 85
4.1 Datasets 85
4.2 Maximum covariance analysis 87
4.3 Impact of geostrophic advection on anomalous SST fields 93
4.4 Covariability in other western boundary current regions 99
4.5 Summary 103

5 The response of the Pacific storm track and atmospheric circulation to Kuroshio variability 107
5.1 Data 108
5.2 Empirical relations between the Kuroshio Extension front and the atmospheric state 109
5.3 Interpretation as evidence of an atmospheric response to ocean variability . 121
5.4 Mechanisms 127
5.4.1 Zonal dipole in eddy heat transport 127
5.4.2 Blocking effect 129
5.4.3 Eddy-mean flow interaction 132
5.4.4 Further effects 136
5.5 Discussion and summary 137

6 Summary and future work 140
6.1 Summary 140
6.2 Future work 142
6.2.1 Oceanic zonal jets 142
6.2.2 Storm track response to other western boundary currents 142
6.2.3 Implications for blocking 145
6.2.4 Aquaplanet simulations 145
6.2.5 Coupled decadal variability in the North Pacific sector 145

References 161

Appendices 162

A Numerical quasigeostrophic basin model 163

B Rossby wave instability 169

List of Figures

1.1 Zonal velocity at 400m, in cm/s, averaged over 3 years in an eddy-resolving ocean general circulation model. (From Richards *et al.* (2006)). 20
1.2 Annual average eddy heat transport, $\overline{v'T'}$, at 850 hPa (using high-pass filtered data from the ERA Interim dataset). 21

2.1 Schematic of the two-layer model with flat bottom and rigid-lid approximation. 27
2.2 Schematic of two orientations of the interface in a two-layer stratified ocean and the available potential energy (APE). The circles mark the centre of mass in each layer in the case of a tilted interface, left, and a flat interface right. The flattening of the interface lowers the centre of mass in the lower layer and raises the centre of mass in the upper layer, corresponding to a release in potential energy due to the density difference between the layers. The flat interface is the minimum potential energy state of the system. . . . 32
2.3 18-week average of the zonal geostrophic velocity anomaly (relative to ten-year average), in cm/s, from the Aviso sea level dataset. (From Maximenko *et al.* (2005)). 38
2.4 Zonal velocity at 400m, in cm/s, averaged over 3 years in an eddy-resolving ocean general circulation model. (From Richards *et al.* (2006)). 39
2.5 Snapshots of decaying barotropic tubulence in the doubly-periodic model of Rhines (1975) with (a) $\beta = 0$ and (b) $\beta > 0$. The eddies that develop in the presence of non-zero β are zonally elongated. (From Rhines (1975)). 41
2.6 Time-averaged non-dimensional streamfunction from the barotropic basin simulations by Nadiga (2006). The simulations were forced with a small scale homogenous stochastic forcing and zero mean forcing. Zonal jets are seen to emerge from an inverse cascade similar to the simulations of Rhines (1975). (From Nadiga (2006)). 42

2.7 Bandpass filtered (2-7 days) standard deviation of the meridional flow at the 300mb pressure level from the NCEP-NCAR reanalysis. The contour interval is 2 ms^{-1}. (From Chang *et al.* (2002)). 44
2.8 Meridional heat transport (northward) as a function of latitude for the ocean (in grey) and atmosphere (in black), calculated from NCEP reanalyses (solid lines) and ECMWF reanalyses (dashed lines). (Reproduced from Czaja and Marshall (2006), who used data from Trenberth and Caron (2001)). 45
2.9 Eady growth rate for the Northern hemisphere winter mean at the 780 hPa level. The contour interval is 0.1 day^{-1} and values over 0.6 day^{-1} are stippled. Where the 780 hPa level is likely to be within the boundary layer (due to orography) the data is blacked out. (From Hoskins and Valdes (1990)). . . . 47
2.10 Climatology of the (shaded) austral winter turbulent surface heat flux (sensible and latent) and the (contoured) high-pass filtered eddy heat transport ($\overline{v'T'}$) at 850 hPa generated using JRA-25 reanalysis data. (From Nakamura *et al.* (2008)). 48
2.11 Geopotential height variance at 850 hPa in the aquaplanet experiment of Brayshaw *et al.* (2008) with zonally varying SSTs. The SST anomally added to a zonally uniform SST field is contoured (in degrees K) and the maximum SST gradient in this setup is located at 90°E and 40°N. (From Brayshaw *et al.* (2008)). 49
2.12 Behaviour of the yearly path of Kuroshio Extension, defined by the 170-cm contours in the weekly SSH fields, where the contour is plotted every 14 days. (From Qiu and Chen (2005)). 51

3.1 Leading empirical orthogonal function (EOF 1) of the winter (December-March) mean sea level pressure anomalies over the North Atlantic sector (20°-70°N, 90°W-40°E), and the percentage of the total variance explained. The contour increment is 0.5 hPa, and the zero contour has been excluded. (From Hurrell *et al.* (2003)). 55
3.2 Correlation coefficient between yearly NAO-index and zonal wind stress, τ_x. Contours are solid/dashed for positive/negative values and the contour interval is 0.2 with maximum values of 0.8. (From Visbeck *et al.* (2003)). . . 56
3.3 Schematic diagram of the "Z" model of Marshall *et al.* where the diagonal is the zero wind curl line of the climatology and the top and bottom lines are the zero wind curl lines of the NAO anomaly. The sense of the "intergyre gyre" spun up by positive NAO forcing is shown. (From Marshall *et al.* (2001)). 57

3.4 (a) Time-averaged non-dimensional upper-layer streamfunction for the simulation with stochastic forcing. (b) Snapshot of the non-dimensional upper-layer streamfunction after about 50 years of the simulation. (c) Snapshot of the non-dimensional barotropic streamfunction during the spin-up phase of the simulation (taken at about 10 years). (d) Meridional cross-section of the time-averaged non-dimensional barotropic potential vorticity, $\overline{\nabla^2\phi} + \beta y$, through the centre of the basin (where the dashed line indicates βy) 59

3.5 Schematic of the dissipative sponge layers employed in the north and south of the basin to prevent the spin-up of inertial recirculation gyres. A dissipation of $-\gamma q_i$ (where q_i is as defined in (2.20)) is applied that relaxes the PV towards βy. 61

3.6 Scatter plot of eigenvalues of the frequency from the linear reduced gravity study by Cessi and Primeau (2001) for both the "mass conserving" boundary condition and the $\psi = 0$ boundary condition in the presence of weak dissipation. The imaginary part of the frequency, ω_i, is the damping rate and the real part, ω_r, is the frequency of the Rossby wave oscillation. Allowing the streamfunction to vary on the boundary allows basin modes to be very weakly damped in comparison to other frequencies. (From Cessi and Primeau (2001)). 62

3.7 Frequency spectrum of the baroclinic streamfunction $|\hat{\tau}(\omega)|$ as measured at the centre of the basin. The basin mode frequencies the frequencies are $\omega_n \approx 0.055n$ (the frequencies of the first four modes are marked by the dashed lines). The streamfunction and frequency are both in non-dimensional model units. 63

3.8 Schematic of structure of first and second basin modes in the baroclinic streamfunction. Dashed contours are negative and solid contours are positive. The structure of the basin modes leads to associated flow which is predominantly meridional, whilst the waves also have a large extent in the zonal direction. 64

3.9 Snapshot of the non-dimensional baroclinic streamfunction in the reference stochastic-only forcing experiment. The Rossby waves emanating from the eastern boundary are see to develop instability where there is significant velocity shear. The black lines in the north and south of the basin indicates the positions of the dissipative sponge layers. 65

3.10 (a) Snapshot of the baroclinic stream function at the start of the averaging period. (b) Snapshot of the baroclinic stream function at the end of the averaging period, note the westward progression of the meridionally orientated Rossby waves and the pertubations that have developed. (c) The zonal "heat transport" average, $\overline{u'\tau'}$, in the period between the snapshots in (a) and (b). (d) the meridional integral of the zonal heat transport average shown in (c). 67

3.11 Maps of the upper-layer zonal velocity anomaly, u_1' (cm/s), in the stochastic forcing simulations for (a) snapshot, (b) 20-week average, (c) 200-week average and (c) 500-week average for the simulation with stochastic-only forcing. The bold black lines mark the edge of the dissipative sponge layers. 69

3.12 Map of the 200-week average of the non-dimensional upper-layer streamfunction, ψ_1. The averaging in time causes the zonal tongues that develop on the large scale Rossby wave to blur as they transit the basin, resulting in bands of alternating zonal motion. The bold black lines mark the edge of the dissipative sponge layers. 70

3.13 Meridional wavenumber spectra of the 200-week mean upper-layer velocity anomaly in the stochastic forcing simulations with $\sigma_{W_s} = \sigma_{\text{ref}}$ (blue), $\sigma_{W_s} = 0.2\,\sigma_{\text{ref}}$ (green), $\sigma_{W_s} = 0.4\,\sigma_{\text{ref}}$ (red), $\sigma_{W_s} = 2.5\,\sigma_{\text{ref}}$ (black) and $\sigma_{W_s} = 5\,\sigma_{\text{ref}}$ (magenta). The shaded area shows the standard deviation of the independent spectra used to produce each mean spectrum. 71

3.14 Plot of the jet wavelength, λ_{jet}, for various values of the deformation radius, L_d, for the stochastic-only forcing experiments. The wavelength of the jets is taken from the peak of the meridional wavenumber spectra (e.g. Figure 3.13). 72

3.15 Ratio of barotropic kinetic energy to baroclinic potential energy in the stochastic-only forcing experiments for various values of the Ekman pumping standard deviation, σ_{W_s}. The larger ratios indicate that there is a cascade of energy to the barotropic mode with increased forcing. The time is in non-dimensional model units. 74

3.16 Snapshot of the baroclinic streamfunction, τ, in the mean and stochastic forcing simulation. The baroclinic Rossby waves can be seen emanating from the Eastern boundary and being "bent" by the barotropic advection. Zonal tongues similar to those observed in the stochastic-only simulations are apparent in the middle part of the large scale gyres. 75

3.17 20-week average of the non-dimensional baroclinic streamfunction anomaly, τ', in the mean and stochastic forcing simulation. The development of tongues (slightly tilted from the purely zonal tongues in the stochastic-only simulations) is visible on the large-scale Rossby wave which is noticably doppler-shifted by the double-gyre mean flow. 77

3.18 Map of the upper-layer zonal velocity anomaly, u_1' (cm/s), in the mean and stochastic forcing simulation averaged over 200 weeks. The mean barotropic streamfunction (averaged over the 115-year model integration) is plotted with a contour interval of 8×10^3 m^{2}s^{-1} and the solid and dashed contours indicate positive and negative values respectively, with the zero contour in bold. . . 78

3.19 Map of the upper-layer zonal velocity anomaly, u_1' (cm/s), in the mean and stochastic forcing simulation averaged over 200 weeks. The mean lower layer potential vorticity, Q_2, is contoured. 80

3.20 (a) Map of the upper-layer zonal velocity anomaly, u_1' (cm/s), in the simulation with mean-only forcing, averaged over 200 weeks. (b) Map of the mean non-dimensional baroclinic streamfunction, $\overline{\tau}$, in the simulation with mean-only forcing. (c) and (d) are the same as (a) and (b) respectively but for the mean and stochastic forcing simulation. 81

4.1 The magnitude of the SST gradient, in units of °C/100km, averaged over the boreal winter of 2004 (i.e. the average of the gradient magnitude, $\overline{|\nabla T|}$) from the optimally-interpolated AMSR-AVHRR daily SST dataset (Reynolds, 2007). 87

4.2 The magnitude of the surface geostrophic velocity, in units of cm/s, corresponding averaged over the boreal winter of 2004 (i.e. the average of the velocity magnitude, $\overline{|\mathbf{u}_g|}$) calculated from the SSH fields in the AVISO daily altimetry dataset. 88

4.3 The first mode patterns from the MCA of the surface geostrophic velocity magnitude, $|\mathbf{u}_g|(x, y, t)$, and the SST gradient magnitude , $|\nabla T|(x, y, t)$. The velocity pattern ($\mathbf{U}_1$) is contoured at intervals of 5 cm/s (positive in black, negative in gold) and the SST gradient pattern ($\mathbf{T}_1$) is shaded in units of °K/100km, each being equivalent to one standard deviation of the variability. The first ten singular values from the singular value decomposition are plotted and the squared covariance fraction (SCF) is indicated. The corresponding time series time series of the first mode of the MCA, $a_1(t)$, is plotted below (where the time series has been normalised by one standard deviation). . . 89

4.4 The magnitude of the SST gradient, in units of °C/100km, corresponding the positive phase (left) and negative phase (right) of the Kuroshio Extension variability (i.e. the mean plus/minus one standard deviation of the MCA pattern). 91
4.5 Plot of the squared covariance (SC) explained by the first mode of the maximum covariance analysis for the SST field lagging the geostrophic velocity by varying lead-lag periods (i.e. negative lag is where the SST field leads the velocity field) 92
4.6 The averaged temperature anomaly, $\langle T' \rangle$, in °C (relative to a time-varying mean as defined in the text) for (a) the positive phase and (b) the negative phase of the Kuroshio Extension front index. The box outlined with the bolds dashed line indicated the region of maximum response which was used for the heat flux divergence integral calculation. 95
4.7 The temperature field associated with each phase of the Kuroshio Extension front index generated by adding the temperature anomaly fields shown in Figure 4.6 to the climatology over the SST data period, for (a) the positive phase and (b) the negative phase. 96
4.8 The anomalous geostrophic advection term, $\langle (\mathbf{u} \cdot \nabla T)' \rangle$, in K/s averaged over (a) the positive phase and (b) the negative phase of the Kuroshio Extension front index. 97
4.9 Scatter plot of the values of $\langle T' \rangle$ (i.e. Figure 4.6) and $\langle (\mathbf{u}_g \cdot \nabla T)' \rangle$ (i.e. Figure 4.8) at each point in the region 34-37°N and 142-150°E for the positive phase (in red) and the negative phase (in blue). 98
4.10 (a) The long-term mean SST gradient magnitude, $\overline{|\nabla T|}$, and (b) the long-term mean of the geostrophic velocity magnitude, $|\mathbf{u}_g|$, for the Gulf Stream region over the full MCA period, 2002-2011. 100
4.11 As in Figure 4.3 but for the Gulf Stream region. The year labels indicate the beginning of that year. 101
4.12 Power spectrum of the time series $a_1(t)$ from the Gulf Stream MCA shown in Figure 4.11. 102
4.13 Lag correlation between the monthly averaged timeseries $a_1(t)$ from the Gulf Stream MCA and the NAO index, here the dotted line indicates the 5% level for no-correlation and independent samples. 103
4.14 (a) The long-term mean SST gradient magnitude, $\overline{|\nabla T|}$, and (b) the long-term mean of the geostrophic velocity magnitude, $|\mathbf{u}_g|$, for the Agulhas region over the full MCA period 2002-2011. 104

4.15 As in Figure 4.3 but for the Agulhas region, although here the velocity magnitude contours are every 2.5 cm/s (positive in green, negative in gold and the zero contour is omitted). 105

5.1 Times series of the first mode of the MCA, normalised by one standard deviation, where the original MCA time series is in black and the time series extension (computed by projecting the velocity pattern onto the full time series) is in blue. 108

5.2 (a) The annual average north Pacific storm track, in terms of $\overline{v'h'}$ at 850 hPa, for the length of the KEF time series. (b) The annual average eddy heat transport difference, $\overline{v'h'}_{\text{diff}}$, between the phase composites of the KEF. Regions where the statistical significance of the difference is less than 95% and 90% are indicated by light and heavy stippling respectively. 110

5.3 As in Figure 5.2 but for $\overline{v'T'}$. 111

5.4 The full $\overline{v'h'}$ for (a) the boreal winter (DJF); (b) the boreal spring (MAM); (c) the boreal summer (JJA) and (d) the boreal autumn (SON). 113

5.5 The seasonal composite, $\overline{v'h'}_{\text{pos}}$, during the positive phase of the KE index for (a) the boreal winter (DJF); (b) the boreal spring (MAM); (c) the boreal summer (JJA) and (d) the boreal autumn (SON). 114

5.6 As in Figure 5.5 but for $\overline{v'h'}_{\text{neg}}$. 115

5.7 The $\overline{v'h'}_{\text{diff}}$ for (a) the boreal winter (DJF); (b) the boreal spring (MAM); (c) the boreal summer (JJA) and (d) the boreal autumn (SON). Regions where the statistical significance of the difference is less than 95% and 90% are indicated by light and heavy stippling respectively. 116

5.8 Plotted in the lower panel is $\overline{v'h'}_{\text{diff}}$ (where significance is 95% or greater) averaged along the storm track axis (indicated by the grey line in top panel plot, using the $\overline{v'h'}_{\text{pos}}$ from spring as an example) between 140°E and 220°E (the blue outlined region in the top panel) for the boreal spring (in green), boreal winter (in blue) and boreal autumn (in orange). The region is bisected by the thick blue line in the top panel, and averages for the east Pacific region (solid lines) and west Pacific region (dashed lines) are plotted. 117

5.9 Upper panel: Annual average climatology for the mean-sea-level pressure, in hPa, over the period of the KEF index. Lower panel: Annual average climatology for the geopotential height at 500 hPa, in metres, over the period of the KEF index. 119

5.10 Shaded is the annual average SLP anomaly associated with the negative phase of the KEF (i.e. $\overline{P_{\text{neg}}} - \overline{P_0}$). Contoured is the annual average 500 hPa geopotential height anomaly associated with the negative phase of the KEF (i.e. $\overline{Z_{\text{neg}}} - \overline{Z_0}$), from -10 to 26 m with a contour interval of 4 m, where negative values are dashed and positive values are solid. 120

5.11 As in Figure 5.10 but for the anomaly associated with the positive phase of the KEF. Here the geopotential height contours are from -26 to 10 m with a contour interval of 4 m. 121

5.12 The seasonal SLP anomaly (shaded) and 500 hPa geopotential height anomaly associated with the positive phase of the KEF (i.e analogous to Figure 5.11 but for each season) for (a) the boreal winter (DJF); (b) the boreal spring (MAM); (c) the boreal summer (JJA) and (d) the boreal autumn (SON). Negative values are indicated by dashed contours and positive values by negative contours, the contour interval is 4 m (i.e. . . . , -10, -6, -2, +2, +6, +10, . . .). 122

5.13 As in Figure 5.12 but for the negative phase of the KEF. 123

5.14 The annual averages for: (a) The depth integrated geostrophic streamfunction for the full dataset, $\overline{\Psi_0}$; (b) wind-stress curl difference between the positive and negative phases of the Kuroshio Extension front, $\nabla \times \overline{\tau_{\text{diff}}}$; (c) The difference in depth integrated geostrophic streamfunction between the positive and negative phase, $\overline{\Psi_{\text{diff}}}$, calculated from the wind-stress curl difference in (b). The streamfunction was plotted over the continents but it has obviously no meaning there. 125

5.15 A scatter plot of the normalised monthly mean KEF index (i.e. Figure 1b) against the El Niño anomaly for the Nino 3 (in black), Nino 3.4 (in blue) and the Nino 4 (in red) indices, in °C. 127

5.16 Schematic indicating the vorticity tendencies, which act to reinforce the blocking anomaly, in the barotropic eddy-straining mechanism. (From Shutts (1983)). 129

5.17 Schematic of the barotropic eddy enstrophy sources/sinks and the associated barotropic potential vorticity fluxes in the positive and negative phases of the KEF. In the positive phase, the region of baroclinic growth spans the Pacific and the entire region is a net source of barotropic eddy enstrophy (up-gradient flux of barotropic potential vorticity). In the negative phase, there is enhanced baroclinic growth in the western Pacific and barotropic dissipation in the eastern Pacific. This leads to enhanced down-gradient barotropic potential vorticity fluxes which act to enhance blocking patterns. 131

5.18 An illustration of the eddy anisotropy and the horizontal **E** vector. (From Hoskins *et al.* (1983)). 133

5.19 a) The **E** vector divergence calculated at 300 hPa over the full boreal winter and spring (the data has been smoothed using a $10^\circ \times 10^\circ$ spatial average calculated at each point as described in the text). (b) As in (a) for the positive phase of the KEF index. (c) As in (a) for the negative phase of the KEF index. (d) The difference between the positive and negative composites. 135

6.1 Averages of the velocity magnitude and SST gradient magnitude over the period 2002-2011 using the datasets described in Chapter 4. The "along-frontal" axis is marked by the thick black line and the thin grey line marks the area over which the average was taken. 143

6.2 Results of the MCA for the "along-frontal" average time series. The variability of the velocity magnitude (in red) and the SST gradient magnitude (in blue) are scaled to be equal to one standard deviation. The singular values, time series and squared covariance fraction (SCF) are also shown. 144

6.3 "Along-frontal" average for the one standard deviation of the positive phase (in green) and negative phase (in gold) of the first MCA mode(shown in Figure 6.2) 144

6.4 Schematic of the coupled ocean-atmosphere decadal variability. The strong SST front (negative phase) drives an anomalous low in the eastern Pacific (as in Figure 5.10). This anomaly then propagates westwards and 3 years later arrives in the Kuroshio region and acts to weaken the Kuroshio Extension and associated SST front. In the positive phase the opposite is true, suggesting the potential for a coupled oscillation. 146

A.1 Schematic cross-section through the centre of a 2-layer mean subtropical gyre, where the blue line is the interface. On the left, the $\tau = 0$ boundary condition means the volume (and hence mass) of each layer is not conserved. On the right, the interface height is allowed to vary on the boundary and mass is conserved for the same mean flow. 166

B.1 The plots show the evolution of the spin-down simulations of the instability of the $n = 3$ basin mode for $Z = 5$. The baroclinic streamfunction is on the left and the barotropic streamfunction on the right. The instability of the initial baroclinic basin mode generates a field of deformation scale barotropic eddies. All units are non-dimensional. (From LaCasce and Pedlosky (2004)). 173

List of Tables

4.1 Average values of the heat flux divergence and the temperature anomaly over the region of maximum temperature response outlined in Figure 4.6 and the associated damping rate for both phases of the MCA index. 99

5.1 Number of days that are used to produce the seasonal and annual phase composites. 109

Chapter 1

Introduction

Narrow zonal currents are a ubiquitous feature of the midlatitude ocean circulation, with typical meridional scales on the order of a hundred kilometres. The strongest zonal currents in the northern hemisphere are the eastward jets that form when the Gulf Stream and Kuroshio detach from the western boundaries of the North Atlantic and North Pacific respectively, as shown in Figure 1.1. However, the development of satellite altimetry and high resolution ocean models has revealed that weaker zonal jets cover the world's oceans, with both weak and strong jets varying on decadal timescales.

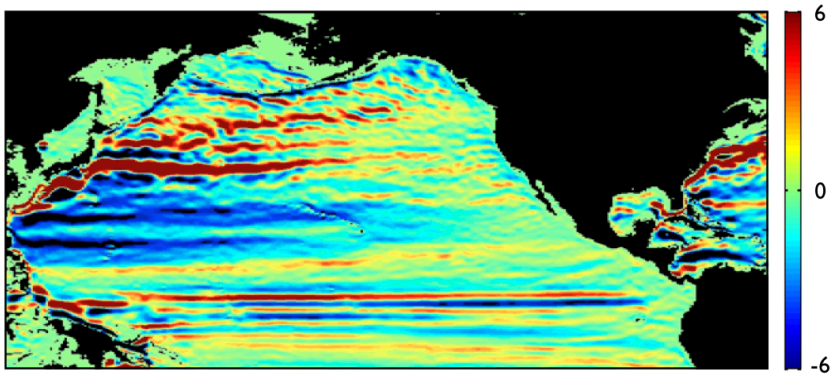


Figure 1.1: Zonal velocity at 400m, in cm/s, averaged over 3 years in an eddy-resolving ocean general circulation model. (From Richards *et al.* (2006)).

An important component in the climate of the midlatitude atmosphere are the synoptic-scale weather systems, or "storms", that move eastwards with the background westerlies and have scales on the order of a thousand kilometres. On short timescales, storms are respon-

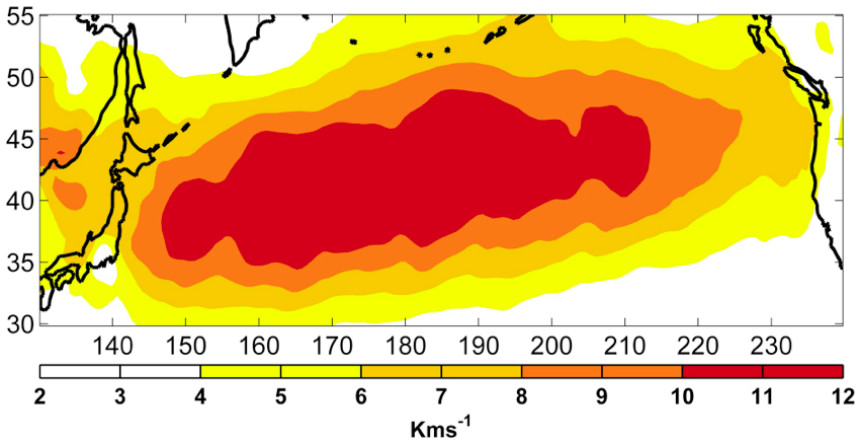


Figure 1.2: Annual average eddy heat transport, $\overline{v'T'}$, at 850 hPa (using high-pass filtered data from the ERA Interim dataset).

sible for strong winds and precipitation, whereas in a time averaged sense they transport heat and moisture polewards thereby exerting a large impact on both global and regional climate. In the northern hemisphere storms predominantly occur over the two midlatitude ocean basins and these regions are referred to as the storm tracks. An example of the North Pacific storm track is shown in Figure 1.2, which is a map of the average poleward heat transport by storms.

In this thesis we investigate two mechanisms by which the zonal ocean jets and storm tracks interact in the northern hemisphere midlatitudes. The first is a the mechanism through which the atmosphere can influence the ocean. The large-scale recirculating gyres in the ocean basins are driven by wind-stress at the surface and the storms are responsible for a relatively high frequency component of this forcing. We study the response of an idealised two-layer ocean model to a simplified storm track stochastic forcing. Rossby waves are generated at the eastern boundary and are found to destabilise as they propagate westwards across the basin, leading to patterns of alternating zonal jets.

The second is a mechanism through which the ocean can influence the atmosphere. In the western regions of the ocean basins, warm water that is carried polewards by the boundary currents loses heat to the relatively cool atmosphere above and thereby influences storm growth. However, western boundary current jets have a distinct decadal variability. In this thesis we use a combination of satellite ocean observations and a reanalysis atmospheric dataset to investigate how the variability of the Kuroshio Extension influences the Pacific

storm track and the large-scale atmospheric circulation.

The thesis is structured as follows. The previous studies under-pinning our investigations are outlined in the background section, Chapter 2. In Chapter 3 we study the response of an idealised two-layer ocean basin model to a stochastic storm track forcing. Chapter 4 considers the variability of oceanic temperature and velocity fields in the vicinity of ocean fronts and an index of the Kuroshio Extension is calculated. In Chapter 5 the response of the storm tracks to the variability of the Kuroshio is analysed. Concluding remarks and a discussion of future work are presented in Chapter 6.

Chapter 2

Background

In this chapter we will discuss the background to our investigations. We begin by discussing the quasigeostrophic equations which underpin our study. This simplified framework has proven a powerful tool with which to investigate complex geophysical phenomena. One such example is baroclinic instability, discussed here in terms of a two-layer system, which greatly influences the general circulation of the atmosphere and oceans. We then review observations of zonal ocean jets in the world's oceans and the generation mechanisms proposed in the literature, as background for the study presented in Chapter 3. Finally, the influence of the oceanic circulation on the midlatitude atmospheric storm tracks is outlined to provide background for the investigations presented in Chapters 4 and 5.

2.1 Quasigeostrophic dynamics

2.1.1 Quasigeostrophic scaling

Vorticity is an important quantity in governing geophysical flows. The vorticity, $\boldsymbol{\omega}$, is a local measure of the amount of rotation and is defined as the curl of the velocity vector $\mathbf{u}$:

$$\boldsymbol{\omega} = \nabla \times \mathbf{u}. \tag{2.1}$$

In the earth's atmosphere and oceans, which are generally stably stratified, flows are predominantly horizontal. For this reason it it the vertical component of the vorticity, as highlighted by Rossby (1939), that is of primary importance for determining the dynamics of large-scale flow in both the atmosphere and oceans. This is inspite of that fact that

the horizontal components of the vorticity are typically larger in magnitude. The vertical component of the vorticity is

$$\boldsymbol{\omega} = \hat{\mathbf{k}}\left(\frac{\partial v}{\partial x} - \frac{\partial u}{\partial y}\right) \equiv \hat{\mathbf{k}}\zeta, \tag{2.2}$$

where ζ is the *relative vorticity* of a horizontal two-dimensional flow. The horizontal shallow water momentum equation (e.g. Vallis, 2006) for a constant density, one-layer ocean with a flat bottom is

$$\frac{D\mathbf{u}}{Dt} + \mathbf{f} \times \mathbf{u} = -g\nabla\eta, \tag{2.3}$$

where η is the deviation of free surface height from the mean height (i.e. $h = H + \eta$), $\mathbf{f} = f\hat{\mathbf{k}}$ is the Coriolis parameter in the Earth's rotating frame and the material derivative, defined as

$$\frac{D}{Dt} = \frac{\partial}{\partial t} + \mathbf{u} \cdot \nabla, \tag{2.4}$$

is the rate of change of a fluid parcel following the flow. For typical scales there is a leading order *geostrophic* balance which exists between the Coriolis term and the height gradient term in the momentum equation, giving the horizontal geostrophic velocity, $\mathbf{u}_g$:

$$\mathbf{u}_g = \frac{g}{f}\hat{\mathbf{k}} \times \nabla\eta. \tag{2.5}$$

Utilising this balance, the horizontal velocity may be written in the form $\mathbf{u} = \mathbf{u}_g + \mathbf{u}_a$, where $\mathbf{u}_a$ is the ageostrophic component. We now make a series of approximations to capture the evolution of the flow that is close to geostrophic balance, which will allow us to simplify the full form of the momentum equation. These are the *quasigeostrophic* (QG) approximations:

- The Rossby number R_o, which is the ratio of the scales of the material derivative and Coriolis terms in the momentum equation, is assumed to be small such that the flow is nearly in geostrophic balance (i.e. $R_o = \frac{U}{fL} \ll 1$).
- Variations in the Coriolis parameter are assumed to be small such that it can be approximated as $f = f_0 + \beta y$, where f_0 is a constant reference value and β is a constant gradient of the Coriolis parameter. The ratio of the scales is $\frac{\beta L}{f_0} \approx O(R_o)$.
- The quasigeostrophic evolution is assumed to occur on the advective time scale and because the geostrophic velocity is much larger than the ageostrophic velocity the

advection in the material derivative is by the geostrophic flow, such that $\frac{D}{Dt} = \frac{\partial}{\partial t} + \mathbf{u}_g \cdot \nabla$.

Using these approximations, retaining terms that are $O(R_o)$ and discarding the higher order terms, the quasigeostrophic momentum equation is

$$\frac{D\mathbf{u}_g}{Dt} + f_0(\hat{\mathbf{k}} \times \mathbf{u}_a) + \beta y(\hat{\mathbf{k}} \times \mathbf{u}_g) = 0. \tag{2.6}$$

Under the QG approximations, along with the assumption that the height perturbation is small compared to the total depth, the shallow water mass conservation equation becomes

$$\frac{1}{H}\frac{Dh}{Dt} = -\nabla \cdot \mathbf{u}_a. \tag{2.7}$$

By taking the curl of the QG momentum equation and using vector identities[1,2], we obtain an equation for the vorticity evolution:

$$\frac{\partial \zeta}{\partial t} + \mathbf{u}_g \cdot \nabla\zeta + f_0(\nabla \cdot \mathbf{u}_a) + \beta v_g = 0, \tag{2.8}$$

where here we have used the fact that the geostrophic velocity is non divergent, $\nabla \cdot \mathbf{u}_g = 0$. Assuming incompressible flow, the ageostrophic divergence can be written as a vortex stretching term, $\nabla \cdot \mathbf{u}_a = \frac{\partial w_a}{\partial z}$. This equation thereby relates the rate of change of vorticity due to the advection of vorticity, planetary vorticity and vortex stretching. Using the mass conservation equation to eliminate the ageostrophic divergence, we obtain a conservation equation for the QG shallow water potential vorticity,

$$\frac{Dq}{Dt} = \frac{D}{Dt}\left(\zeta + \beta y - \frac{f_0}{H}\eta\right) = 0. \tag{2.9}$$

The three terms in the potential vorticity are the relative vorticity, planetary vorticity and vortex stretching term, respectively. We can now define a geostrophic streamfunction,

$$\psi = \frac{g\eta}{f_0}, \tag{2.10}$$

[1] $(\mathbf{u} \cdot \nabla)\mathbf{u} = \frac{1}{2}\nabla(\mathbf{u} \cdot \mathbf{u}) - \mathbf{u} \times (\nabla \times \mathbf{u})$

[2] $\nabla \times (\boldsymbol{\omega} \times \mathbf{u}) = (\mathbf{u} \cdot \nabla)\boldsymbol{\omega} - (\boldsymbol{\omega} \cdot \nabla)\mathbf{u} + \boldsymbol{\omega}(\nabla \cdot \mathbf{u}) - \mathbf{u}(\nabla \cdot \boldsymbol{\omega})$

which gives the horizontal geostrophic velocity components

$$u = -\frac{\partial \psi}{\partial y}, \qquad v = \frac{\partial \psi}{\partial x}. \tag{2.11}$$

The relative vorticity can then be written in terms of the geostrophic streamfunction as

$$\zeta = \nabla^2 \psi. \tag{2.12}$$

We also define the deformation radius,

$$L_d = \frac{\sqrt{gH}}{f_0}. \tag{2.13}$$

The deformation radius is the characteristic length scale at which the geostropic balance becomes important. The conservation equation for the QG shallow water potential vorticity, q, is then

$$\frac{Dq}{Dt} = \frac{D}{Dt}\left(\nabla^2 \psi + \beta y - \frac{1}{L_d^2}\psi\right) = 0. \tag{2.14}$$

2.1.2 Two-layer quasigeostrophic equations

The QG shallow water equation is a simple way to model flow in the absence of stratification, for small Rossby number conditions. The two-layer QG equations are a way of including a simplified stratification, which plays an important role in oceanic and atmospheric dynamics, whilst maintaining the simple framework of the QG approximation. The shallow water QG is extended to a two layer ocean consisting of a layer of constant density fluid, ρ_1, resting on a layer of denser fluid, ρ_2, as depicted in Figure (2.1).

A key difference between the shallow-water QG equation and the two-layer model is that in the latter the surface flow depends on the interfacial displacement, η_1, in addition to the surface displacement, η_0. The surface displacement,

$$\eta_0 = \frac{f_0}{g}\psi_1, \tag{2.15}$$

is scaled by g, whereas the interfacial displacement,

$$\eta_1 = \frac{f_0}{g'}(\psi_2 - \psi_1), \tag{2.16}$$

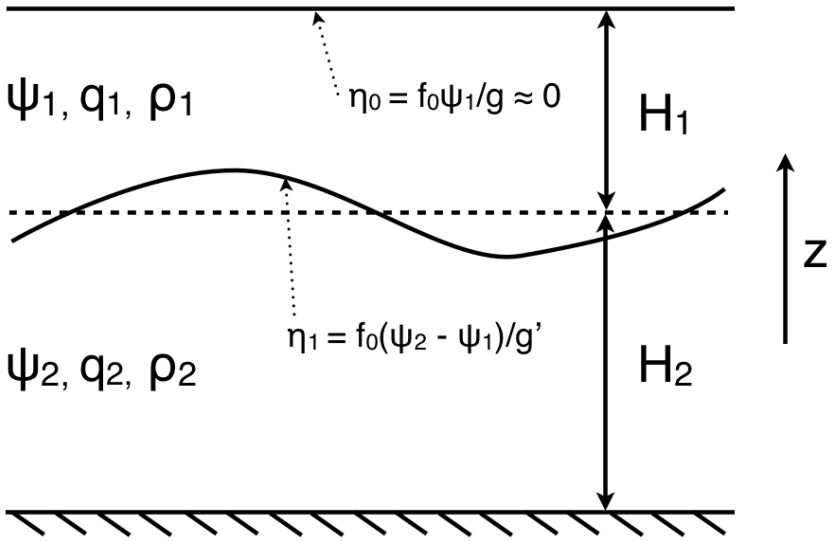


Figure 2.1: Schematic of the two-layer model with flat bottom and rigid-lid approximation.

is scaled by the reduced gravity, g', between the two layers which relates to the density difference across the interface,

$$g' = \frac{\rho_2 - \rho_1}{\rho_2} g. \tag{2.17}$$

As a result, interfacial displacements are several orders of magnitude larger than surface displacements for typical oceanic parameters and are neglected. This is the rigid-lid approximation and excludes surface gravity waves, which is justified in this type of model because the interaction of gravity waves with the slower large-scale ocean circulation is generally weak (e.g. McWilliams, 2006). To simplify the dynamics further, the model is setup with a flat-bottom so we can study the ocean response in the absence of the effects of bottom topography.

With these simplifications the unforced, inviscid two-layer QG model equations are:

$$\frac{\partial q_1}{\partial t} + J(\psi_1, q_1) + \beta \frac{\partial \psi_1}{\partial x} = 0 \tag{2.18}$$

$$\frac{\partial q_2}{\partial t} + J(\psi_2, q_2) + \beta \frac{\partial \psi_2}{\partial x} = 0 \tag{2.19}$$

where q_i is the potential vorticity of layer i,

$$q_i \equiv \nabla^2 \psi_i + h_{3-i} F(\psi_{3-i} - \psi_i), \qquad i = 1, 2 \tag{2.20}$$

and the layer index counts from the surface. Here, h_i is the ratio of the layer thickness at rest, H_i, to the total depth, $H_1 + H_2$. The squared inverse of the deformation radius is $F = \frac{f_0^2(H_1+H_2)}{g'H_1H_2} = \frac{1}{L_d^2}$. The Jacobian represents the advection terms and is defined as $J(a,b) \equiv \left(\frac{\partial a}{\partial x}\frac{\partial b}{\partial y} - \frac{\partial b}{\partial x}\frac{\partial a}{\partial y}\right)$.

All the interesting dynamics in the model stems from the second term in the expression for the PV, (2.20), which couples the upper and lower layers in the layer QG equations, (2.18) and (2.19). This term represents the potential vorticity contribution by stretching/squeezing of fluid column and as such is proportional to the interfacial displacement, η_1. The deformation radius in two-layer QG is related to the reduced gravity between the layers and because of this it is significantly smaller than in the constant density model. This is important because we can expect most of the interesting dynamics, determined by the interfacial displacement, to depend on the deformation radius.

The two-layer QG model can also be written in terms of its vertical normal modes of oscillation. In the two-layer model there is two vertical degrees of freedom and these correspond to the barotropic and first baroclinic modes of the continuously stratified ocean (e.g. Gill, 1982). The barotropic mode describes the vertically averaged flow, which has the streamfunction

$$\phi \equiv h_1\psi_1 + h_2\psi_2. \tag{2.21}$$

The first baroclinic mode, which has the streamfunction

$$\tau \equiv \psi_1 - \psi_2, \tag{2.22}$$

describes the surface flow with respect to the flow at depth and is entirely determined by the displacement of the interface. Conversely, the barotropic streamfunction is independent of the displacement of the interface in this framework.

Using the definitions for the barotropic and baroclinic streamfunctions, the two-layer QG equations, (2.18) and (2.19), can be written in their equivalent modal form:

$$\frac{\partial q_\phi}{\partial t} + J(\phi, q_\phi) + h_1h_2J(\tau, q_\tau) + \beta\frac{\partial \phi}{\partial x} = 0, \tag{2.23}$$

$$\frac{\partial q_\tau}{\partial t} + J(\phi, q_\tau) + J(\tau, q_\phi) + (h_1 - h_2)J(\tau, q_\tau) + \beta\frac{\partial \tau}{\partial x} = 0, \tag{2.24}$$

where the modal potential vorticities are

$$q_\phi \equiv \nabla^2 \phi, \tag{2.25}$$

$$q_\tau \equiv \nabla^2 \tau - F\tau. \tag{2.26}$$

Equation (2.23) describes the evolution of the barotropic vorticity q_ϕ. The first term on the left hand side represents the local tendency of q_ϕ and the second term is advection of the barotropic vorticity by the barotropic flow itself. The third term on the right hand side of (2.23) represents the forcing of the barotropic voritcity by the baroclinic mode, which arises primarily through baroclinic instability which acts to flatten the interface in the model, and thus generates barotropic vorticity. This is often referred to as a "stirring" term. The final term on the left hand side of the barotropic potential vorticity equation is the planetary vorticity advection term. Equation (2.24) is the potential vorticty equation for the baroclinic mode of the two layer model. The first term on the left hand side is the local tendency of the baroclinic potential vorticity and the second term is the advection of baroclinic voriticity by the barotropic flow. The third term on the right hand side represents the tendency of the baroclinic velocity component to generate baroclinic vorticity from the local barotropic vorticity, since the velocity in the lower layer and upper layer are opposite the baroclinic flow, it essentially acts to make a barotropic vortex more baroclinic and thus generates baroclinic vorticity. The fourth term on the left hand side of (2.24) is a self advection term that is zero when the layer heights are equal and is similar to the baroclinic stirring term in (2.24). When the layer heights are equal, the baroclinic self-advection term (associated with baroclinic instability) is most efficient at generating barotropic vorticity and its coefficient in the barotropic vorticity equation (i.e. $h_1 h_2$) is at a maximum and is zero in the baroclinic equation. When the layer heights are not equal however, baroclinic instability is less efficient at generating barotropic vorticity and baroclinic self-advection term also acts to generate baroclinic vorticity. The final term on the left hand side of (2.24) represents the advection of planetary vorticity.

It is this modal form of the two-layer equations that are stepped through in time by the numerical model used in Chapter 3.

2.1.3 Non-dimensional variables

It is often useful to work with non-dimensional variables such that the magnitude of the terms in the PV equations , (2.18) and (2.19), can be estimated in terms of characteristic scales. Taking the characteristic length and velocity scales to be L and U respectively, we introduce non-dimensional variables denoted by asterisks:

$$x = Lx^*, \tag{2.27}$$

$$y = Ly^*, \tag{2.28}$$

$$\psi_i = LU{\psi_i}^*, \tag{2.29}$$

$$t = \frac{L}{U}t^*. \tag{2.30}$$

In terms of non-dimensional variables, the layer PV equations are

$$\frac{\partial {q_i}^*}{\partial t^*} + J({\psi_i}^*, {q_i}^*) + \beta^* \frac{\partial {\psi_i}^*}{\partial x^*} = 0, \qquad i = 1, 2, \tag{2.31}$$

$${q_i}^* \equiv {\nabla_*}^2 {\psi_i}^* + h_{3-i} F^* ({\psi_{3-i}}^* - {\psi_i}^*), \tag{2.32}$$

where ${\nabla_*}^2$ is the non-dimensional Jacobian, the non-dimensional parameter F is

$$F^* = \left(\frac{L}{L_d}\right)^2 \tag{2.33}$$

and β^* is the non-dimensional parameter of the β-effect,

$$\beta^* = \frac{\beta L^2}{U}. \tag{2.34}$$

The modal PV equations can be similarly written in terms of non-dimensional variables. Non-dimensional equations will be used henceforth but the asterisks will be dropped and the use of dimensional variables will be explicitly stated.

2.1.4 Rossby waves in two layers

The restriction on fluid parcels to conserve their potential vorticity provides an effective "restoring force" in the presence of a non-zero planetary vorticity gradient. Consider the linear, inviscid and unforced form of the modal QG model equations, (2.24) and (2.23),

which are respectively:

$$\frac{\partial}{\partial t}(\nabla^2\tau - F\tau) + \beta\frac{\partial \tau}{\partial x} = 0; \tag{2.35}$$

$$\frac{\partial}{\partial t}\nabla^2\phi + \beta\frac{\partial \phi}{\partial x} = 0. \tag{2.36}$$

Assuming the plane wave solutions $\tau = \tau_0 \exp(i[kx+ly-\omega t])$ and $\phi = \phi_0 \exp(i[kx+ly-\omega t])$, where k and l are the zonal and meridional wave numbers respectively and ω is the frequency, yields the dispersion relation for the linear baroclinic Rossby waves

$$\omega_\tau = \frac{-k\beta}{(k^2 + l^2 + F)}, \tag{2.37}$$

and for linear barotropic Rossby waves

$$\omega = \frac{-k\beta}{(k^2 + l^2)}. \tag{2.38}$$

The Rossby waves associated with both the barotropic and baroclinic modes have a westward phase velocity, which represents the sense of the relative vorticity induced by meridionally displacing a fluid parcel from rest. For baroclinic waves that have a wavelength larger than the deformation radius (i.e. $F \gg 1$) we can neglect the wave numbers in the denominator of (2.37) and the phase speed is simply

$$c \approx -\frac{\beta}{F}. \tag{2.39}$$

2.1.5 Two-layer baroclinic instability

Baroclinic instability is an important mechanism by which flow patterns that we observe in both the atmosphere and oceans of the Earth are generated, as first elucidated in the pioneering studies of Eady (1949) an Charney (1947). In a stably stratified ocean, when a flow varies with depth it will have associated with it, a horizontal density gradient. Figure 2.2 is a schematic of two different orientations of constant density layers in an idealised two-layer ocean. On the left, the interfacial surface is tilted and as such there is a horizontal density gradient from which potential energy can be extracted through redistribution of the fluid by the flow. On the right, the interfacial surface is horizontal which constitutes the state of minimum potential energy and no potential energy can be extracted by the flow. In general, density surfaces in the ocean (and atmosphere) are not horizontal and the

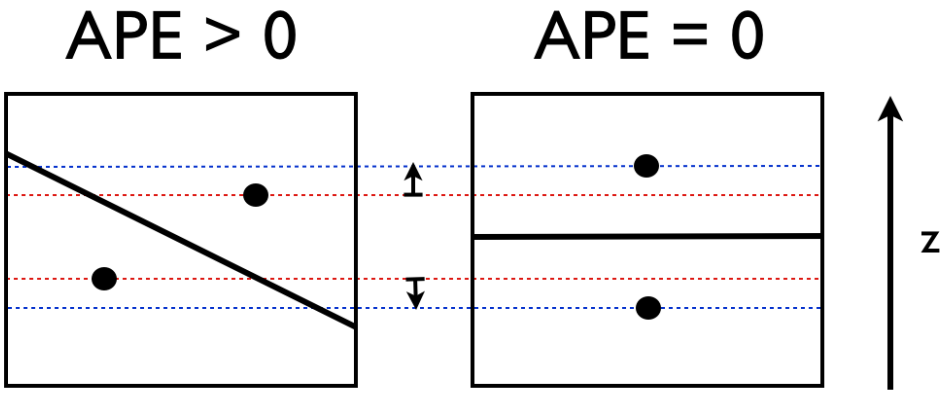


Figure 2.2: Schematic of two orientations of the interface in a two-layer stratified ocean and the available potential energy (APE). The circles mark the centre of mass in each layer in the case of a tilted interface, left, and a flat interface right. The flattening of the interface lowers the centre of mass in the lower layer and raises the centre of mass in the upper layer, corresponding to a release in potential energy due to the density difference between the layers. The flat interface is the minimum potential energy state of the system.

method by which the flow extracts this available potential energy, and the extent to which it does so, determines many of the dynamical phenomena we observe. The amount of excess potential energy that can be extracted by rearranging the density surfaces in Figure 2.2 is referred to as the available potential energy (APE) (Lorenz, 1955).

In the two-layer QG equations, available potential energy is associated with the baroclinic streamfunction which is a proxy for the interfacial height (as shown in Figure 2.1). The extraction of available potential energy from a uniform baroclinic flow in a two-layer QG model was first studied by Phillips (1954) and is an important reference point for the present study. As a result we will now briefly revisit this problem (following Vallis, 2006).

Using the non-dimensional form of the PV equations previously introduced for a two-layer QG ocean with an eastward and uniform baroclinic flow, U_s, the streamfunctions of the basic state, Ψ_i, can be written as

$$\Psi_1 = -Uy, \qquad \Psi_2 = Uy, \tag{2.40}$$

such that the shear velocity is double the velocity scale in each layer, U:

$$U_s = -\frac{\partial \tau}{\partial y} = -\frac{\partial}{\partial y}(\Psi_1 - \Psi_2) = 2U. \tag{2.41}$$

For simplicity we will assume equal layer heights and that the flow is frictionless. To test the stability of the basic flow, the approach is to linearise the potential vorticity equations (2.18) and (2.19) about the basic state and look for growing solutions:

$$\frac{\partial q_j}{\partial t} + J(\Psi_j, q_j) + J(\psi_j, Q_j) + \beta \frac{\partial \psi_j}{\partial x} = 0, \quad j = 1, 2, \tag{2.42}$$

where q_j and ψ_j are the PV and streamfunction of the perturbation in each layer, Q_j is the potential vorticity of the basic state and second order perturbation terms (i.e. $J(\psi_j, q_j)$) have been omitted. With the basic state (2.41) the linearised equations become

$$\left(\frac{\partial}{\partial t} + U\frac{\partial}{\partial x}\right)\left(\nabla^2\psi_1 + \frac{F}{2}(\psi_2 - \psi_1)\right) + \frac{\partial \psi_1}{\partial x}(\beta + FU) = 0, \tag{2.43}$$

$$\left(\frac{\partial}{\partial t} - U\frac{\partial}{\partial x}\right)\left(\nabla^2\psi_2 + \frac{F}{2}(\psi_1 - \psi_2)\right) + \frac{\partial \psi_2}{\partial x}(\beta - FU) = 0. \tag{2.44}$$

Assuming a square domain that is zonally periodic and imposing the boundary condition of no normal flow in the north and south of the domain,

$$\frac{\partial \psi_j}{\partial x} = 0, \qquad y = \pm 1, \tag{2.45}$$

normal mode solutions are sought in the form

$$\psi_j = \text{Re } \tilde{\psi_j} e^{i(kx+ly-\omega t)} = \text{Re } \tilde{\psi_j} e^{ik(x-ct)} e^{ily} \qquad j = 1, 2 \tag{2.46}$$

where $\tilde{\psi_j}$ is the complex amplitude, k and l are the zonal and meridional wave numbers respectively and are positive and real. The angular frequency, ω, and zonal phase speed, $c = \omega/k$, are both complex and can be written explicitly in terms of their real and imaginary parts, e.g.,

$$c = c_r + ic_i. \tag{2.47}$$

The perturbation grows exponentially with growth rate kc_i, when c_i is positive:

$$\psi_j = \text{Re } \tilde{\psi_j} e^{ik(x-c_r t)} e^{kc_i} e^{ily} \qquad j = 1, 2. \tag{2.48}$$

Substituting (2.46) into (2.43) and (2.44) and rearranging gives two homogenous linear

equations in terms of the $\tilde{\psi_1}$ and $\tilde{\psi_2}$:

$$\left[(U-c)\left(\frac{F}{2}+K^2\right)-(\beta+FU)\right]\tilde{\psi_1}-\left[\frac{F}{2}(U-c)\right]\tilde{\psi_2}=0, \tag{2.49}$$

$$-\left[\frac{F}{2}(U+c)\right]\tilde{\psi_1}+\left[(U+c)\left(\frac{F}{2}+K^2\right)+(\beta-FU)\right]\tilde{\psi_2}=0 \tag{2.50}$$

For non-trivial solutions the determinant of the coefficients is zero, yielding a quadratic equation in c which has the solution

$$c=-\frac{\beta}{K^2+F}\left(1+\frac{F}{2K^2}\pm\frac{F}{2K^2}\left[1+\frac{4U^2K^4(K^4-F^2)}{\beta^2F^2}\right]^{1/2}\right), \tag{2.51}$$

where $K^2=(k^2+l^2)$. From this solution we can deduce some interesting characteristics of the two-layer baroclinic instability mechanism. For the the basic state to be unstable and for the perturbation to grow, c_i must be positive, so the radicand in (2.51) must be negative:

$$\frac{\beta^2F^2}{U^2}+4K^4(K^4-F^2)<0. \tag{2.52}$$

The left hand side is a minimum for the intermediate value $K^4=F^2/2$. Using the minimum value for the wavenumber yields a critical velocity shear, U_c, which the basic state must exceed for the instability to grow:

$$U_s>U_c=\frac{2\beta}{F}. \tag{2.53}$$

At this critical shear the most unstable perturbation has wavelength

$$\lambda=2^{\frac{5}{4}}\pi L_d, \tag{2.54}$$

furthermore, the inequality (2.52) yields a minimum scale, $\lambda_{\min}$, that perturbations must exceed to be unstable:

$$\lambda>\lambda_{\min}=2\pi L_d. \tag{2.55}$$

The scale of unstable waves must exceed the deformation radius, which also determines the scale of that most unstable wave.

An interesting characteristic of the instability is the existence of a critical shear, (2.53). The magnitude of the critical shear is determined by two parameters, the planetary vor-

ticity gradient and the squared deformation radius, and increases with both such that in dimensional form the critical velocity shear is

$$U_c \propto \beta L_d. \tag{2.56}$$

Physically, this dependancy can be understood through the following arguments. The basic state flow is purely zonal and as a result, along latitude circles of constant planetary vorticity, βy. For the perturbed fluid columns to be significantly displaced north or south, they must gain or lose relative vorticity, which requires an increase in kinetic energy. The fluid columns can extract kinetic energy from the available potential energy in the basic state flow, however, if the shear is very low, the fluid column cannot extract enough kinetic energy to move it from it's initial latitude and the perturbation cannot grow. As the planetary vorticity gradient increases, the parcel must gain or lose a larger amount of relative vorticity and a larger amount of energy must be extracted, requiring a larger velocity shear. In the corresponding problem with continuous stratification, no critical shear exists but there is an effective critical shear that governs the growth of "deep" modes that span the vertical domain (Vallis, 2006), whereas in the two layer model only deep modes exist.

The scale of the instability is approximately proportional to the deformation radius. Since the relative vorticity is the curl of the horizontal velocity, for larger deformation radii, perturbations must have larger amplitudes for fluid columns to gain sufficient relative vorticity to become unstable. This means that the perturbations for larger deformation radii require larger amounts of kinetic energy to generate the sufficient vorticity perturbation, which ultimately depends on there being sufficient potential energy available. As such, the critical shear of the basic state increases with the deformation radius.

The instability of meridional flow in the two-layer system is particularly pertinent to the study in Chapter 3. Assuming a basic state that is a uniform meridional baroclinic background flow,

$$\Psi_1 = Vx, \qquad \Psi_2 = -Vx, \tag{2.57}$$

where we have used V to represent the velocity scale of the meridional flow[3] . As with the stability analysis of zonal baroclinic flow, we again linearise the layer equations about the

[3]The meridional baroclinic basic state is not a solution of the unforced PV equations but requires a constant forcing term. This does not affect the instability analysis because we only deal with the basic state, as with the unforced basic state in the zonal instability problem.

basic state (2.42) and search for normal mode solutions:

$$\psi_j = \text{Re } \tilde{\psi}_j e^{i(kx+ly-\omega t)} = \text{Re } \tilde{\psi}_i e^{il(y-ct)} e^{ikx} \qquad j = 1, 2, \tag{2.58}$$

adjusted so that $c = \omega/l$, is the meridional phase speed. Substituting this into the linearised PV equations leads to two linear equations as before. The resulting quadratic equation in c has the solution

$$c = \pm V \left(\frac{K^2 - F}{K^2 + F} \right)^{1/2}. \tag{2.59}$$

The radicand must be negative to yield a real growth rate as before, but with the meridional basic state it is clear that the only requirement for the perturbation to be unstable is that it must exceed the same minimum scale as in the zonal instability problem

$$\lambda > \lambda_{\min} = 2\pi L_d. \tag{2.60}$$

Crucially, from (2.59) it is clear that there is no critical velocity shear for the meridional flow. That is, the flow will be unstable even for small values of V, irrespective of the planetary vorticity gradient. When a baroclinic flow is purely meridional, the associated available potential energy is oriented along latitude circles of constant planetary vorticity, βy. As a consequence, displaced fluid columns are not required to generate anomalous relative vorticity, as is the case with zonal flow. The presence of a planetary vorticity gradient therefore preferentially stabilises zonally orientated currents. Of course, in general flows are neither zonally or meridionally orientated and the degree to which the β-effect can stabilise the flow depends on the angle of the flow with respect to the direction of the planetary vorticity gradient and the magnitude of the flow itself (Pedlosky, 1982).

The vertical structure of the instability in the two-layer model can be determined from the phase relationship between the upper and lower layer perturbation. The ratio of the complex amplitudes $\tilde{\psi}_1$ and $\tilde{\psi}_2$, which can be calculated from (2.49), yields a phase relationship between the perturbation streamfunctions:

$$\psi_2 = \left(\frac{\tilde{\psi}_2}{\tilde{\psi}_1} \right) \psi_1 \propto e^{i\theta} \psi_1, \tag{2.61}$$

so that the upper layer wave lags the lower layer wave by the phase,

$$\theta = \tan^{-1}\left[c_i\left(\frac{\beta + FU}{F|U-c|^2}\right)\Big/\left(\frac{F+2K^2}{F} + \frac{(\beta+FU)(U-c_r)}{F|U-c|^2}\right)\right]. \tag{2.62}$$

For growing waves, c_i is positive when the velocity shear is supercritical and consequently the growing upper layer wave lags the wave in the lower layer. For the upper layer wave to lead, c_i must be negative and the perturbation decays. The westward tilt with height is a general feature of growing baroclinic waves and is particularly striking in a continuously stratified system. The upper and lower layer waves in the two layer model closely correspond to the edge waves that occur at the vertical boundaries in the Eady model of baroclinic instability (Eady, 1954).

The energy equation for the perturbations in the two-layer baroclinic instability problem with uniform zonal background flow is found by multiplying the linearised perturbation equations (2.43) and (2.44) by $-\frac{1}{2}\psi_1$ and $-\frac{1}{2}\psi_2$ respectively, summing and integrating over the domain to give:

$$\begin{aligned}\frac{\partial}{\partial t}\iint\limits_{\text{domain}}\left(\frac{1}{2}(\nabla\psi_1)^2 + \frac{1}{2}(\nabla\psi_2)^2 + \frac{F}{4}(\psi_1-\psi_2)^2\right)dx\,dy \\ = -F\iint\limits_{\text{domain}} v_1(\psi_1-\psi_2)U_s\,dx\,dy\end{aligned} \tag{2.63}$$

where the first two terms on the left hand side are the kinetic energies of the perturbation in each layer and the final term on the left hand side is the potential energy of the perturbation. The term on the right hand side represents the extraction of available potential energy from the basic state with velocity shear U_s. This term is the product of the baroclinic perturbation streamfunction, the perturbation velocity and the velocity shear of the basic state. For a westward tilt of the perturbation with height, this term is on average positive over the period of the perturbation wave and the energy of the perturbation grows. This again highlights the importance of the phase relationship between the upper and lower perturbation waves. For an eastward tilt the term in parentheses is on average negative and the energy of the perturbation decreases and the perturbation waves decay. In this way, baroclinic instability facilitates the conversion of available potential energy from the baroclinic basic state into kinetic energy.

An important feature of (2.63) is the single forcing term on the right hand side, from

which it is clear that the available potential energy is only energy source for instability growth for a uniform baroclinic velocity field. In general the background state from which instabilities grow will not be uniform but the degree to which they resemble this uniform flow, with respect to the scale of the deformation radius, will determine the relevance of this idealised understanding of baroclinic instability.

2.2 Zonal jets in the ocean

The advent of satellite altimetry has hugely improved knowledge of sea surface currents over the past two decades. Instantaneous snapshots reveal surface flows dominated by swirling mesoscale (on the order of 100km) eddies (e.g. Chelton *et al.* (2011)). Maximenko *et al.* (2005) discovered that when averaged in time, over periods of up to several years, surface altimeter data, merged from several satellites, revealed multiple zonal jets with alternating east-west surface velocity anomalies across all of the world's oceans. Figure 2.3, from Maximenko *et al.* (2005), shows an 18-week average of observed zonal surface velocity anomaly. The bands of alternating surface current have meridional wavelengths of 200-300km and lengths of up to an order of magnitude larger. Similarly anisotropic features where also reported by Huang *et al.* (2007), who highlighted the importance of time-averaging in the emergence of jets, and by Sokolov and Rintoul (2007) in a study of the Antarctic Circumpolar Current (ACC).

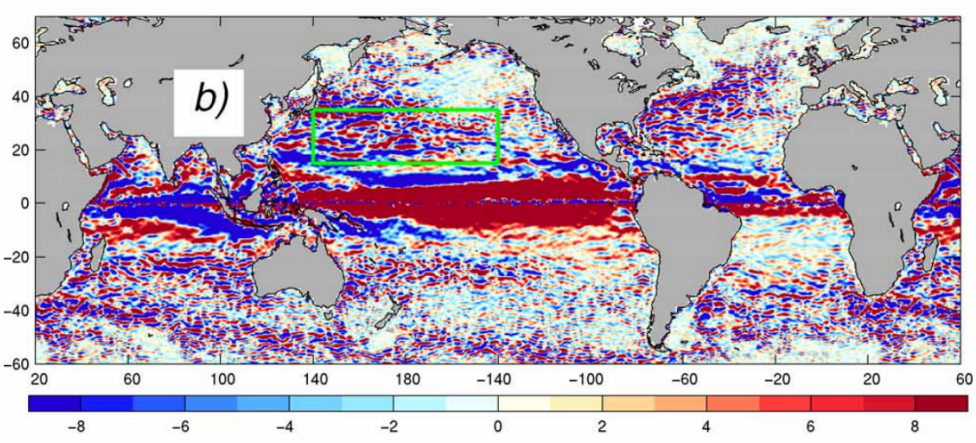


Figure 2.3: 18-week average of the zonal geostrophic velocity anomaly (relative to ten-year average), in cm/s, from the Aviso sea level dataset. (From Maximenko *et al.* (2005)).

Maximenko *et al.* (2008) found similar "jet-like features" when analysing a ten-year

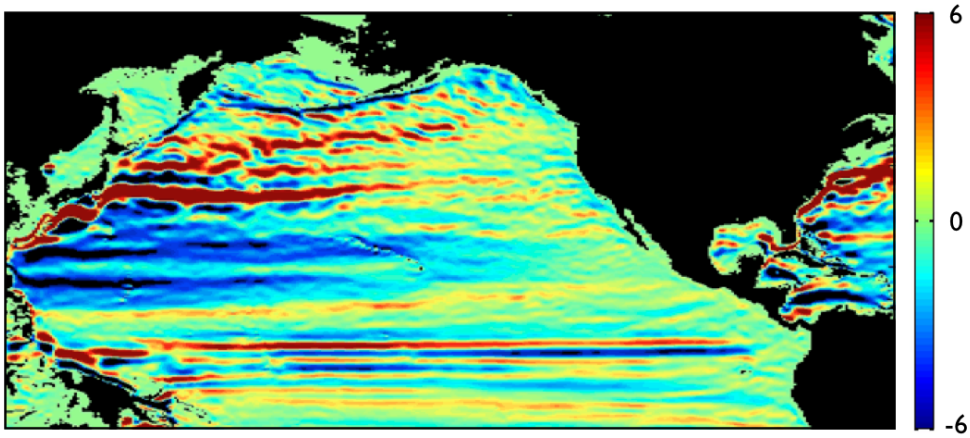


Figure 2.4: Zonal velocity at 400m, in cm/s, averaged over 3 years in an eddy-resolving ocean general circulation model. (From Richards *et al.* (2006)).

mean dynamic ocean topography (MDOT) between 1992-2002, which combined observations by drifters, altimeters and NCEP wind data. Applying a high-pass filter to the MDOT product, the authors focussed on mid-latitude ocean basins and removed the gyre-scale signal to isolate the mesoscale component. Maximenko *et al.* choose to refer to the resultant zonally elongated features in the surface flow as "striations" rather than jets because they observed flow travelling across the striations rather than along them. Expendable bathythermograph (XBT) and float data, from the World Ocean Database 2005 (Boyer *et al.*, 2006), were used to validate the mesoscale striations observed in the MDOT dataset and revealed the striations to be distinct in the depth of 12°C isotherm, close to the depth of the thermocline in the regions investigated. This suggests that the "jets" (as we shall continue to refer to them, for conventional rather than dynamical reasons) may be features of thermocline height that emerge on time-scales of several years. Maximenko *et al.* find a meridional tilt to the zonal surface jets from east to west in the direction of the meridional mean flow associated with the gyre. Analysis of data from Argo floats in the North Atlantic by van Sebille *et al.* (2011) reveals a similar tilt to the jets that emerge in a three-year mean of the velocity profiles.

Alternating zonal surface currents have also been seen to emerge in time-averaged flow in eddy-resolving ocean general circulation models (e.g. Richards *et al.*, 2006; Huang *et al.*, 2007; Kamenkovich *et al.*, 2009). Richards *et al.* (2006) identified jet-like features in the three-year averaged flow, which are vertically coherent throughout the entire depth of the

ocean at midlatitudes and are surface intensified, similar to those observed by Maximenko *et al.* (2008). Interestingly, the emerging jets are not vertically coherent in the tropics, suggesting latitude could be important in determining local vertical jet structure. The three-year mean zonal velocity at 400m below the surface from the model of Richards *et al.* is shown in Figure 2.4.

The observation of alternating zonal jets is reminiscent of the early geostrophic turbulence study by Rhines (1975). Decaying two-dimensional turbulence cascades to larger horizontal scales but Rhines found that in the presence of a meridional planetary vorticity gradient, the cascade is "arrested" in the meridional direction resulting in a field of zonally elongated eddies. Figure 2.6 shows snapshots from the simulations of Rhines (1975) in a doubly-periodic domain, with and without a planetary vorticity gradient, and the anisotropy is evident in the presence of non-zero β. The scale at which the arrest occurs is obtained from a simple scaling of the terms in the barotropic vorticity equation on the β-plane (equivalent to the shallow water QG potential vorticity equation, (2.14), in the limit $L_d \to \infty$):

$$\frac{\partial}{\partial t}\nabla^2\psi + J(\psi, \nabla^2\psi) + \beta\frac{\partial\psi}{\partial x} = 0, \tag{2.64}$$

where the terms scale as

$$\frac{U}{LT} \qquad \frac{U^2}{L^2} \qquad \beta U. \tag{2.65}$$

At small scales non-linear advection will dominate, driving an inverse energy cascade towards larger scales, whereas at large scales the β-term will dominate and the flow will resemble propagating Rossby waves (as in equation (2.38)). The crossover scale, at which the terms are approximately equal in magnitude, is the so-called Rhines scale,

$$L_R = \left(\frac{U}{\beta}\right)^{1/2}. \tag{2.66}$$

Alternate crossover scales between the turbulent and wave regimes were proposed by Vallis and Maltrud (1993), using the phenomenology of two-dimensional turbulence. In a barotropic channel model (i.e. zonally periodic with rigid boundaries to the north and south of the domain) with spatially homogenous forcing at scales smaller that the deformation radius, Vallis and Maltrud found the zonal jet structures which were generated to be extremely persistent. The emergence of anisotropy is also documented in a number of other studies of β-plane barotropic turbulence in a periodic domain (e.g. Vallis and Maltrud,

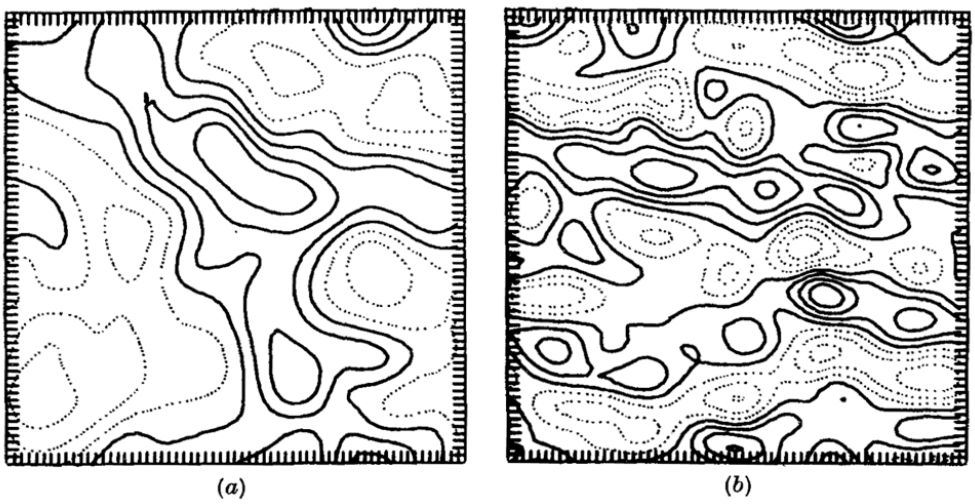


Figure 2.5: Snapshots of decaying barotropic tubulence in the doubly-periodic model of Rhines (1975) with (a) $\beta = 0$ and (b) $\beta > 0$. The eddies that develop in the presence of non-zero β are zonally elongated. (From Rhines (1975)).

1991; Chekhlov *et al.*, 1996; Galperin *et al.*, 2004).

A related model of jet formation is the "potential vorticity staircase" paradigm (Marcus, 1993; Baldwin *et al.*, 2007; Dritschel and McIntyre, 2008). In this model jets exist along "steps" in the meridional potential vorticity field, which act as a barrier to potential vorticity mixing across the jet. The potential vorticity tends to mix either side of the step which further sharpens the gradient across it and this positive feedback tends to maintain the jet. The resulting velocity field consists of narrow eastwards jets, associated with the sharp steps in potential vorticity, interspersed with broader regions of westward flow in which the potential vorticity is partially homogenised. Observations suggest that this mechanism is consistent with the nature of jets on Jupiter (Marcus, 1993).

The emergence of persistent jets in idealised models was extended to include baroclinic effects by Panetta (1993), who found that jets emerge in a zonally reentrant channel from an imposed baroclinically unstable zonal background flow. The jets are primarily barotropic, with the barotropic mode being forced by the baroclinic instability which develops on the imposed background flow. These results are supported by a number of other idealised baroclinic simulations of zonal jets in a channel domain (e.g. Treguier and Panetta, 1994; Thompson and Young, 2007; Berloff *et al.*, 2009a; Berloff *et al.*, 2009b).

The application of these idealised barotropic and baroclinic turbulence studies to the

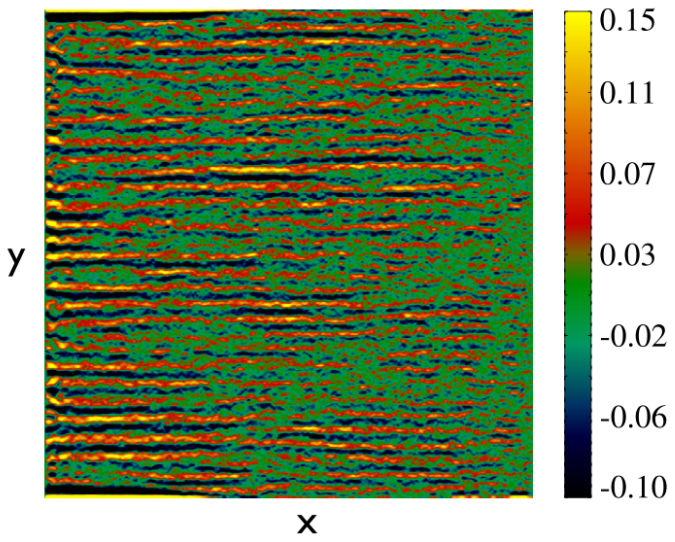


Figure 2.6: Time-averaged non-dimensional streamfunction from the barotropic basin simulations by Nadiga (2006). The simulations were forced with a small scale homogenous stochastic forcing and zero mean forcing. Zonal jets are seen to emerge from an inverse cascade similar to the simulations of Rhines (1975). (From Nadiga (2006)).

jets observed in ocean basins, however, is not straightforward. Firstly, the jets produced in these previous studies are not latent jets, as is evident in the observations, but appear in the instantaneous snapshots of the flow. Berloff *et al.* (2011) investigated the issue of latency in channel models of zonal jets and suggested that the latency of the jets increases with the strength of bottom friction. Secondly, all of the studies discussed employ zonally periodic domains, more suited to model studies of the atmosphere or the Antarctic Circumpolar Current and the presence of meridional boundaries complicates matters, particularly in the presence of large-scale recirculating gyres.

There have been relatively few studies of zonal jet generation in idealised basin simulations. Nadiga (2006) studied the flow of a square barotropic basin subject to small-scale, spatially homogenous, stochastic forcing and found that alternating zonal flows emerged after time averaging, similar to results found with a zonally periodic domain (a similar result is reported by Kramer *et al.* (2006)). An extension of this approach, to include a large-scale mean double-gyre forcing, was carried out by Nadiga and Straub (2010), who demonstrated that zonal jets emerge as small-scale meridional perturbations on the large-scale gyres in the time averaged flow. In a two-layer baroclinic model with a weak small-scale stochastic forcing and zero time mean forcing, Berloff (2005) found that weak alternating zonal flows

emerge in the time mean upper-layer streamfunction. In Chapter 3 we investigate the response of a two-layer QG ocean basin model to *large-scale* atmospheric stochastic forcing and observe emerging zonal jets.

An alternative theory for alternating zonal jets, particularly close to the eastern regions of ocean basins, is that they represent instabilities radiated westwards towards the interior from unstable eastern boundary currents. By carrying out a linear stability analysis, Hristova *et al.* (2008) found that both a baroclinic and barotropic meridional flow along an eastern boundary will radiate baroclinic instability waves that propagate towards a resting interior, with differing energy sources. It is suggested that the structures that emerge have a similar structure to the striations which seem to emerge from the eastern boundary in satellite observations (Centurioni *et al.*, 2008; Maximenko *et al.*, 2008). This was supported by the simulations by Wang *et al.* (2012) using a barotropic QG model forced with an Ekman pumping to drive a mean flow only at the eastern boundary. The resulting sea surface height anomaly when time averaged has the appearance of alternating jets emerging from the boundary and weakening with distance from the eastern boundary. Similar features were observed in laboratory experiments by Afanesyev *et al.* (2012), who simulated an unstable current along an "eastern" boundary in a rotating tank, with the effective planetary vorticity gradient provided by a variation in fluid depth.

The relationship between the alternating jets which emerge with time-averaging and the mesoscale eddies which dominate instantaneous snapshots of surface flow is not clear. A null hypothesis for the emergence of jets with time-averaging is that they simply represent the imprint of westward propagating eddies which are randomly seeded, as suggested by Schlax and Chelton (2008). A related theory, presented by Scott *et al.* (2008), is that mesoscale eddies follow "preferred pathways", potentially influenced by bottom topography, and that striations in the averaged surface flow are observed as a result. Melnichenko *et al.* (2010) analysed the time-averaged vorticity equations and the importance of the individual terms. The Reynolds stresses are not found to support the jets, as in two-dimensional turbulence, but instead act to dissipate or shift them. The vortex stretching term is found to be crucially important in supporting the vorticity of the jets. The striations near the surface are found to cross mean potential vorticity contours which are non-zonal in ocean gyres, compared with purely zonal contours in zonal channel models. Melnichenko *et al.* (2010) argue that because the eddy flux of potential vorticity contribute the time mean budget, eddies interact with the jets and as such they do not simply represent an artefact of westward propagating

eddies.

2.3 The impact of the ocean on the midlatitude storm tracks

In the midlatitudes, tropospheric circulation is dominated by synoptic scale eddies, or weather systems, with scales on the order of 1000km. These atmospheric eddies travel eastwards on the mean westerly flow and are the cause of the large weather variations in midlatitude regions. Typical Eulerian measures of averaged eddy properties (e.g. geopotential height variance, meridional velocity variance and eddy heat transport) reveal peaks over the Pacific and Atlantic oceans in narrow midlatitude bands, as shown in Figure 2.7. These are referred to as the storm tracks because they represent the growth and presence of eddies in the atmosphere.

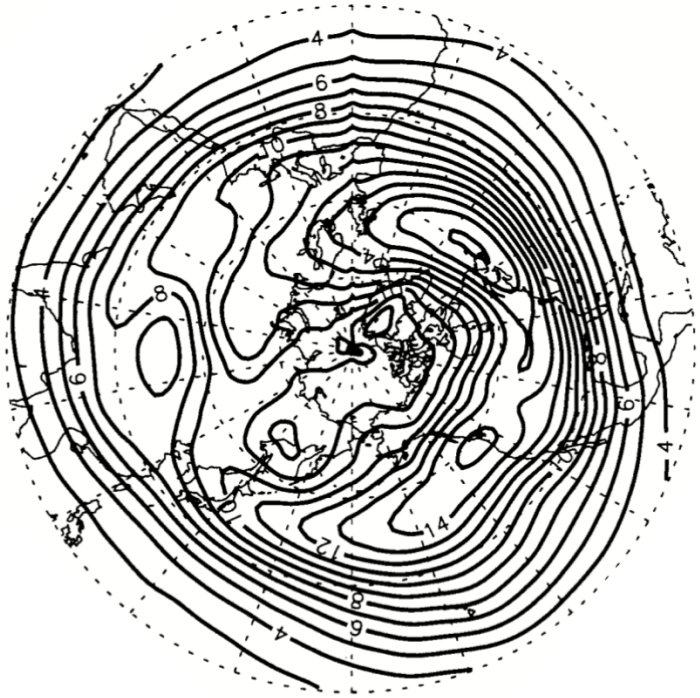


Figure 2.7: Bandpass filtered (2-7 days) standard deviation of the meridional flow at the 300mb pressure level from the NCEP-NCAR reanalysis. The contour interval is 2 ms^{-1}. (From Chang *et al.* (2002)).

The zonally integrated meridional heat transport, shown in Figure 2.8, is an important component in controlling the Earth's climate. Synoptic eddies are the main contributor to

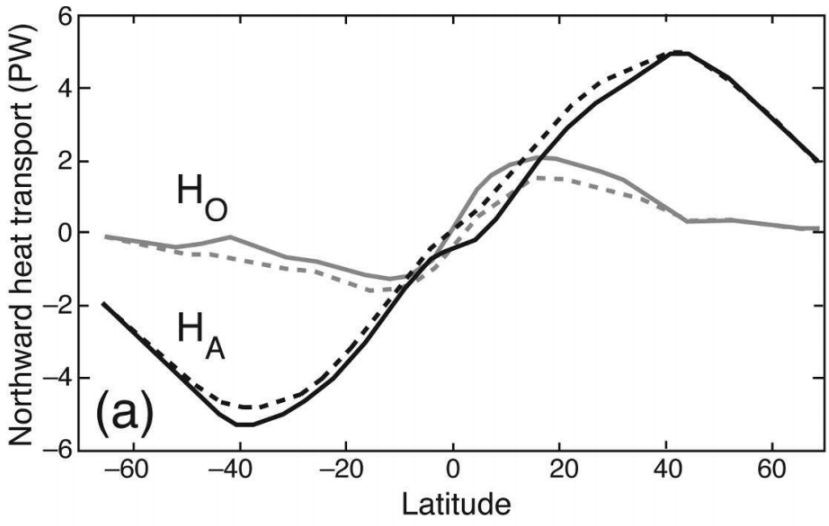


Figure 2.8: Meridional heat transport (northward) as a function of latitude for the ocean (in grey) and atmosphere (in black), calculated from NCEP reanalyses (solid lines) and ECMWF reanalyses (dashed lines). (Reproduced from Czaja and Marshall (2006), who used data from Trenberth and Caron (2001)).

the heat transport in the midlatitudes, whereas the ocean is the dominant conduit at lower latitudes. The zonally integrated decomposition of the global heat transport paints a simple picture of how the ocean and atmosphere may interact in the northern hemisphere. The heat transport by the ocean in the lower latitudes of the northern hemisphere is primarily due to the mean recirculation of the subtropical gyres in the Pacific and Atlantic, which carry warm water from the tropics rapidly along their western boundaries before losing heat to the atmosphere (e.g. Kelly *et al.*, 2010) and the cooler water then slowly returns southwards in the interior of the gyre. The extent of the subtropical gyres is clear in Figure 2.8, where the ocean heat transport is greatly reduced at around 40°N and in this region poleward heat transport by atmospheric eddies is at its largest. With this in mind it is perhaps not surprising that atmospheric heat transport peaks over the ocean basins, before actually even considering the nature of the transient eddies in the atmosphere, or the western boundary currents in the ocean.

Midlatitude eddies form through baroclinic instability, which feeds off the available potential energy arising from meridional temperature gradients in the atmosphere, as outlined for the case of an idealised two-layer fluid in section 2.1.5 of this chapter. The pioneering study by Eady (1949) demonstrated that a basic zonal flow with a vertical shear in velocity,

like that observed in the troposphere, is unstable to baroclinic perturbations with a westward tilt with height[4]. The growth of baroclinic eddies in Eady's model acts to reduce the available potential energy, as in the two-layer model, and thus acts to reduce the meridional temperature gradient by transporting heat polewards. Nonlinear life-cycles of baroclinic instability waves were investigated by Simmons and Hoskins (1978) using a primitive equation model. They found a fairly clear life-cycle consisting of a baroclinic growth phase, during which the low level meridional temperature gradient is reduced and the wave becomes more barotropic, followed by a phase of decay. An important parameter that emerges from the Eady model is the Eady growth rate,

$$\sigma_E = 0.31 \frac{f}{N} \left| \frac{\partial \mathbf{v}}{\partial z} \right|, \tag{2.67}$$

where N is the buoyancy frequency, $\mathbf{v} = (u, v)$ is the horizontal velocity and N is the Brunt-Väisälä frequency, which is a measure of the static stability. The Eady growth rate is a useful measure of the climatological baroclinicity at a particular location, peaking in the two storm track entrances in the northern hemisphere. The distribution of the Eady growth rate, shown in Figure 2.9, helps to explain the zonal asymmetry of the observed northern hemisphere storm tracks. Consistent with the life cycle studies of growing baroclinic waves, the maximum storm track intensity (e.g. Figure 2.7) is downstream of the region of peak baroclinicity. However, the relationship between the Eady growth rate and the storm tracks is not completely straightforward. In particular, the baroclinicity is larger over the Pacific than the Atlantic yet the Pacific storm track is generally weaker, as is clear in Figures 2.7 and 2.9. Since growing baroclinic waves act to reduce the meridional temperature gradient there must be mechanisms in place that restore the zonal asymmetry in baroclinicity that peaks in the storm track entrance regions.

The zonal asymmetry of the mean baroclinicity in the northern hemisphere has been attributed to multiple sources. Firstly, the mean atmospheric flow itself is not zonally symmetric and the departures from a symmetric basic state can be thought of as a series of stationary wave patterns superimposed on the zonal mean flow (e.g. Held *et al.*, 2002). Such stationary wave models indicate that the Himilayan and Rocky mountain ranges generate an anomalous upper-level low downstream (e.g. Trenberth and Chen, 1988; Valdes and

[4]As mentioned previously, Eady's model is broadly equivalent to a the two-layer model with constant stratification, in the absence of a planetary vorticity gradient.

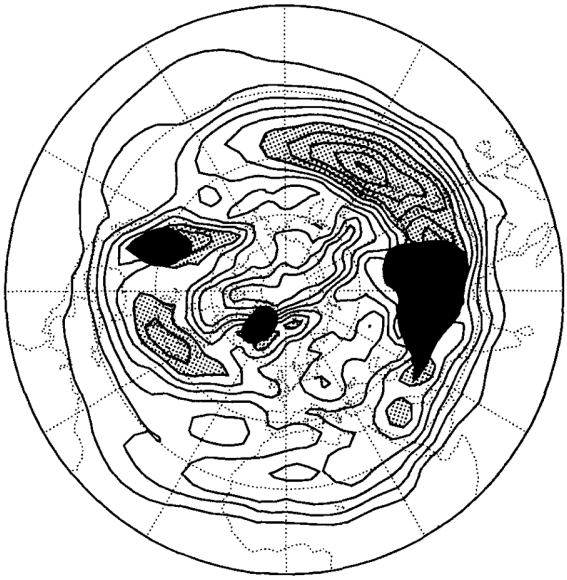


Figure 2.9: Eady growth rate for the Northern hemisphere winter mean at the 780 hPa level. The contour interval is 0.1 day^{-1} and values over 0.6 day^{-1} are stippled. Where the 780 hPa level is likely to be within the boundary layer (due to orography) the data is blacked out. (From Hoskins and Valdes (1990)).

Hoskins, 1989), which enhances the upper level jet in the storm track entrance regions, which can be expected to enhance the mean baroclinicity. Some studies using simple circulation models have achieved enhanced mean baroclinicity in the region downstream of mountain ranges and relatively realistic storm tracks in the absence of moist dynamics (Lee and Mak, 1996; Son *et al.*, 2009).

Using a stationary wave model, with prescribed heating rates and thermal effects of transient eddies calculated from reanalysis data, Hoskins and Valdes (1990) demonstrated that diabatic heating over the storm tracks acts to maintain the maximum in mean baroclinicity, counteracting the tendency of growing baroclinic eddies to reduce meridional temperature gradients. This is related to the evaporation of moisture from the warm western boundary of the ocean and the subsequent latent heat release via precipitation along the storm tracks. A related mechanism which further emphasises the importance of warm western boundary currents in determining the nature of the storm tracks is the "oceanic baroclinic adjustment" hypothesis proposed by Nakamura *et al.* (2004). In this mechanism, midlatitude SST fronts act to effectively generate meridional temperature gradients in the lower troposphere through differential surface heat fluxes across the front, as shown in Figure 2.10.

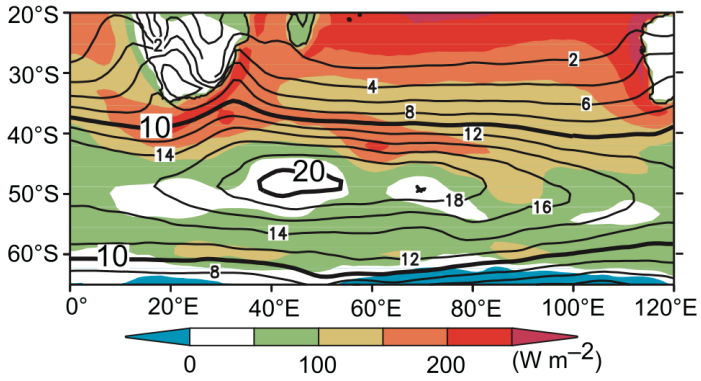


Figure 2.10: Climatology of the (shaded) austral winter turbulent surface heat flux (sensible and latent) and the (contoured) high-pass filtered eddy heat transport ($\overline{v'T'}$) at 850 hPa generated using JRA-25 reanalysis data. (From Nakamura *et al.* (2008)).

The SST gradient is appears to "anchor" the storm track above. The surface temperature gradient is particularly important in potential vorticity models of baroclinic instability in which Rossby waves in the upper troposphere and near to the surface mutually reinforce one another, as outlined by Hoskins *et al.* (1985). The "oceanic baroclinic adjustment" hypothesis is difficult to assess using reanalysis data alone however, because the observation of a peak in mean eddy heat transport downstream from a midlatitude SST gradient (as in Figure 2.10) does not necessarily imply causality.

Subsequently, the importance of SST gradients in determining the nature of the atmosphere has been tested in various numerical modelling studies. Nakamura *et al.* (2008) analysed the results of a pair of aquaplanet GCM simulations with prescribed zonally uniform SST profiles (which were analysed in more detail in Sampe *et al.* (2010)), one with a smoothed meridional SST profile and one with a midlatitude SST front. The experiment with the strong SST gradient is found to anchor a more intense storm track that is situated further poleward than in the control experiment, leading the authors to conclude that in the real atmosphere the "observed collocation is not fortuitous". In a more thorough set of aquaplanet experiments Brayshaw *et al.* (2008) also found that the presence of a midlatitude SST front strongly influences the location of the storm track maximum, again finding that it is anchored on the poleward side of the front. In their simulations with zonally uniform SST profiles, Brayshaw *et al.* showed that the influence of the SST front on the overlying storm track was highly sensitive to its latitude in relation to the subtropical jet, this sensitivity was emphasised by the results of the idealised simulations by Chen *et*

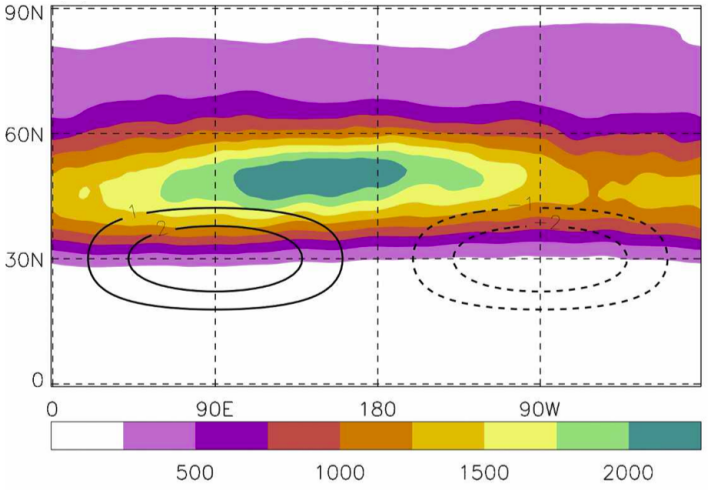


Figure 2.11: Geopotential height variance at 850 hPa in the aquaplanet experiment of Brayshaw *et al.* (2008) with zonally varying SSTs. The SST anomally added to a zonally uniform SST field is contoured (in degrees K) and the maximum SST gradient in this setup is located at 90°E and 40°N. (From Brayshaw *et al.* (2008)).

al. (2010) and Ogawa *et al.* (2012). In the same study, Brayshaw et al. showed that a zonally localised midlatitude SST gradient anchors a zonally asymmetric storm track that peaks slightly poleward and downstream of the strong midlatitude SST front, as is shown in Figure 2.11. These studies suggest that the storm track is more sensitive to alterations in the underlying SST *gradient* rather than the actual SST itself.

The mechanism through which realistic SST fronts can impact the overlying atmosphere has been further examined using more realistic GCMs. Taguchi *et al.* (2009) used a high resolution regional atmospheric model hindcast over the western Pacific region during the cold season of 2003/04, forced by reanalysis data at the boundary, to investigate the air-sea heat fluxes of the mean SST field observed from satellites in comparison to an artificially smoothed SST field. Unsurprisingly, the surface air temperature (SAT) gradient is found to be enhanced across the Kuroshio Extension front and the transient eddy heat transport field exhibits a stronger peak poleward and downstream of the Kuroshio Extension in the simulation with realistic SST fronts when compared to the simulation with smoothed SSTs. Using a coupled GCM with active ocean dynamics, Nonaka *et al.* (2009) highlighted the maintenance of the SAT gradient across the SST front in the southern Indian Ocean and found that this is efficiently restored by the ocean following the passing of a synoptic system with a timescale on the order of a day. In light of the numerical simulations indicating the

important role of SST gradients in maintaining low-level baroclinicity, Hotta and Nakamura (2011) revisited the stationary wave approach of Hoskins and Valdes (1990). Using a more recent reanalysis dataset, Hotta and Nakamura decomposed the diabatic heating into sensible and latent components and found the near-surface differential sensible heating across midlatitude SST fronts was crucially important for maintaining low-level baroclinicity in the storm tracks, apparently more so than latent heating associated with evaporation and precipitation along the storm tracks.

Given the substantial body of literature highlighting the apparent role of midlatitude SST gradients in determining the nature of the storm tracks, the extent to which the time-variability of these SST fronts can influence the atmosphere on interannual to decadal timescales warrants investigation. The Kuroshio Extension in particular is known to exhibit low frequency variability. Qiu and Chen (2005) analysed SSH data in the region of the Kuroshio Extension and found that the current exhibits a dominant low frequency bimodal variability, as had previously been discussed by other authors (e.g. Deser *et al.*, 1999; Schneider *et al.*, 2002). In its "stable" state the current is stronger and predominantly zonal, whereas in the "unstable" state the current is generally weaker and significantly meandering. Figure 2.12 shows a particular SSH contour plotted fortnightly for the 12 years from 1993 to 2004 and the contrast between the particularly stable (i.e. 2002-2004) and unstable (i.e. 1995-1997) years is striking. This variability can be predominantly be attributed to westward propagating long Rossby wave signals in the central and eastern Pacific (e.g. Qiu, 2003; Kwon and Deser, 2007; Taguchi *et al.*, 2007; Sasaki and Schneider, 2011) but similar behaviour has also been generated as intrinsic nonlinear oceanic modes of variability in numerical simulations with mean wind forcing (e.g. Pierini *et al.*, 2009). The variability of the Kuroshio Extension front, the strong SST front located on the northern edge of the Kuroshio Extension has been investigated by Chen (2008). Microwave satellite SST data was used along with a searching algorithm to track the shape and strength of the front, and Chen found that the dominant variability in the strength of the front was fairly well correlated with the strength of the Kuroshio Extension. A small seasonal dependence was seen in the strength of the front, whereas the position of the front exhibits no clear seasonality.

There are few previous studies into the response of the Pacific storm track to fluctuations in the Kuroshio Extension. Joyce *et al.* (2009) investigated the year-to-year variability of near-surface synoptic activity in an air-sea flux dataset in relation to small meridional

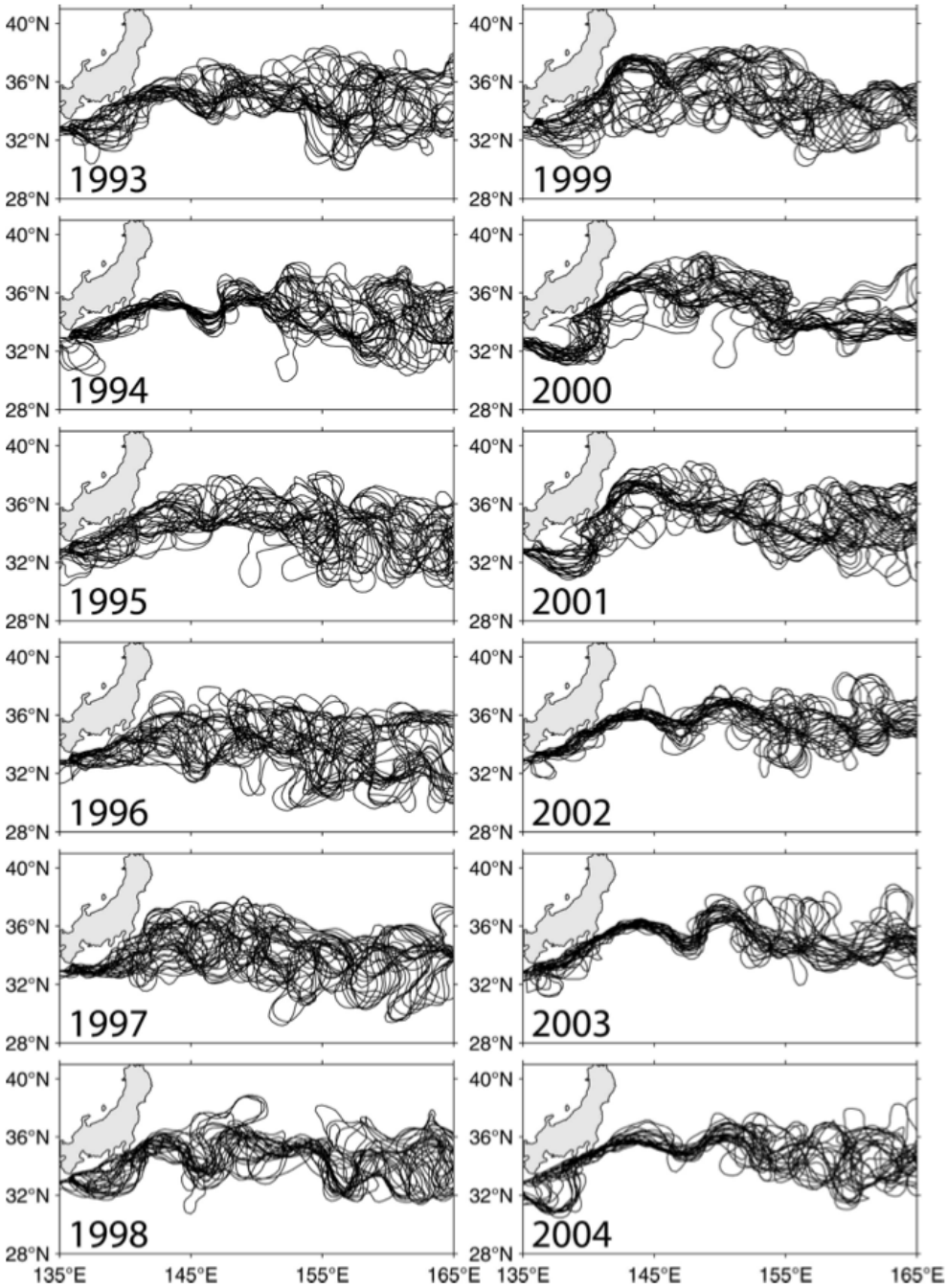


Figure 2.12: Behaviour of the yearly path of Kuroshio Extension, defined by the 170-cm contours in the weekly SSH fields, where the contour is plotted every 14 days. (From Qiu and Chen (2005)).

shifts of the large-scale Kuroshio Extension front, which they defined as the leading principal component of the 14°C isotherm at 200m. The response was seemingly statistically significant but with no coherent mechanism determining the variability. Frankignoul *et al.* (2011) examined the lagged large-scale atmospheric circulation response to a similarly defined index of the Kuroshio Extension. The largest response was a barotropic high (low) over the northwestern Pacific when the Kuroshio Extension axis moved to the north (south) and lead the atmosphere by 2 seasons. In a recent study, Nakamura *et al.* (2012) analysed the impact of the Kuroshio path on Lagrangian winter cyclone tracks over the South of Japan using surface weather charts. They showed that cyclones develop significantly faster and follow a more distinct track when the SST front closely follows, rather than meandering away from, the coastline and is shown to greatly influence the rate of snowfall in Tokyo.

In Chapters 4 and 5 we investigate the response of the Pacific storm track and large-scale atmospheric circulation to the low frequency fluctuations in the Kuroshio Extension using observational and reanalysis datasets.

Chapter 3

Emergence of zonal ocean jets due to atmospheric forcing

In this chapter the oceanic response to large-scale stochastic atmospheric forcing is investigated through the use of a two-layer quasigeostrophic (QG) basin model. The results presented here have been previously reported in O'Reilly *et al.* (2012).

3.1 Quasigeostrophic model setup

3.1.1 Numerical model

The numerical basin model used in this study is the same as that used by LaCasce and Pedlosky (2004), written by Joe LaCasce. The model solves the two-layer non-dimensional modal potential vorticity equations, (2.24) and (2.23), with forcing due to a wind-stress curl forcing in the surface layer, W_{Ek}. The model domain is a square basin with a length of 5000 km and the average depths of the upper and lower layer equal to 700 m and 3300 m respectively, where the interface roughly represents the thermocline in the midlatitude ocean basins. Dissipation is via bottom friction in the lower layer, with a timescale of 280 days (following Arbic and Flierl (2004)) and a weak Rayleigh damping in the upper layer, with a damping timescale of 2800 days. All simulations were integrated for 150 years, starting with a resting ocean, and results were taken after the model had equilibrated after a spin-up time of 35 years. All model runs presented here were performed on a 256×256 grid. The results were verified using higher resolution simulations on a 512×512 grid for the reference stochastic-only forcing experiment and the reference mean and stochastic

forcing experiment, which were both found to exhibit quantitatively similar behaviour to the experiments performed on a 256×256 grid.

One key aspect of the basin model is that the baroclinic stream function is constant at the boundary but this value is allowed to vary in time. The interfacial height therefore varies in time at the boundary, in order to satisfy

$$\frac{\partial}{\partial t} \iint_{\text{basin}} \tau \, dxdy = 0, \tag{3.1}$$

which is the correct "mass conserving" boundary condition (e.g. McWilliams, 1977; Milliff and McWilliams). A description of the numerical model is given in Appendix A.

3.1.2 Large-scale atmospheric forcing

The time variation of wind forcing of ocean basins is known to generate Rossby waves, which emanate from Eastern boundaries (e.g. Gill, 1982; Frankignoul *et al.*, 1997). This is a manifestation of the boundary boundary pressure oscillation driving Rossby waves that have a westward phase velocity. In Northern Hemisphere ocean basins large-scale wind forcing varies on the order of a few days to weeks due to the passage of synoptic-scale weather systems and more persistent atmospheric blocking patterns. In the North Atlantic sector, the dominant large-scale variability caused by the variable propagation of these high and low pressure systems is referred to as the North Atlantic Oscillation (NAO). In the rest of this chapter we investigate the response of the two-layer QG model to a simple model of NAO-like atmospheric stochastic forcing. However, the model is very idealised is also related to the North Pacific.

The NAO is historically described as the difference in seasonal air pressure anomaly between Iceland and the Azores (e.g. Hurrell *et al.*, 2003). The associated large-scale pattern in sea level pressure is a North-South dipole (Walker and Gutzler, 1981) that emerges as the first empirical orthogonal function from monthly anomalies, as shown in Figure (3.1). The NAO thus represents a North-South shift in the westerlies and the associated storm tracks.

The effect of the NAO in the surface wind forcing can be incorporated into the equations of the QG model through the Ekman pumping velocity, W_{Ek}, which is related to the

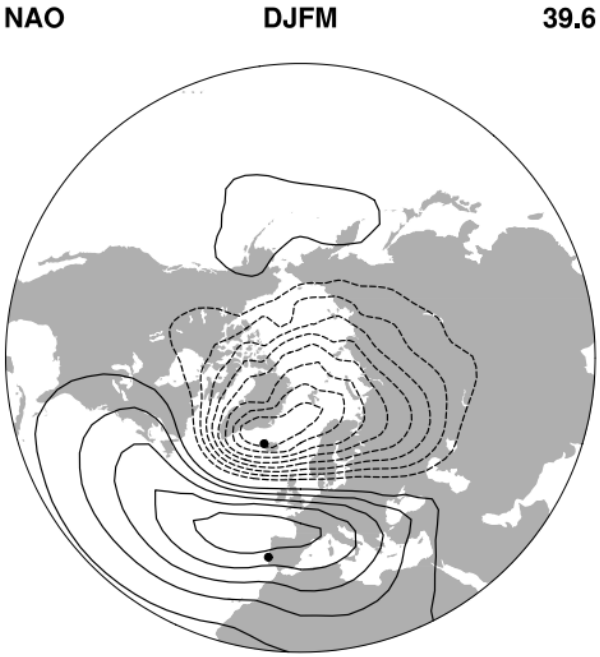


Figure 3.1: Leading empirical orthogonal function (EOF 1) of the winter (December-March) mean sea level pressure anomalies over the North Atlantic sector (20°-70°N, 90°W-40°E), and the percentage of the total variance explained. The contour increment is 0.5 hPa, and the zero contour has been excluded. (From Hurrell *et al.* (2003)).

horizontal curl of the surface wind stress, $\boldsymbol{\tau}$:

$$W_{Ek} = \frac{1}{\rho_{\text{ref}}} \nabla_z \times \left(\frac{\boldsymbol{\tau}}{f} \right), \tag{3.2}$$

where ρ_{ref} is a reference value of seawater density. The zonal surface wind stress anomaly due to the NAO is a meridionally orientated dipole, reflecting the northward (southward) shift in the westerlies in the positive (negative) phase of the NAO. This is demonstrated in Figure (3.2), from Visbeck *et al.* (2003), which shows a large correlation between the NAO index and zonal surface wind stress from the NCEP/NCAR reanalysis dataset (Kalnay *et al.*, 1996). The observed wind-stress anomaly associated with the NAO was used by Marshall *et al.* (2001) to model the response of ocean gyres on long timescales and investigate potential feedbacks. Figure (3.3) shows the "Z" shaped model used by Marshall *et al.*, where the diagonal of the "Z" is the climatological line of zero wind stress curl and the horizontal lines are the lines of zero wind stress curl associated with the NAO anomaly. In this model

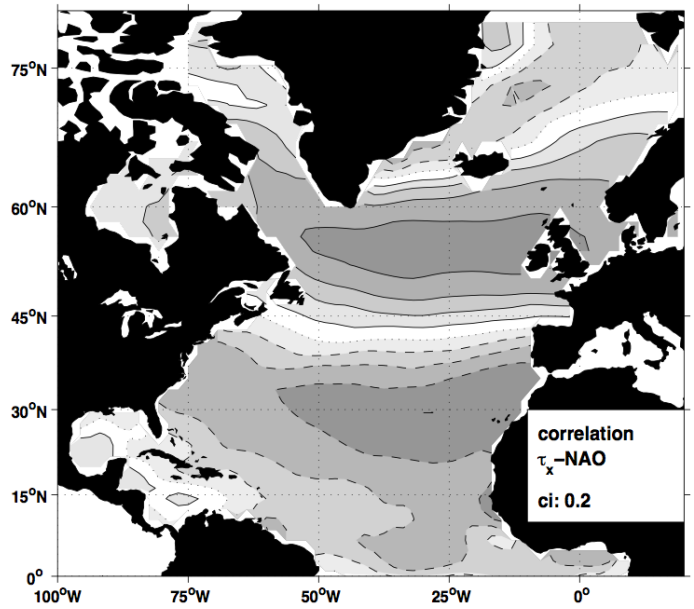


Figure 3.2: Correlation coefficient between yearly NAO-index and zonal wind stress, τ_x. Contours are solid/dashed for positive/negative values and the contour interval is 0.2 with maximum values of 0.8. (From Visbeck *et al.* (2003)).

the meridional shifting of the wind stress pattern causes the subtropical and subpolar gyres to expand and contract, generating an "intergyre gyre" between the climatological mean gyres with its sense of rotation determined by the mean flow.

The form of Ekman pumping used to force the two-layer QG model follows the meridional shifting used by Marshall *et al.* to represent the NAO wind stress curl. The NAO Ekman pumping pattern is modelled as a single-gyre stochastic component superposed on a double-gyre mean wind forcing:

$$W_{Ek} = W_m \sin\left(\frac{2\pi y}{L_y}\right) + W_s(t) \sin\left(\frac{\pi y}{L_y}\right), \tag{3.3}$$

where y is the meridional coordinate in the square basin and L_y is the basin length in the meridional direction. The amplitudes of the mean and stochastic components of the Ekman pumping are W_m and $W_s(t)$ respectively.

This form of Ekman pumping pattern varies only in the meridional direction and as a result the line of zero Ekman pumping is zonally orientated rather than diagonally as in the climatology of the North Atlantic. This allows the simplest analysis in the square basin and

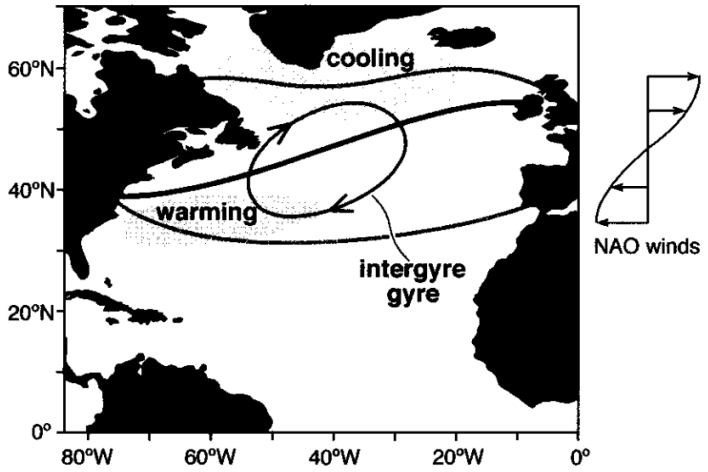


Figure 3.3: Schematic diagram of the "Z" model of Marshall *et al.* where the diagonal is the zero wind curl line of the climatology and the top and bottom lines are the zero wind curl lines of the NAO anomaly. The sense of the "intergyre gyre" spun up by positive NAO forcing is shown. (From Marshall *et al.* (2001)).

symmetric double-gyre mean forcing has been well studied in the literature (e.g. Holland, 1978; Marshall, 1984). The amplitude of the mean double-gyre forcing, W_m, is taken to be equal to a maximum mean Ekman pumping of 50 m yr^{-1} (Levitus, 1994).

The stochastic time series, $W_s(t)$, is computed from a first order Markov process with zero mean. This is based on the hypothesis that the NAO index exhibits a white frequency spectrum on inter-annual timescales (e.g. Wunsch, 1999) but that the atmospheric forcing is persistent on short timescales (Feldstein, 2000). The full form of $W_s(t)$ is calculated from the stochastic process

$$W_s(t) = \sigma_{\text{ref}} M(t), \tag{3.4}$$

where σ_{ref} is the standard deviation of the stochastic component and $M(t)$ is a first order Markov process with zero mean and unit standard deviation, given by

$$M_t = \phi M_{t-1} + a_t, \tag{3.5}$$

with a_t a white noise process and where the coefficient ϕ determines the persistence of the forcing. To calculate suitable values for the stochastic forcing time series we used the NCEP-NCAR reanalysis daily surface wind stress dataset (Kalnay *et al.*, 1996). Taking the mean zonal wind stress at each day over regions associated with the NAO anomaly,

(50°-25°W, 50°-55°N) to the north and (25°-50°W, 25°-30°N) to the south, we computed a time series for the large scale Ekman transport between 27.5°N and 52.5°N:

$$W_{\mathrm{NAO}}(t) = \frac{1}{\rho_{\mathrm{ref}}\Delta y}\left(\frac{\tau_N(t)}{f_N} - \frac{\tau_S(t)}{f_S}\right). \tag{3.6}$$

The annual cycle, empirically constructed from the mean value for each day in the year, was then removed. The standard deviation of the resultant time series were used to define the amplitude of the stochastic component, σ_{ref}. The decorrelation time of the large scale Ekman transport ($\approx$ 7 days) was used to calculate the persistence coefficient, ϕ, for the time series of the stochastic forcing component.

3.2 Stochastic wind forcing simulations

3.2.1 Fofonoff gyres and sponge layers

Prior to investigating the oceanic response to the large-scale atmospheric wind forcing pattern in equation (3.3) we first study the response of the basin model to only the stochastic component of the wind forcing. In doing so we aim to isolate the response to the stochastic component from the basin-scale mean Ekman pumping before analysing the full simulations later in the chapter.

Omitting the double-gyre forcing component, the model Ekman pumping is simply

$$W_{Ek} = W_s(t)\sin\left(\frac{\pi y}{L_y}\right), \tag{3.7}$$

which has a time-mean of zero at every location in the basin. The time mean response to such a forcing, however, is not zero everywhere. Figure (3.4b) shows a snapshot of the upper-layer streamfunction after about 50 years of the model integration and the time mean circulation in the upper layer of this simulation is shown in Figure (3.4a). The flow consists of a westward velocity towards the centre of the basin with eastward recirculation through thin boundary layers along the north and south walls which dominates the instantaneous snapshots as well the mean flow. The mean circulation resembles the analytical solution by Fofonoff (1954) of the unforced, inviscid barotropic vorticity equation on the β-plane. The Fofonoff solution consists of a linear relationship between the mean potential vorticity and the streamfunction which results in two gyres, anticyclonic in the north and cyclonic in the south.

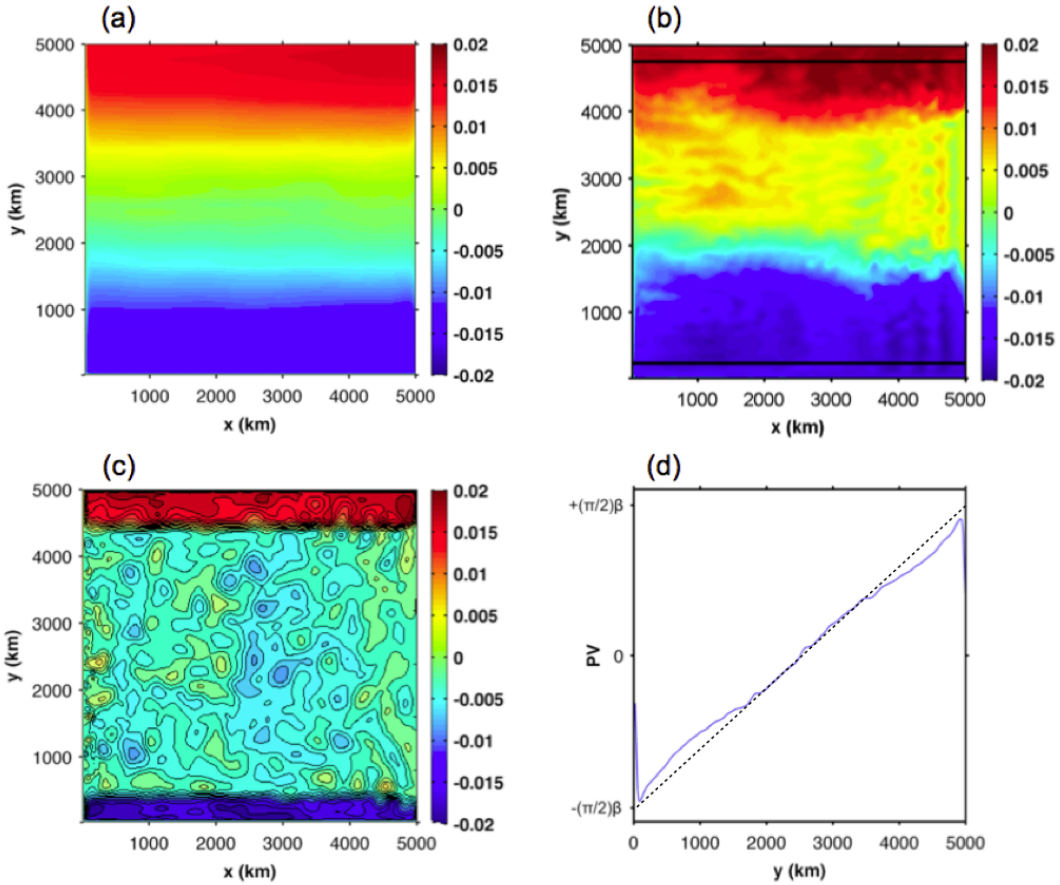


Figure 3.4: (a) Time-averaged non-dimensional upper-layer streamfunction for the simulation with stochastic forcing. (b) Snapshot of the non-dimensional upper-layer streamfunction after about 50 years of the simulation. (c) Snapshot of the non-dimensional barotropic streamfunction during the spin-up phase of the simulation (taken at about 10 years). (d) Meridional cross-section of the time-averaged non-dimensional barotropic potential vorticity, $\overline{\nabla^2\phi} + \beta y$, through the centre of the basin (where the dashed line indicates βy)

The emergence of mean flows resembling Fofonoff gyres is an ubiquitous feature of two-dimensional turbulence in basins and has been reported extensively in the literature (e.g. Griffa and Salmon, 1989; Cummins, 1992; Wang and Vallis, 1994). Bretherton and Haidvogel (1976) demonstrated that the Fofonoff solution represents the minimum potential enstrophy state of the system and unforced weakly decaying turbulence will approach this state due to the conservation of potential enstrophy, as described by Griffa and Salmon (1989). More specifically, the circulation we observe in the numerical simulation in Figure (3.4) is qualitatively comparable to the results obtained by Veronis (1970) using a single layer barotropic basin model. Upon applying a single-gyre forcing with a harmonically oscillating amplitude, Veronis found that inertial gyres, similar to the Fofonoff solution, appear in the time-averaged circulation. In our simulation, baroclinic Rossby waves, driven by the stochastic wind forcing, emanate from the eastern boundary and transit westwards across the basin. As the Rossby waves impact the western boundary they break into small scale vortices, as is evident in the snapshot of the barotropic streamfunction during the model spin-up shown in Figure (3.4c). The small scale vortices at the western boundary are then "sorted out" in a way that fluxes eddy PV down that mean gradient, as in previous studies of two-dimensional turbulence (e.g. Bretherton and Haidvogel, 1976), note that the mean flow is entirely eddy-driven since the mean forcing is zero (i.e. $\overline{W_{Ek}} = 0$). This flux of eddies generates a build up of positive and negative vorticity along the southern and northern boundaries respectively, which acts to effectively erode the planetary vorticity gradient in the north and south of the basin. Figure (3.4d) shows the meridional cross section of the mean total barotropic potential vorticity, $\overline{q_\phi} + \beta y$, and the erosion of the planetary vorticity gradient leads to inertial recirculation along closed contours of constant potential vorticity.

The inertial recirculation gyres that spin-up in the north and south of the basin dominate the dynamics and inhibit our ability to investigate the dynamics of the ocean interior. In order to suppress the development of these gyres we employ dissipative sponge layers along the northern and southern boundaries which relax the potential vorticity towards the local planetary vorticity. Figure (3.5) is a schematic of the sponge layers which span the basin zonally and are 250km wide. They are implemented in the model equation through an extra dissipative term, $-\gamma q_i$ (where q_i is as defined in (2.20)), in the potential vorticity equations, (2.18) and (2.19). The timescale of the damping parameter γ was set to 60 days, which was just strong enough to suppress the inertial recirculation gyres while not overly

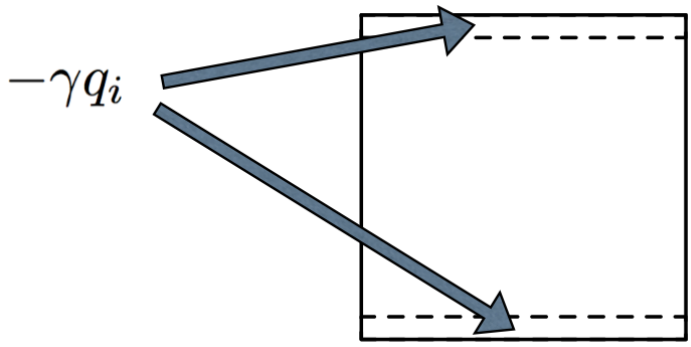


Figure 3.5: Schematic of the dissipative sponge layers employed in the north and south of the basin to prevent the spin-up of inertial recirculation gyres. A dissipation of $-\gamma q_i$ (where q_i is as defined in (2.20)) is applied that relaxes the PV towards βy.

influencing the dynamics in the interior of the basin. As expected, with the sponge layers there is no significant mean flow generated by the stochastic-only forcing. The remaining simulations using stochastic-only forcing are all run with the dissipative sponge layers, it should be noted that the sponge layers effectively shorten the meridional scale of the basin to 4500km.

3.2.2 Rossby basin modes

After the initial application of the stochastic forcing to the basin, baroclinic and barotropic Rossby waves are seen emanating from the eastern boundary which are generated by the fluctuating streamfunction along the boundary of the model (i.e. through the boundary condition as shown in Figure A.1 in Appendix A). As mentioned previously, the timescales of barotropic and baroclinic Rossby waves differ hugely. Crucially, this means that all long baroclinic Rossby waves have equal phase speed at all latitudes in our two-layer QG model, as a result of the β-plane approximation (this is not the case for the real ocean since β and F clearly depend on latitude). For the parameters used in our basin simulations this corresponds to a transit time of about 8 years for long baroclinic Rossby waves, whereas it takes barotropic Rossby waves on the order of a few days to cross the basin.

Lacasce (2000) and Cessi and Primeau (2001) have discussed the theoretical existence of so-called "Rossby basin modes", which are a particular class of low frequency baroclinic Rossby waves that are particularly resistant to dissipation. Cessi and Louazel (2001) demonstrated the emergence of the basin modes as the dominant signal in a linear reduced-gravity

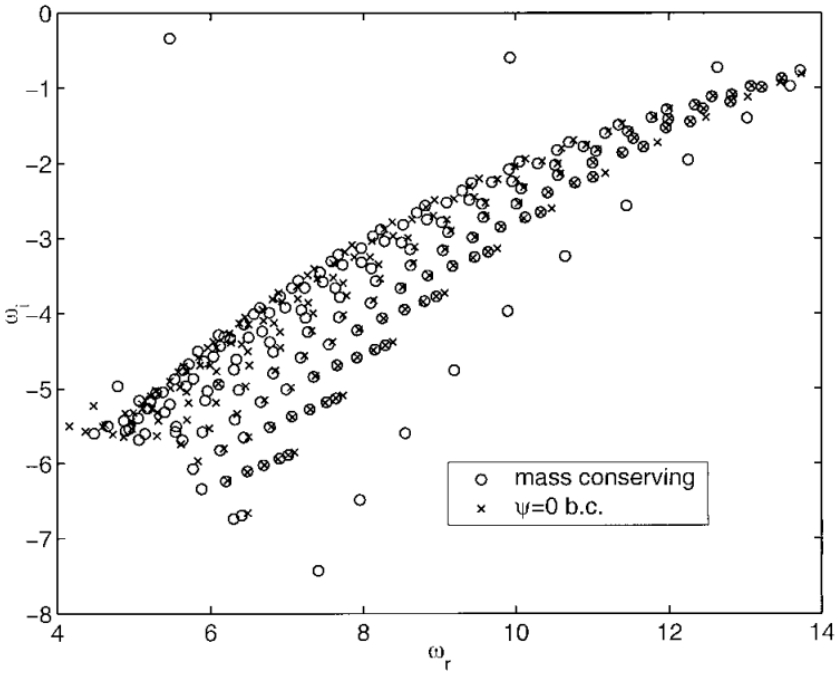


Figure 3.6: Scatter plot of eigenvalues of the frequency from the linear reduced gravity study by Cessi and Primeau (2001) for both the "mass conserving" boundary condition and the $\psi = 0$ boundary condition in the presence of weak dissipation. The imaginary part of the frequency, ω_i, is the damping rate and the real part, ω_r, is the frequency of the Rossby wave oscillation. Allowing the streamfunction to vary on the boundary allows basin modes to be very weakly damped in comparison to other frequencies. (From Cessi and Primeau (2001)).

model, including full variation of the Coriolis parameter, forced with large-scale stochastic forcing similar to (3.7). Rossby basin modes arise through basin-wide resonances of long Rossby waves whose zonal wavelengths span the basin an integral number of times,

$$\lambda_n = \frac{L_x}{n}, \tag{3.8}$$

where λ_n are the zonal wavelengths of the basin modes and n is a positive integer. The condition that the baroclinic stream function is constant along the boundary and that it can change in time means that as a propagating Rossby wave impacts the western boundary a corresponding Rossby wave is excited at the eastern boundary. This acts to reinforce the waves with basin mode wavelengths and means that they are most resistant to dissipation. The "mass conserving" boundary condition, (3.1), on the baroclinic mode is thus absolutely key to the existence Rossby basin modes. Figure 3.6 shows frequency eigenvalues from the

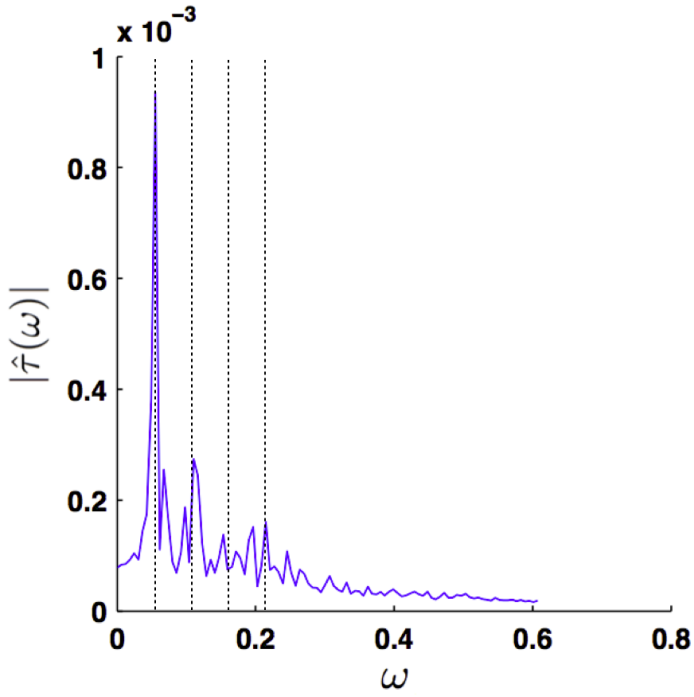


Figure 3.7: Frequency spectrum of the baroclinic streamfunction $|\hat{\tau}(\omega)|$ as measured at the centre of the basin. The basin mode frequencies the frequencies are $\omega_n \approx 0.055n$ (the frequencies of the first four modes are marked by the dashed lines). The streamfunction and frequency are both in non-dimensional model units.

linear reduced gravity study by Cessi and Primeau (2001). In the presence of dissipation, the mass conserving boundary condition is seen to allow basin modes to be very weakly damped. Without dissipation there is no significant difference between the two boundary conditions (Flierl, 1977). Physically, the mass conserving boundary condition amounts to a parameterisation of the effect of ageostrophic boundary kelvin waves, which are infinitely fast under the quasigeostrophic approximation.

Given the emergence of basin modes in related studies, it is reasonable to expect baroclinic Rossby basin modes to be excited in our stochastic-only forcing simulation. The constant phase velocity of westward propagating long Rossby waves means that the frequencies of the basin modes, ω_n, occur at equally spaced intervals according to

$$\omega_n = \frac{2\pi\beta}{FL_x}n, \tag{3.9}$$

where again, n is a positive integer. Figure (3.7) shows the frequency spectrum of the non-

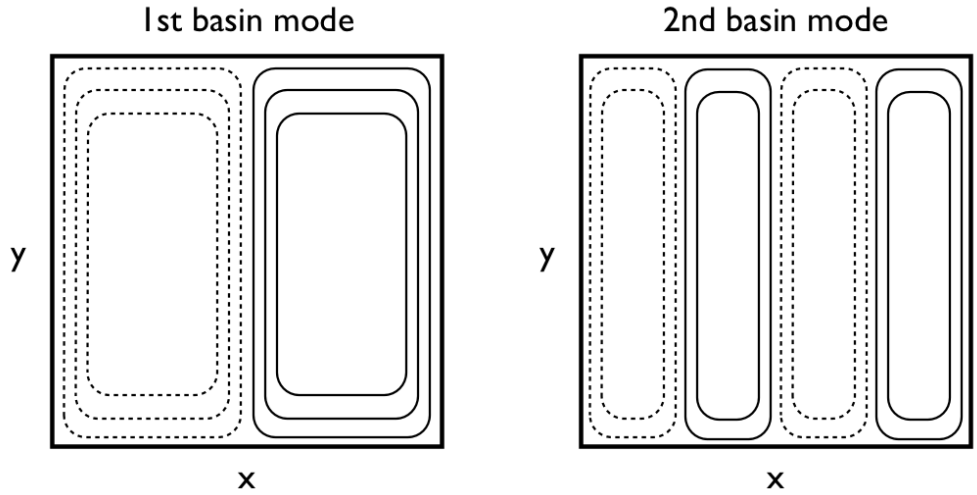


Figure 3.8: Schematic of structure of first and second basin modes in the baroclinic streamfunction. Dashed contours are negative and solid contours are positive. The structure of the basin modes leads to associated flow which is predominantly meridional, whilst the waves also have a large extent in the zonal direction.

dimensional baroclinic streamfunction taken from the centre of the basin, after an initial spin-up period equal to $3\frac{1}{2}$ baroclinic Rossby wave transit times, over the full simulation. In non-dimensional units the frequencies correspond to $\omega_n \approx 0.055n$. The spectrum is dominated by the first basin mode with a smaller but discernible peak at the frequency of the second basin mode, these two primary modes are sketched in Figure 3.8. The higher frequency modes are very weak as are the majority of the non-modal frequencies, suggesting that the response of the basin to the large-scale stochastic forcing is on the whole dominated by Rossby basin modes with very large zonal wavelengths.

3.2.3 Rossby wave instability

The Rossby waves that are generated by the stochastic forcing emanate from the eastern boundary, span the basin in the meridional direction and generally have a large zonal wavelength, as a result of the zonally constant forcing pattern (i.e. $\partial W_{Ek}/\partial x = 0$). Figure 3.9 shows a snapshot of the baroclinic streamfunction and captures the evolution of the baroclinic Rossby waves as they traverse the basin. At the eastern boundary the emerging Rossby wave front has the same meridional orientation as the boundary itself and the associated baroclinic velocity is purely north-south, whereas the meridional wavefront has

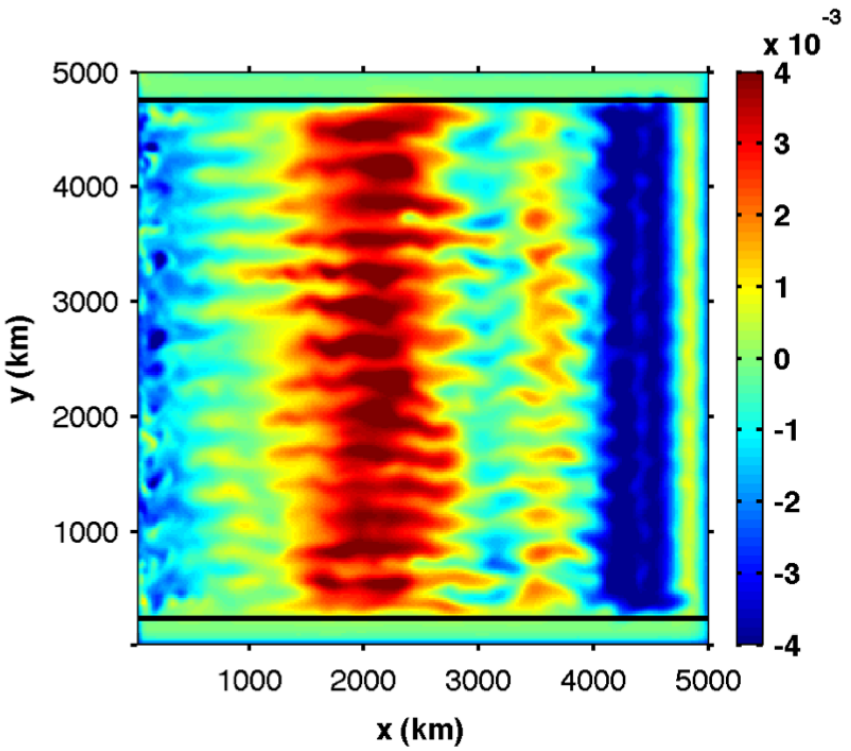


Figure 3.9: Snapshot of the non-dimensional baroclinic streamfunction in the reference stochastic-only forcing experiment. The Rossby waves emanating from the eastern boundary are see to develop instability where there is significant velocity shear. The black lines in the north and south of the basin indicates the positions of the dissipative sponge layers.

been significantly deformed by the time it reaches the centre of the basin where long zonal "tongues" emerge. From section 2.1.5, we expect baroclinic currents to be unstable but how does this translate to Rossby waves?

The Rossby wave instability problem has been the subject of a number of studies, which are discussed in more detail in Appendix B. A result that is particularly relevant is from the study of baroclinic Rossby basin mode instability by Lacasce and Pedlosky (2004). They demonstrated that the instability mechanism depends on the non dimensional parameter, $F = L^2/{L_d}^2$, where L is the length scale of the baroclinic Rossby wave. When $F \lesssim 1$, Rossby waves are susceptible to barotropic-type instabilities whereas when $F \gg 1$, the instability mechanism closely resembles the instability of a uniform baroclinic flow (as described in section 2.1.5).

It is clear from the dominant basin modes that appear in our reference simulation with

stochastic-only forcing, shown in Figure 3.9, that the scale of these waves is in the $F \gg 1$ regime. As a result, we expect baroclinic instability to be the dominant mechanism acting to destabilise the Rossby waves. However, unlike the spin-down experiments of LaCasce and Pedlosky, in which they initiated a basin with an arbitrarily chosen third basin mode, in our forced dissipated simulation the dynamics are dominated by the first basin mode. We expect the Rossby waves to be baroclinically unstable and that, following equation (2.59), the growth rate of the instability, σ, will be proportional to the meridional velocity shear and thus related to the baroclinic streamfunction:

$$\sigma \propto \left| \frac{\partial \tau}{\partial x} \right|. \tag{3.10}$$

As the waves emerge from the eastern boundary and move westwards across the basin, baroclinic instability grows initially on the Rossby waves where the vertical velocity shear is largest. The perturbation continues to grow as the wave moves westwards, generating long zonal "tongues" in the baroclinic streamfunction as seen in Figure 3.9. The zonal tongues extend from the crest to the trough of the basic (meridionally-orientated) Rossby waves, the growth of the initial instability being halted due the absence of available potential energy. In this way the scale of the zonal tongues appears to be largely set by the wavelength of the basic Rossby wave. In spite of the instability growth, the large-scale Rossby waves remain distinct and the whole system of large-scale meridional wave and the zonal tongues transit the basin together, until they reach the western boundary.

To verify that the pertubations do reflect the growth of baroclinic instability waves on the large-scale baroclinic Rossby waves we analyse the zonal transport of anomalous interfacial displacement, diagnosed as $\overline{u'\tau'}$, which corresponds to the zonal eddy "heat transport" in a two layer model. When the large-scale zonal gradient of τ is positive, a negative zonal eddy transport of τ represents the action of growing baroclinic waves to reduce the APE of the large-scale wave. Where the zonal gradient of the large-scale wave is negative the zonal eddy transport of τ is predominantly positive for growing baroclinic waves. This is confirmed by Figure 3.10. The zonal eddy transport, $\overline{u'\tau'}$, is shown in panel (c) for the period between the snapshots shown in panels (a) and (b). In the eastern region of the basin, where the large scale zonal gradient of τ is negative the zonal addy transport is generally positive (shown in panel (d)) and this reflects the growth of the zonal pertubations at the expense of the large-scale APE.

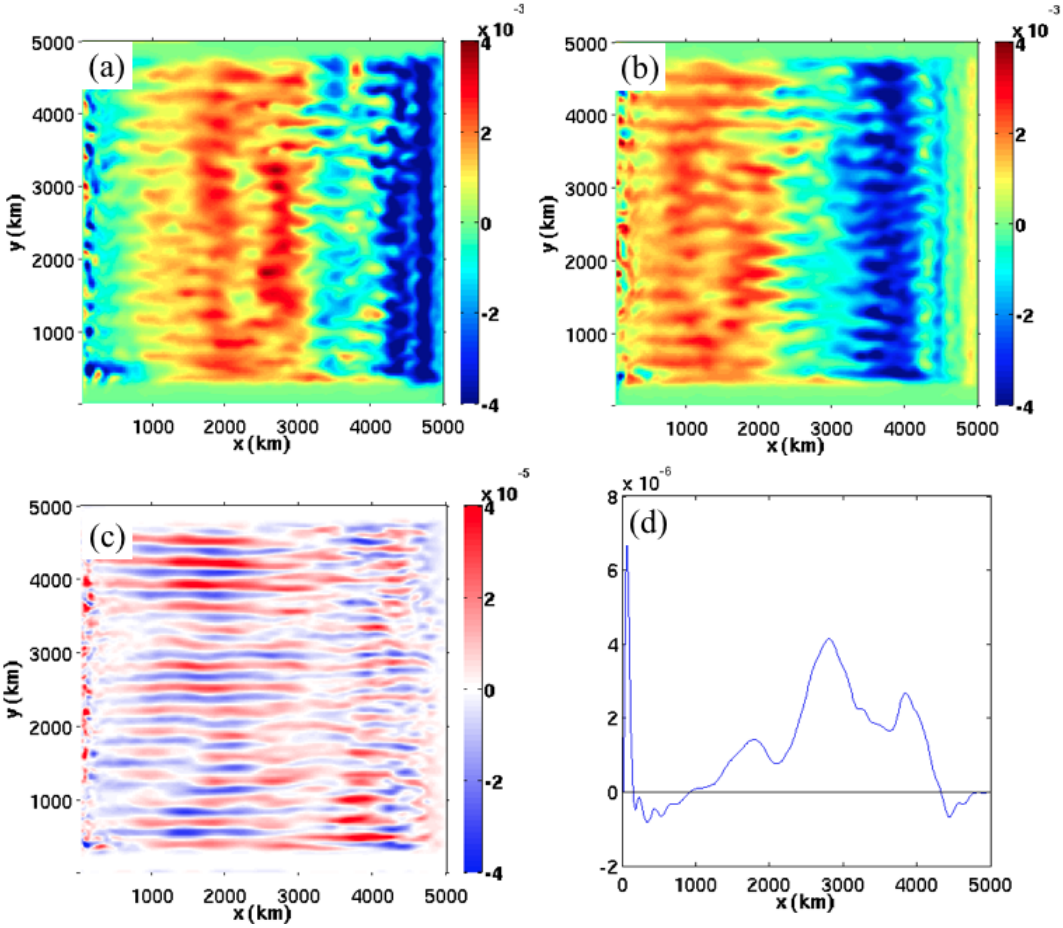


Figure 3.10: (a) Snapshot of the baroclinic stream function at the start of the averaging period. (b) Snapshot of the baroclinic stream function at the end of the averaging period, note the westward progression of the meridionally orientated Rossby waves and the pertubations that have developed. (c) The zonal "heat transport" average, $\overline{u'\tau'}$, in the period between the snapshots in (a) and (b). (d) the meridional integral of the zonal heat transport average shown in (c).

The zonal baroclinic perturbations that develop, as the Rossby waves cross the basin, themselves have a vertical velocity shear that could be baroclinically unstable. As discussed in section 2.1.5, in the presence of the planetary vorticity gradient the instability of zonal flows is suppressed relative to meridional flows of the same amplitude. Therefore if there is unstable growth on the jets, it is unable to occur to a significant degree while the waves cross the basin. The prominence of the primary instability growth on the basic wave and the weak secondary instability on the zonal perturbations are the key features of the reference stochastic-only forcing simulation.

3.2.4 Emergence of alternating zonal jets at surface

In the two layer model the surface motion is related to the barotropic and baroclinic modes by

$$\psi_1 = \phi + h_2\tau, \tag{3.11}$$

(where, as defined in equations (2.21) and (2.22), ϕ and τ are the barotropic and baroclinic streamfunctions respectively) and the distortion of the large-scale Rossby waves by the primary instability can be seen to some extent in snapshots of the surface flow, as in Figure 3.11a which shows a snapshot of the surface zonal velocity field. In particular, when averaging the surface flow over periods of a few weeks or more, the surface streamfunction almost entirely reflects the baroclinic mode as the barotropic waves generated by the stochastic forcing have time scales of a few days to weeks and average to zero. Figures 3.11a, 3.11b, 3.11c and 3.11d show maps of the zonal velocity anomaly, u_1' (cm/s), from a snapshot, a 20-week average, a 200-week average and a 500-week average respectively. For comparison, the transit time of baroclinic Rossby waves in the reference stochastic forcing simulation is approximately 400 weeks. The emergence of alternating zonal velocity jets with increasing averaging period is striking. The jets appear to be stationary features on these long timescales but as indicated by the decreasing amplitude with increasing averaging period, the jets disappear with infinite averaging period. This is due to the jets only emerging through the projection of the baroclinic tongues onto the surface streamfunction and averaging the field in time blurs the zonal dependence, as shown in Figure 3.12, giving the appearance of stationary jets.

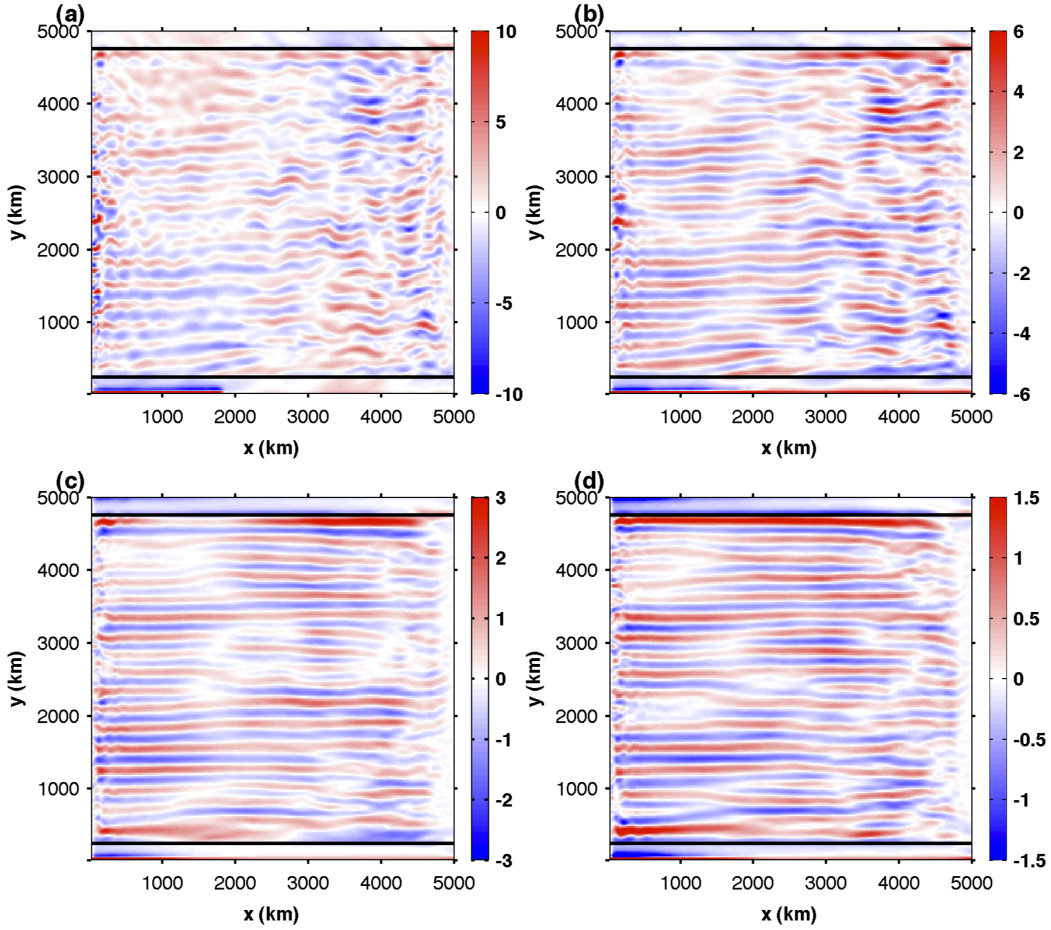


Figure 3.11: Maps of the upper-layer zonal velocity anomaly, u_1' (cm/s), in the stochastic forcing simulations for (a) snapshot, (b) 20-week average, (c) 200-week average and (c) 500-week average for the simulation with stochastic-only forcing. The bold black lines mark the edge of the dissipative sponge layers.

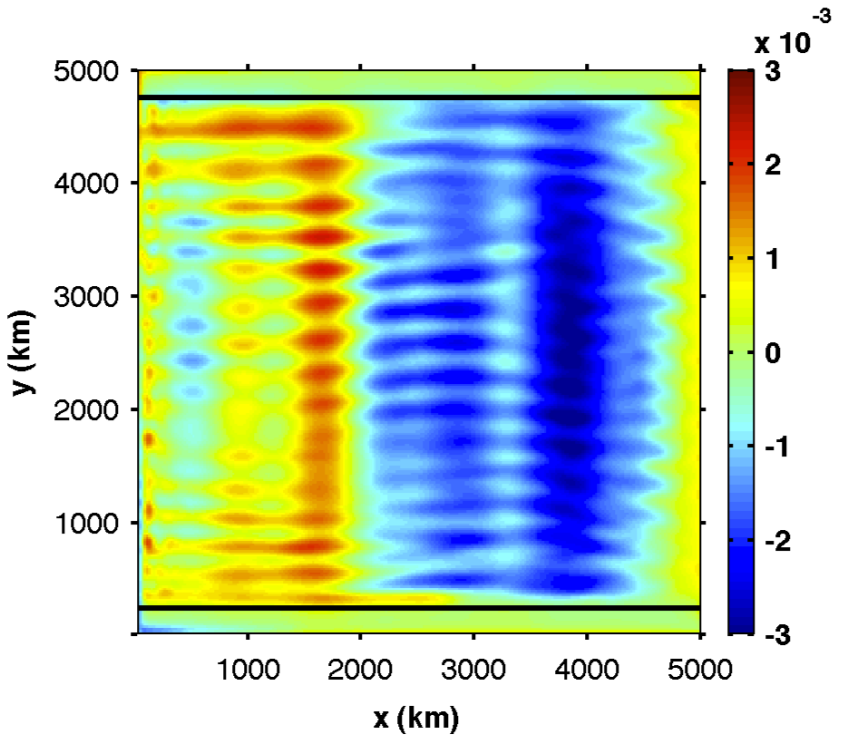


Figure 3.12: Map of the 200-week average of the non-dimensional upper-layer streamfunction, ψ_1. The averaging in time causes the zonal tongues that develop on the large scale Rossby wave to blur as they transit the basin, resulting in bands of alternating zonal motion. The bold black lines mark the edge of the dissipative sponge layers.

3.2.5 Scale of jets and sensitivity to forcing amplitude

The jets in Figure 3.11 have dominant meridional scale that we might expect is set by the most unstable meridional wavenumber of the primary Rossby wave instability. From Lacasce and Pedlosky (2004), for a free large-scale Rossby wave in the infinite domain, the exponential growth rate, in terms of meridional wavenumber l, is given by

$$\sigma = (h_1 h_2)^{1/2} \, lV(x) \left(\frac{F - l^2}{F + l^2} \right)^{1/2}, \tag{3.12}$$

where $V(x)$ is the meridional velocity scale of the plane baroclinic Rossby wave. This is almost identical to the corresponding growth rate for broad meridional flow in equation (2.59) but the unequal layer depths have been factored in. The maximum growth rate

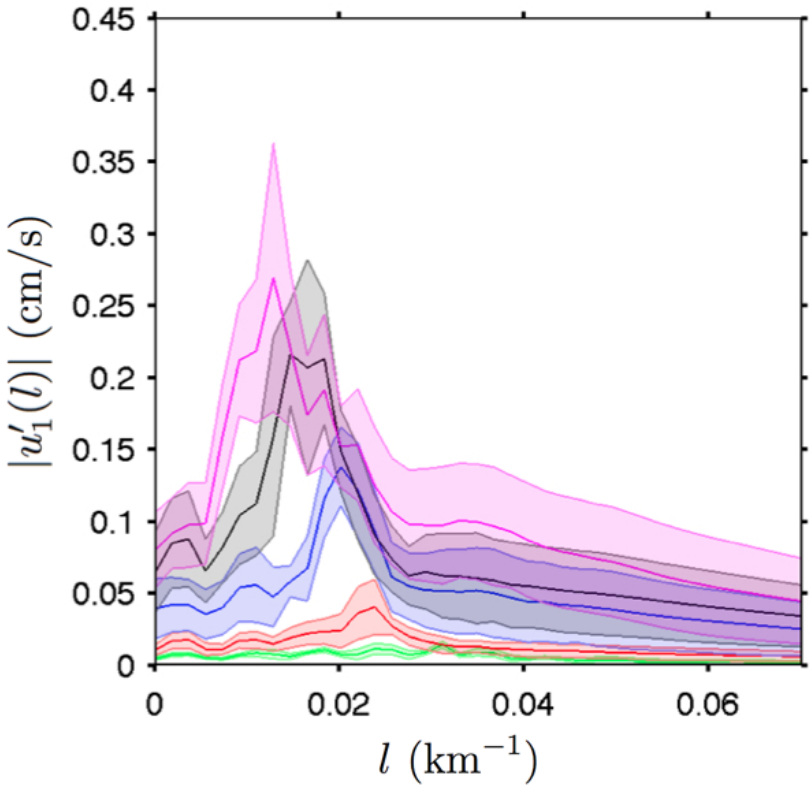


Figure 3.13: Meridional wavenumber spectra of the 200-week mean upper-layer velocity anomaly in the stochastic forcing simulations with $\sigma_{W_s} = \sigma_{\text{ref}}$ (blue), $\sigma_{W_s} = 0.2\,\sigma_{\text{ref}}$ (green), $\sigma_{W_s} = 0.4\,\sigma_{\text{ref}}$ (red), $\sigma_{W_s} = 2.5\,\sigma_{\text{ref}}$ (black) and $\sigma_{W_s} = 5\,\sigma_{\text{ref}}$ (magenta). The shaded area shows the standard deviation of the independent spectra used to produce each mean spectrum.

occurs at the wavenumber

$$l_{\text{max}} = (2^{1/2} - 1)^{1/2}\, F^{1/2} \tag{3.13}$$

and therefore we expect the meridional wavelength, λ_{jet}, of the emerging jets to be proportional to the deformation radius, specifically

$$\lambda_{\text{jet}} \approx 9.76\, L_d. \tag{3.14}$$

Figure 3.13 shows the meridional wavenumber spectra of the 200-week average of zonal surface velocity anomaly, averaged over 10 independent periods, for five different levels of forcing (prescribed as the standard deviation of $W_s(t)$). The blue line in Figure 3.13 is

the mean zonal velocity spectrum of the reference run shown in Figures 3.11, 3.9 and 3.12. The peak of the spectrum was taken to determine the dominant meridional scale of the jets. The stochastic-only simulation was repeated for a for a range of deformation radii and the dominant jet wavelength for each is plotted in Figure 3.14. The dominant wavelength of the emerging jets appears to scale relatively uniformly with the deformation radius, in agreement with (3.14), except at lower vaues of the deformation radius. This is because for these small values of the deformation radius, the scale of the most unstable wave becomes comparable with the grid spacing and are poorly resolved because disturbances on the order of the grid spacing are preferentailly damped by the implicit diffusion (which is associated with the advection scheme, see Appendix A).

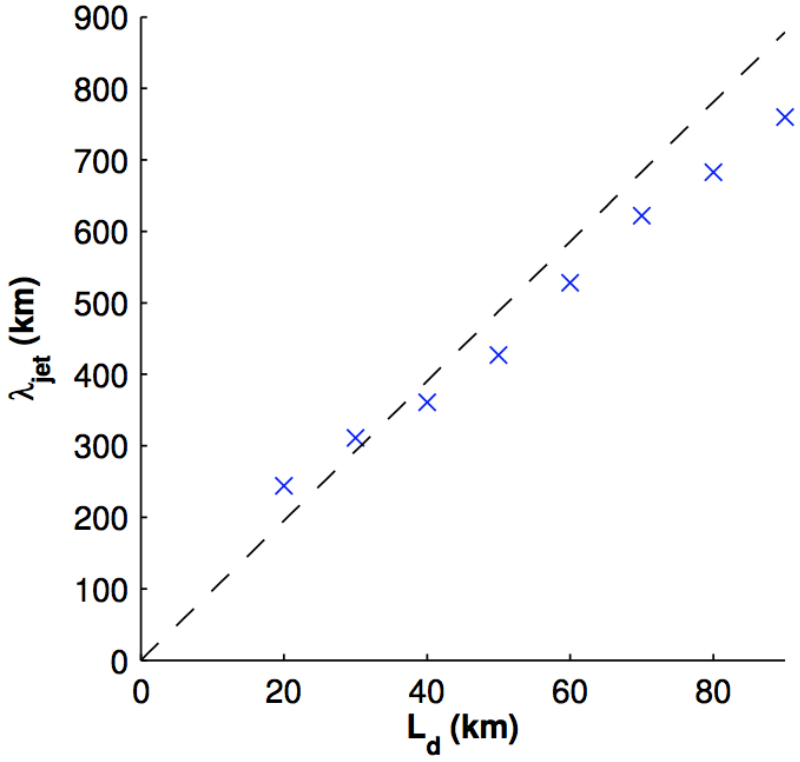


Figure 3.14: Plot of the jet wavelength, λ_{jet}, for various values of the deformation radius, L_d, for the stochastic-only forcing experiments. The wavelength of the jets is taken from the peak of the meridional wavenumber spectra (e.g. Figure 3.13).

For the reference stochastic-only forcing simulation we find the zonal perturbations, that develop on the basin Rossby waves, to be themselves only weakly unstable in the period it takes the wave to cross the basin. However, if the jets had a stronger shear,

we would expect to observe more unstable growth and more turbulent behaviour. To test this hypothesis we repeated the same stochastic experiment but increased the standard deviation of $W_s(t)$ to 2.5, 5 and 10 times that used in the reference simulation. The meridional wavenumber spectra for the increased forcing simulations are plotted in Figure 3.13; these were calculated in the same way as the spectrum of the reference simulation. The peak velocities increase with the forcing amplitude, as expected since the velocity shear of the Rossby waves increases. The spectral peak also shifts to smaller wave numbers and broadens, indicating an increase in the dominant meridional scale of the upper-layer zonal velocity.

The shift towards small wave numbers seen in Figure 3.13 is familiar from studies of purely two-dimensional turbulence (Fjortoft, 1953; Rhines, 1979). For two-layers and a flat bottom, energy cascades towards the scale of the deformation radius where baroclinic instability growth occurs and energy is transferred into the barotropic mode (Salmon, 1978). The linearised model of baroclinic instability discussed in section 2.1.5 is a special case of a more general tendency to generate barotropic kinetic energy at the expense of baroclinic potential energy. Thereafter, the energy in the barotropic mode cascades to larger scales as in the purely two-dimensional case. This comparison can be made explicitly in equation (2.23) if one considers the Jacobian involving the self-interaction of the baroclinic mode to be a "stirring term" that forces the barotropic PV evolution.

An inverse cascade should favour the barotropic mode, whereas we find that a significant amount of kinetic energy remains in the baroclinic mode, even in the 200-week averages. One explanation is that having a thinner upper layer hinders the transfer of energy to the barotropic mode as has been found in previous two-layer turbulence studies (Smith and Vallis, 2002; Arbic and Flierl, 2004; Scott and Arbic, 2007). This can be understood by considering the stirring term of the barotropic mode that appears in (2.23), it is largest when $h_1 = h_2$ but decreases for non-uniform stratifications and the stirring by the baroclinic mode is effectively reduced. Bottom friction however, has a similar effect (LaCasce and Brink, 2000), and this could also be the cause. Vertically asymmetric damping (i.e. $r_1 < r_2$), as we have used here, preferentially damps the lower layer which generates a baroclinic component from a purely barotropic flow and acts to retain energy in the baroclinic mode. In any case, these experiments suggest that the forcing amplitude affects the scale of the jets, albeit weakly, increasing it beyond the deformation radius predicted by linear theory.

But there is a limit. Increasing the amplitude to 20 times the reference value results in

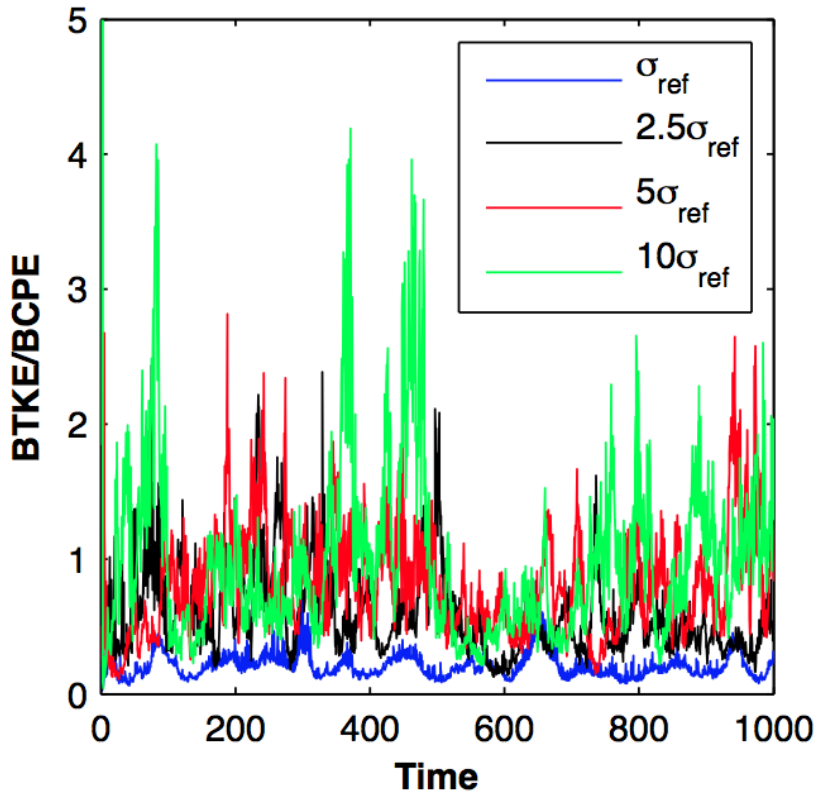


Figure 3.15: Ratio of barotropic kinetic energy to baroclinic potential energy in the stochastic-only forcing experiments for various values of the Ekman pumping standard deviation, σ_{W_s}. The larger ratios indicate that there is a cascade of energy to the barotropic mode with increased forcing. The time is in non-dimensional model units.

no discernible jets in the 200-week averages. In this case the resulting eddy field is largely barotropic and isotropic. This is the limit considered by LaCasce (2002) and seen also in LaCasce and Pedlosky (2004).

Figure 3.15 shows the time evolution of the ratio of barotropic kinetic energy to baroclinic potential energy for different forcing levels in the stochastic-only forcing simulations. With increased forcing it is clear that the energy is being more efficiently converted from the baroclinic mode to the barotropic mode. The increased forcing allows the zonal tongues to become unstable, and through this instability a greater proportion of the energy in the baroclinic mode is being transferred to the barotropic mode.

For completeness, the simulation was performed with smaller values of the forcing and as before their meridional wavenumber spectra are plotted in Figure 3.13. The baroclinic

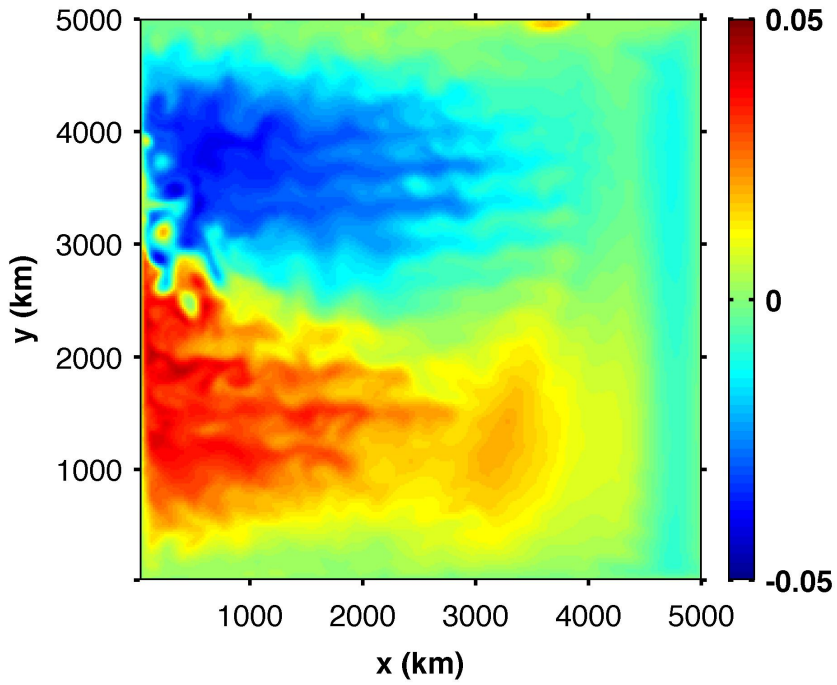


Figure 3.16: Snapshot of the baroclinic streamfunction, τ, in the mean and stochastic forcing simulation. The baroclinic Rossby waves can be seen emanating from the Eastern boundary and being "bent" by the barotropic advection. Zonal tongues similar to those observed in the stochastic-only simulations are apparent in the middle part of the large scale gyres.

Rossby waves generated by the weaker stochastic forcing have weaker shear and the primary instability growth on the meridionally orientated wave is slower. This is clear from the very small peak in the $\sigma_{W_s} = 0.4\,\sigma_{\text{ref}}$ simulation and the lack of an obvious peak in the $\sigma_{W_s} = 0.2\,\sigma_{\text{ref}}$ spectrum, where there is no significant instability growth on the Rossby waves in the basin transit time.

3.3 Mean and stochastic wind forcing simulations

We now examine the response of the model to the mean double gyre Ekman pumping pattern applied in addition to the large-scale stochastic forcing, as in equation (3.3). The addition of the mean double gyre wind forcing complicates the dynamics by driving a mean flow but the large-scale stochastic forcing will continue to excite Rossby waves at the eastern boundary. We anticipate that the propagation of the low frequency basin modes will be influenced by the advection of the barotropic mean flow (e.g. Ben Jelloul and Huck, 2005) and that the interaction with the mean flow will generate greater spatial inhomogeneity in comparison to the stochastic-only forcing results. The mean component of the forcing generates a mean circulation in the opposite sense to the inertial circulation gyres in Figure 3.4 and as a result their emergence is much weaker (as found, for example, by Griffa and Salmon (1989)). As such, sponge layers were not applied to the model for the simulations with mean and stochastic forcing.

3.3.1 Instantaneous and time-averaged flow

The mean wind forcing generates a familiar double gyre circulation, with a cyclonic subpolar gyre circulation to the north and anticyclonic subtropical gyre to the south, as is seen in Figure 3.16 which is a snapshot of the baroclinic streamfunction during the mean and stochastic forcing simulation. A Rossby wave that meridionally spans the basin is seen emanating from the eastern boundary, as in the stochastic-only forcing simulation, and the Rossby wave instability is apparent in each of the gyres. Towards the centre of the basin the advection of the Rossby waves by the barotropic flow is evident: The westward propagation of the waves is slowed in the central part of the basin, where the mean flow is eastward, and their propagation is accelerated in the northern and southern regions of the basin, where the mean flow is westward. This has the effect of "bending" the waves such that there orientation is no longer purely meridional as in the stochastic-only forcing

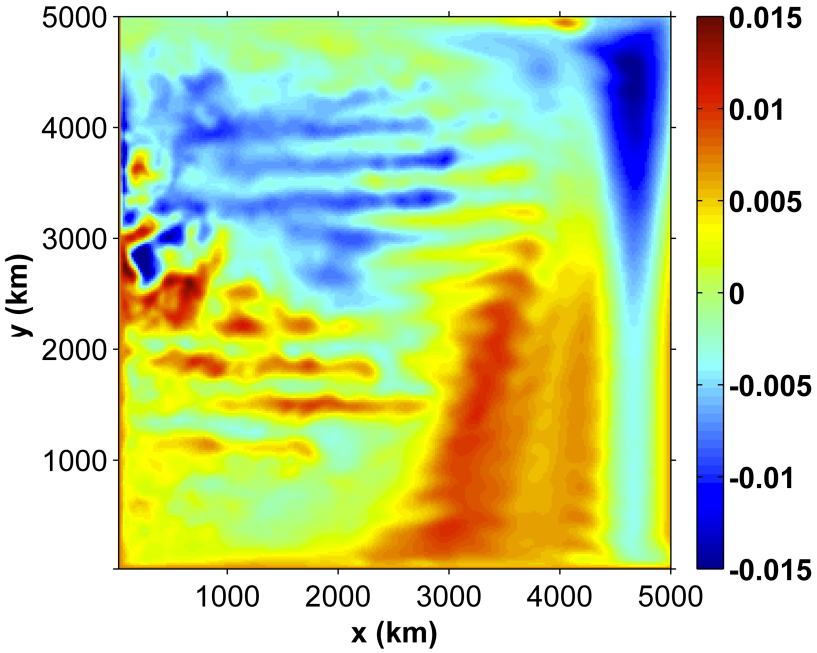


Figure 3.17: 20-week average of the non-dimensional baroclinic streamfunction anomaly, τ', in the mean and stochastic forcing simulation. The development of tongues (slightly tilted from the purely zonal tongues in the stochastic-only simulations) is visible on the large-scale Rossby wave which is noticably doppler-shifted by the double-gyre mean flow.

simulations. The growth of instability tongues is less clear than in the snapshots of the stochastic-only forcing simulations (e.g. Figure 3.9) but nonetheless still evident. It is interesting that the instability appears to be not purely zonal but also tilted very slightly following the bending of the Rossby waves by the mean flow. When the flow is not purely meridional the instability growth is largest in an intermediate direction between the angle of maximum available potential energy, which is perpendicular to the Rossby wave front, and latitude circles of constant planetary vorticity (e.g. Pedlosky, 1982). This is shown more clearly in Figure 3.17, which show a 20-week mean of the baroclinic streamfunction anomaly. The 20-week mean is taken to filter out the higher frequency wave motion and essentially represents a "smoothed" snapshot of the instability evolution.

The surface zonal velocity anomaly (defined as the departure from the 115-year mean), averaged over 200-weeks, is plotted in Figure 3.18. The alternating jets are again clearly visible, extending across the gyres, but now their appearance is more spatially dependent than in the stochastic-only forcing simulations. The contours in Figure 3.18 show the mean

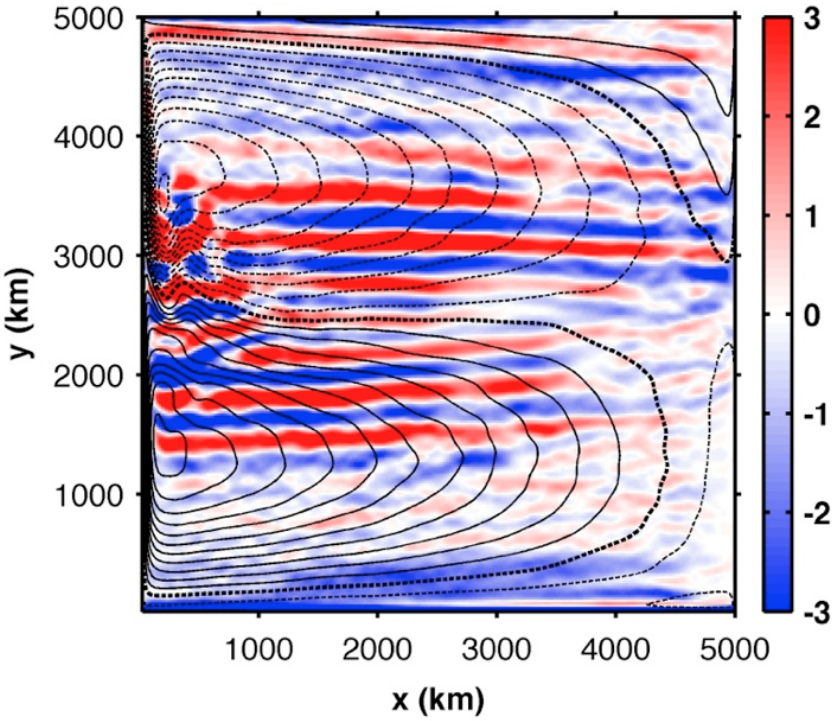


Figure 3.18: Map of the upper-layer zonal velocity anomaly, u_1' (cm/s), in the mean and stochastic forcing simulation averaged over 200 weeks. The mean barotropic streamfunction (averaged over the 115-year model integration) is plotted with a contour interval of 8×10^3 m^{2}s^{-1} and the solid and dashed contours indicate positive and negative values respectively, with the zero contour in bold.

barotropic flow (averaged over the 115-year simulation). In the middle part of the basin, where the mean flow is eastwards, the jets are stronger because the barotropic flow acts to slow the propagation of the waves and effectively allows the instability more time to develop. In contrast, where the mean flow is eastward, in the north and south of the basin, the Rossby wave speeds are augmented and the instability has less time to develop whilst the wave transits the basin.

In a sense, the weakening of the jets on the flanks of the gyres is consistent with the results of the increased averaging period in the stochastic-only forcing simulations. In Figure 3.11 the jets are seen to become weaker as the averaging period becomes comparable to the transit time of the baroclinic Rossby waves. The increased averaging period reduces the signal from the individual zonal tongues in the measurement. Where the barotropic mean flow is westwards, in the north and south of the basin, the ratio of the averaging period

to the transit time is much larger than the region of westward mean flow, so the effective projection of the baroclinic instability tongues on the surface flow is reduced.

Interestingly, the meridional scale of the jets increases westwards, where the flow, near the separated boundary currents, is more energetic. The amplitude of the jets is also seen to increase in this region, which is consistent with the modest inverse cascade of energy in the baroclinic mode observed in the stochastic-only simulations with increased forcing.

3.3.2 Meridional tilt of zonal jets

Another aspect, in contrast to the stochastic-only simulations, is that the time-averaged jets appear to tilt in the interior. The direction of the tilt is in the direction of the mean flow and reflect the distortion of the potential vorticity contours by the mean flow. Figure 3.19 shows the zonal velocity anomaly averaged over 200-weeks plotted against contours of the mean lower-layer potential vorticity, Q_2, given by

$$Q_2 = \beta y + h_1 F \bar{\tau} \tag{3.15}$$

where the overbar indicates the average over the whole simulation.

The mean flow distorts the contours of Q_2 from latitude lines of βy, tilting them in the direction of the mean flow. The lower-layer of the model is unforced, so time averaged fluid motion in the lower-layer is constrained by the Q_2 contours. This is not the case in the upper-layer where the mean forcing permits motion across the upper-layer potential vorticity contours. The zonal jets in Figure 3.19 seem to closely follow the Q_2 contours in the interior. They deviate somewhat approaching the western boundary where the flow is more turbulent. Here, the variability of the lower layer potential vorticity is larger, due to the more energetic flow, and as such the motion is less constrained by the mean potential vorticity contours.

It is notable that the tilt of the jets that emerge with mean and stochastic forcing differs from the tilt of the instability tongues in the instantaneous snapshots of the baroclinic streamfunction (e.g. Figure 3.16). The instability initially grows with a tilt that maximises the extraction of available potential energy from the Rossby waves, opposite to the mean flow. Similar to the stochastic-only simulations, after the initial growth, the zonal tongues are relatively robust to subsequent instability growth. The system of baroclinic instability tongues propagates westwards, with the tongues closely following the lower layer potential

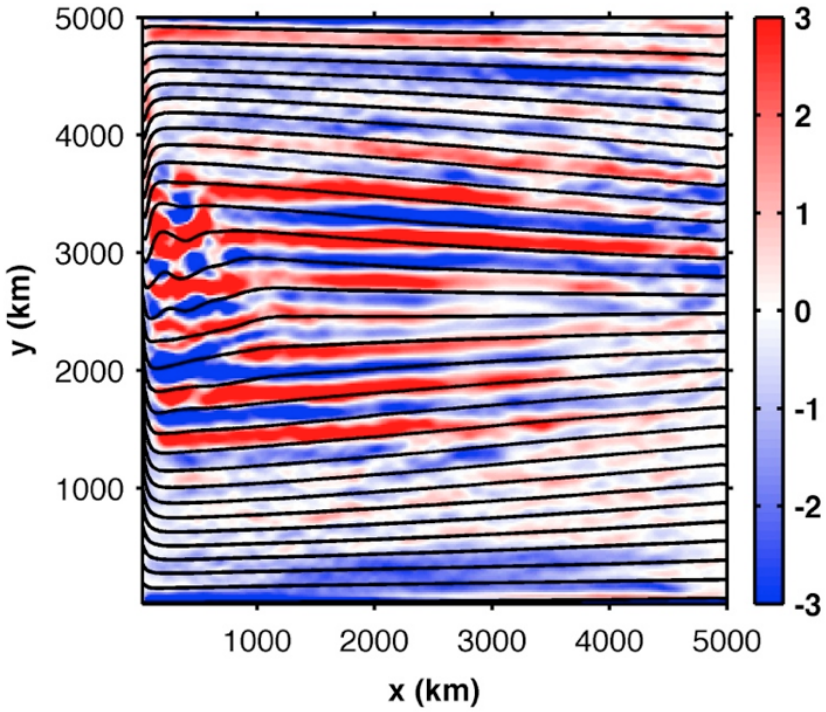


Figure 3.19: Map of the upper-layer zonal velocity anomaly, u_1' (cm/s), in the mean and stochastic forcing simulation averaged over 200 weeks. The mean lower layer potential vorticity, Q_2, is contoured.

vorticity contours, resulting in meridional tilt in the direction of the mean flow.

3.3.3 Comparison with mean-only simulations

For comparison, a simulation was performed with only the mean double-gyre wind forcing component in (3.3). Figure 3.20a shows the 200-week average of the zonal velocity anomaly and reveals no clear alternating zonal features in the interior of the basin, only large anomalies in the vicinity of the western boundary, which is shown in Figure 3.20d. The mean stream function, in Figure 3.20b, reveals a mean flow that is somewhat different from the mean and stochastic forcing simulation. In the mean-only simulation, strong recirculation gyres spin-up at the western boundary on either side of the emerging western boundary jet. This jet is much weaker in the simulation with mean and stochastic forcing and the recirculation gyres are not present. The circulation in the interior of the ocean is similar in both simulations, being slightly weaker in the presence of mean and stochastic

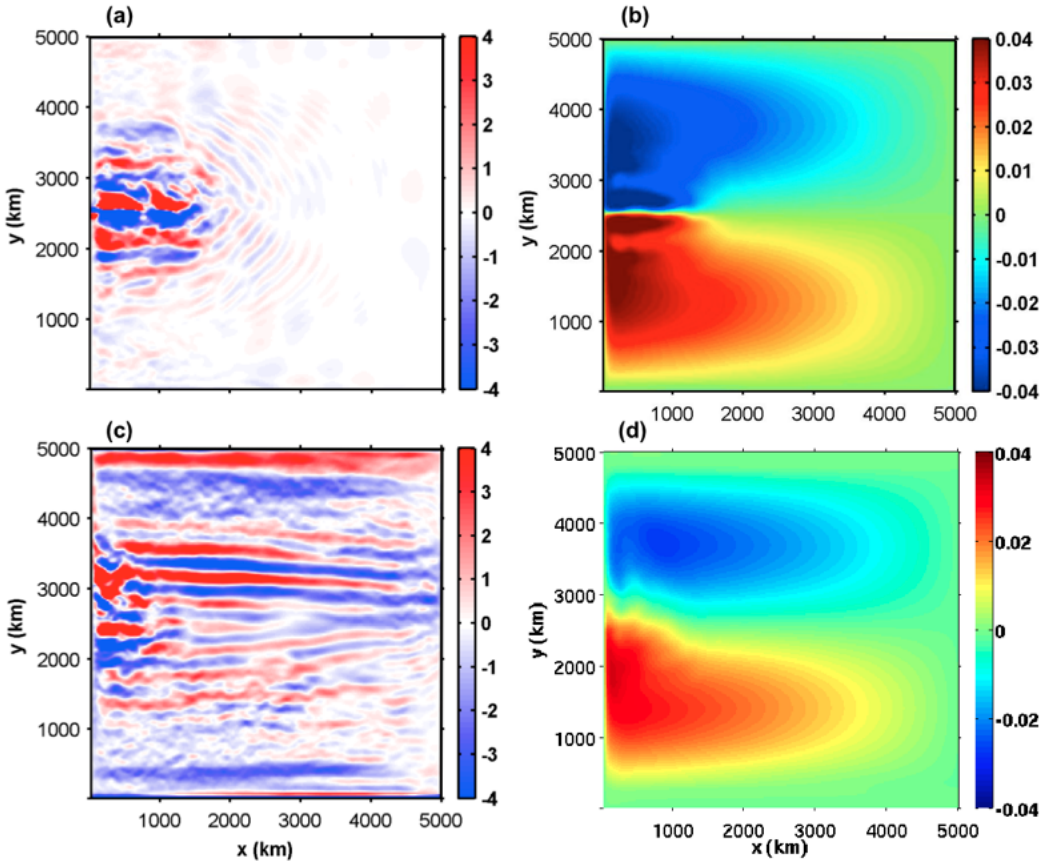


Figure 3.20: (a) Map of the upper-layer zonal velocity anomaly, u_1' (cm/s), in the simulation with mean-only forcing, averaged over 200 weeks. (b) Map of the mean non-dimensional baroclinic streamfunction, $\overline{\tau}$, in the simulation with mean-only forcing. (c) and (d) are the same as (a) and (b) respectively but for the mean and stochastic forcing simulation.

forcing. This indicates that zonal anomalies that are generated on the Rossby waves also remove available potential energy from the large-scale flow, which weakens the gyres in the interior. The notion that the zonal jets are growing at the expense of the mean flow available potential energy is also supported by the relative weakness of the zonal jets across the central latitude of the basin, where $\overline{\tau} \approx 0$, and there is negligible available potential energy in the mean flow. By comparison, the strongest jets in Figure 3.20d occur in the region of the sub polar gyre with an eastward mean flow but with a larger zonal gradient, and therefore larger available potential energy, in the mean baroclinic streamfunction. Nonetheless, comparison with the mean-only simulations demonstrates that the instability of the large-scale baroclinic Rossby waves generated by the stochastic forcing component is crucially important in the emergence of alternating zonal jets in this model.

3.4 Discussion and summary

Our QG simulation of basin-scale stochastic forcing with zero time mean, a simple model of the NAO, produces zonal jet structures similar to those recently found in observations. The study of the influence on the interior ocean is in contrast to all previous literature on the response of the North Atlantic to NAO forcing of the ocean (e.g. Frankignoul *et al.*, 1997; Marshall *et al.*, 2001). This model is highly idealised, however, and is also relevant to the North Pacific ocean which is subject to similarly large-scale stochastic forcing. In the simulations described here, the wind forcing excites baroclinic Rossby waves emanating from the eastern boundary. As these propagate westward they become unstable, producing a secondary wave with long zonal extent. If one averages the surface fields in time, the latter appear as distinct, alternating jets. In most cases, the meridional scale of the jets is set by the most unstable meridional wavelength of the instability, which scales with the deformation radius as predicted from linear instability theory. However with stronger forcing, the unstable growth rate is larger and the resultant eddy field is more energetic. This is found to generate a moderate inverse energy cascade, increasing the dominant length scales with increased stochastic forcing.

The baroclinic waves equilibrate for the lower levels of stochastic forcing because the zonal pertubations that grow on the large-scale meridional Rossby waves (driven by the stochastic forcing) are not as susceptible to baroclinic instability as the equivalent meridional flow (as discussed in Chapter 2). The meridional gradient of planetary vorticity essentially

acts to stabilise zonal flows with a relatively weak vertical shear. We find that this occurs for stochastic forcing from 0.4 to 5 times the refernence value, which was tuned to match the large-scale stochastic wind forcing of the North Atlantic. This broad range of parameters indicates that in the real world and as such we might expect this mechanism to be relevant in the North Atlantic. The mechanism is fairly general, so as such it is obviously possible that the mechanism may also be relevant in the North Pacific.

The alternating zonal jets are also found when a mean component of the winds is added to the stochastic forcing. The former generates a double gyre system with their associated western boundary currents. The mean gyres affect the jet formation by altering the propagation speed of the primary baroclinic waves. Where the mean flow is eastward, the waves are slowed, allowing more time for the instability to grow. The gyres also modify the orientation of the jets by deforming the PV contours in the lower layer. The jets are then approximately aligned with those contours. A similar tilting was observed by Maximenko *et al.* (2008) in the interior of ocean gyres. In simulations with mean-only forcing no discernible jets emerge in the ocean interior, highlighting the importance of the large-scale stochastic forcing in determining their emergence in this model.

An important distinction exists between the jet-like features observed in our basin simulations and the β-plane jets found in a periodic domain (Rhines, 1975; Vallis and Maltrud, 1993). The latter span the domain zonally, like the rings of Jupiter. The jets seen in our simulations are in fact waves, with long zonal scales. Averaging the fields in time blurs the zonal dependence, giving them the appearance of jets. But averaging them over progressively longer times weakens their signature, as indeed is found in observations (e.g. Maximenko *et al.*, 2005). With infinite averaging times, the features necessarily disappear. As a result, a finite averaging period is key to the meridional arrangement of zonal instability tongues giving rise to alternating bands of zonal velocity. In this sense, our mechanism thereby offers a possible explanation of the vorticity budget analysis by Melnichenko *et al.* (2010) in which the vortex stretching term was found to be important in maintaining the "jets". The propagation and slow growth of the zonal tongues generates large variations in the interfacial height, a proxy for the thermocline in our idealised model, and could generate the required vortex stretching squeezing observed in the upper ocean. This hypothesis is also supported by the study of Maximenko *et al.*, (2008) who observe the strongest alternating zonal signal near to the depth of the thermocline.

We note that the mechanism described here is likely to have a strong dependence on

latitude. As highlighted by Lacasce and Pedlosky (2004), the ratio of the timescale of the instability growth to the transit time of the baroclinic Rossby waves is proportional to $\beta {L_d}^3$, in which both terms decrease with latitude (e.g. Chelton *et al.*, 1998). At lower latitudes the Rossby waves can transit the basin before succumbing to the instability and therefore, this mechanism is most likely relevant at midlatitudes. As noted in the chapter 2 though, an unstable eastern boundary current can produce similar features (Hristova *et al.*, 2008; Afanasyev *et al.*, 2011). Such currents are precluded in our idealised model set up but it could be that both mechanisms are at play in the ocean, with the present one producing jets in the interior and the boundary currents producing them in the eastern part of the domain.

Chapter 4

Covariability of the Kuroshio Extension jet and SST front

In this chapter we aim to characterise the covariability of the Kuroshio Extension temperature front with the Kuroshio Extension jet. The Kuroshio Extension jet has been shown to have a dominant low frequency variability in previous studies, as outlined in Chaper 2, and we wish to investigate how this is related to the variability of the Kuroshio Extension front. The interest in the variability of the SST front is in part motivated by the various modelling studies, also discussed in Chapter 2, that suggest that the midlatitude SST *gradients* plays an important role in determining the downstream atmospheric circulation.

4.1 Datasets

The SSH data used in this study are "the delayed-time updated maps of absolute dynamic topography" available daily on a 1/3° mercator grid produced by AVISO[1]. Available from October 1992 to January 2011, this is a merged dataset utilising altimeter data from the Cryosat-2, Jason-1, Jason-2, Topex/Poseidon, Envisat, GFO and ERS1/2 missions, at all times utilising merged datasets from between two and four missions at any one time (e.g. Ducet *et al.* 2000). Therefore the quality of the dataset is not homogenous but represents the best estimate from the available altimeter data. The absolute dynamic topography (ADT) is the part of the SSH that can be deemed dynamically important to the oceanic flow and is

[1]The altimeter products were produced by Ssalto/Duacs and distributed by Aviso, with support from Cnes (http://www.aviso.oceanobs.com/duacs/).

produced by adding the sea level anomaly (SLA) to the mean dynamic topography (MDT):

$$\text{ADT} = \text{SLA} + \text{MDT}. \tag{4.1}$$

The mean dynamic topography is the mean sea level height minus the contribution from the geoid, which is a map of the theoretical sea surface height of the oceans only under the influence of the Earth's gravitational field. The daily maps are produced by interpolating data at coarser temporal resolution (on the order of a week) but we use the daily maps to match the SST data product.

The SST dataset we use is the "optimally-interpolated AMSR-AVHRR" available with a 1-day temporal resolution on a 1/4° mercator grid from the National Oceanic and Atmospheric Administration (NOAA) National Climatic Data Centre (NCDC)[2]. The dataset combines high resolution infra-red observations from the Advanced Very High Resolution Radiometer (AVHRR), the microwave satellite data from the Advanced Microwave Scanning Radiometer (AMSR) as well as in situ data from ships and buoys which are used to adjust systematic biases in the satellite data (Reynolds, 2007). The microwave data has the advantage of being robust to local weather features (i.e. can "see through" clouds whereas the infrared instrument cannot) but is a more recent mission and as such this dataset is only available from June 2002 through October 2011. The high resolution AVHRR data is particularly useful in regions near to land, where AMSR measurements are not available, as well as reducing errors in regions where data from both instruments is available. In three days the AMSR covers 95% of the world ocean, compared to about 40% coverage in a single day (Chelton and Wentz, 2005), but we will use the optimally-interpolated daily product to match the temporal resolution of the SSH dataset.

The daily SSH data, $\eta(x, y, t)$, is used to calculate maps of the surface geostrophic velocity, $\mathbf{u}_g(x, y, t)$:

$$\mathbf{u}_g = (u_g, v_g) = \frac{g}{f}\left(-\frac{\partial \eta}{\partial y}, \frac{\partial \eta}{\partial x}\right), \tag{4.2}$$

where the variables have the usual meaning. To analyse the relationship between western boundary current jet variability and the variability of the associated SST front we will use maps of the magnitudes of the two vector fields, $|\mathbf{u}_g|(x, y, t)$ and $|\nabla T|(x, y, t)$ respectively.

[2]The SST data was downloaded from
http://iridl.ldeo.columbia.edu/SOURCES/.NOAA/.NCDC/.OISST/.version2/.AVHRR-AMSR/.

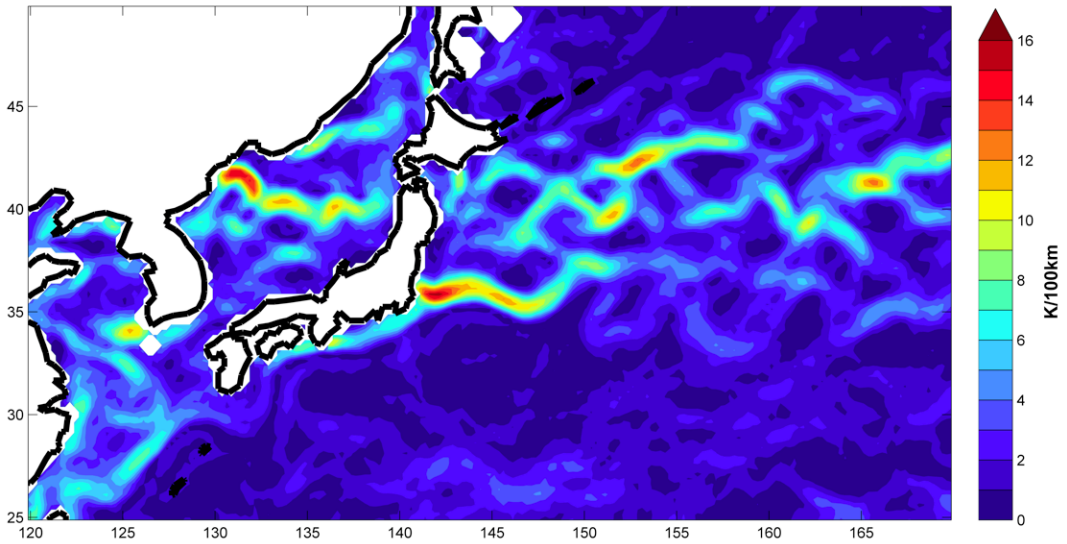


Figure 4.1: The magnitude of the SST gradient, in units of °C/100km, averaged over the boreal winter of 2004 (i.e. the average of the gradient magnitude, $\overline{|\nabla T|}$) from the optimally-interpolated AMSR-AVHRR daily SST dataset (Reynolds, 2007).

Figures 4.1 and 4.2 show maps of scalar magnitudes of the SST gradient and geostrophic velocity fields calculated from the SSH and SST datasets, averaged over the boreal winter of 2004 (i.e. December 2004 to February 2005). The Kuroshio Extension appears as a clear maximum in the geostrophic velocity magnitude and the magnitude of the SST gradient also exhibits a strong associated maximum. The seasonal mean, rather than the long-term mean, has been plotted to emphasise the correspondence between the two fields on the seasonal timescale. To the north of the Kuroshio Extension front there are additional large temperature fronts associated with the Oyashio current but the association between the current magnitude and magnitude of the SST gradient is not as clear. As such we choose to focus on the relationship between the Kuroshio Extension jet and front variability.

4.2 Maximum covariance analysis

To investigate the covariability between the anomalous fields of geostrophic velocity magnitude, $|\mathbf{u}_g|'(x, y, t)$, and SST gradient magnitude, $|\nabla T|'(x, y, t)$, in the Kuroshio Extension region during the period which we have data for (i.e. June 2002 to January 2011) we use a maximum covariance analysis (MCA) (e.g. Bretherton *et al.*, 1992). The anomaly time series are generated by simply removing the time mean over the period at each day (n.b. no

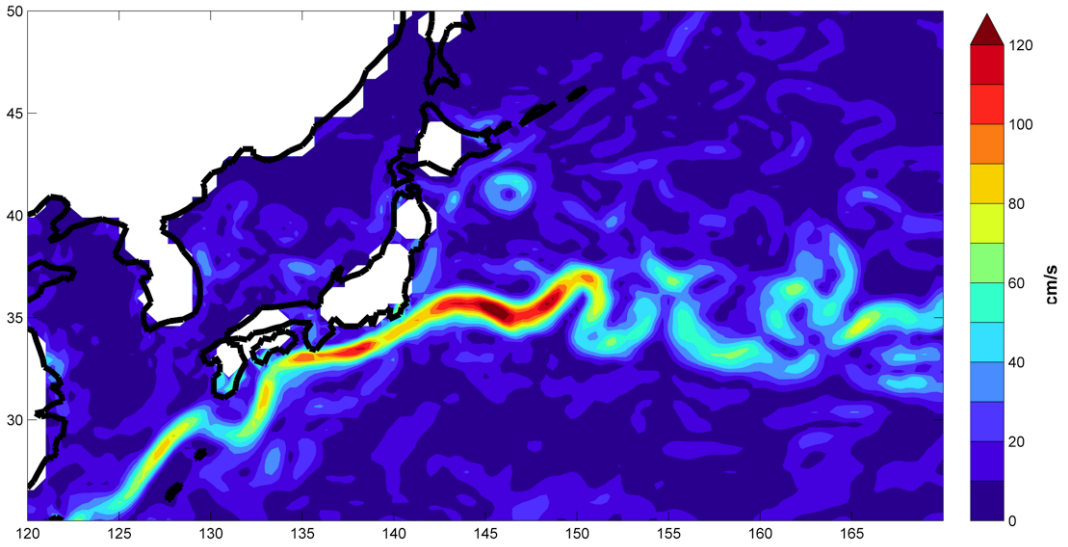


Figure 4.2: The magnitude of the surface geostrophic velocity, in units of cm/s, corresponding averaged over the boreal winter of 2004 (i.e. the average of the velocity magnitude, $\overline{|\mathbf{u}_g|}$) calculated from the SSH fields in the AVISO daily altimetry dataset.

seasonal component is removed, only the long-term mean). Similar to principle component analysis, MCA decomposes the two fields into K orthogonal signals, which for our fields are

$$|\mathbf{u}_g|'(x, y, t - \tau) = \sum_{k=1}^{K} a_k(t - \tau)\, \mathbf{p}_k(x, y), \tag{4.3}$$

$$|\nabla T|'(x, y, t) = \sum_{k=1}^{K} b_k(t)\, \mathbf{q}_k(x, y), \tag{4.4}$$

where a_k and b_k are the expansion coefficient time series for mode k, $\mathbf{p}_k$ and $\mathbf{q}_k$ are the "patterns" of variability of the kth mode and τ is a lag period (i.e. the time by which the velocity field "leads" the temperature field). To decompose the two fields into patterns which maximise the covariability, we first compute the covariance matrix, C_{uT}, between the two fields:

$$C_{uT} = \langle |\mathbf{u}_g|' \, |\nabla T|' \rangle, \tag{4.5}$$

where the angled brackets denotes a time average. The covariance matrix contains values of the covariance between each point in one field and all the points in the other and therefore C_{uT} has the dimensions $N_u \times N_T$, where N_u and N_T are the number of grid points in the

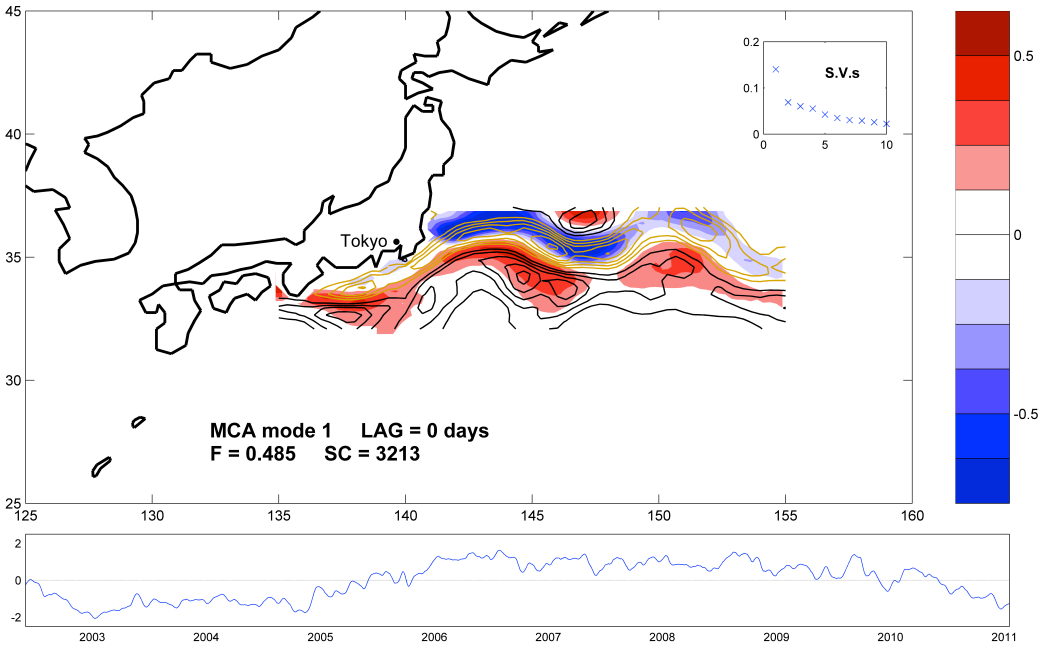


Figure 4.3: The first mode patterns from the MCA of the surface geostrophic velocity magnitude, $|\mathbf{u}_g|(x, y, t)$, and the SST gradient magnitude , $|\nabla T|(x, y, t)$. The velocity pattern ($\mathbf{U}_1$) is contoured at intervals of 5 cm/s (positive in black, negative in gold) and the SST gradient pattern ($\mathbf{T}_1$) is shaded in units of °K/100km, each being equivalent to one standard deviation of the variability. The first ten singular values from the singular value decomposition are plotted and the squared covariance fraction (SCF) is indicated. The corresponding time series time series of the first mode of the MCA, $a_1(t)$, is plotted below (where the time series has been normalised by one standard deviation).

velocity and temperature fields respectively. Using a singular value decomposition (SVD), the covariance matrix can be written as

$$C_{uT} = \sum_{k=1}^{K} \sigma_k \, \mathbf{p}_k \, \mathbf{q}_k{}^T, \tag{4.6}$$

where $\mathbf{p}$ and $\mathbf{q}$ are orthonormal sets of K vectors, corresponding to the patterns of variability in equations (4.3) and (4.4), σ_k are the singular values of the covariance matrix and the superscript T denotes the transpose. The number of vectors in the decomposition, K, is equal to the minimum of N_u and N_T.

A property of the SVD is that the singular values are positive and decrease with increasing mode number, such that σ_1 is the largest and σ_K the smallest. From the definition

of the squared Frobenius norm, the covariance matrix can be written as the sum of the squared singular values:

$$||C_{uT}||_F{}^2 = \text{trace}\left(C_{uT}\, C_{uT}^T\right) = \sum_{k=1}^{K} \sigma_k{}^2, \tag{4.7}$$

therefore the singular values are directly related to the squared covariance "explained" by the kth mode of the expansion in (4.3) and (4.4). By extension, this also indicates the first mode is responsible for the largest amount of the squared covariance and therefore represents the maximum covariance between the two fields. A useful measure is the total squared covariance fraction (SCF) explained by a particular mode,

$$\text{SCF}_k = \frac{\sigma_k{}^2}{\sum_{i=1}^{K} \sigma_i{}^2}, \tag{4.8}$$

although here we will focus on the first mode, which maximises the covariance. It is important to note that whilst MCA is a useful technique, the results should be treated with some caution, particularly because the analysis will *always* produce maps that maximise the covariance between the two fields but this does not imply a causal relationship.

We wish to investigate how the maps of covariance in both fields are associated with the expansion time series $a_1(t)$, rather than dealing with the two time series in (4.3) and (4.4). To do this we analyse the homogenous covariance maps of the velocity field of the first mode, $\mathbf{U}_1$, and the heterogenous covariance maps of the SST gradient field, $\mathbf{T}_1$, that vary with $a_1(t)$. These are determined by projecting the observation time series, $|\nabla T|'(x, y, t)$ and $|\mathbf{u}_g|'(x, y, t)$, onto the normalised $a_1(t)$ time series. The results of the MCA between the magnitude of the geostrophic velocity and SST gradient field in the KE region, at zero lag ($\tau = 0$), are shown in Figure 4.3. The region was chosen to match the region where there is apparently a close correspondence in Figures (4.2) and (4.1). The velocity magnitude variability pattern is contoured and the SST gradient variability is shaded, with the magnitudes of each corresponding to unit standard deviation of the variability. Plotted below is the expansion coefficient time series of the variability, which has been normalised by one standard deviation.

The variability of the velocity pattern is a meridionally orientated dipole-like pattern and is closely matched by the pattern in the SST gradient variability, which is slightly offset to the north of the velocity field. The close correspondence of the fields indicates

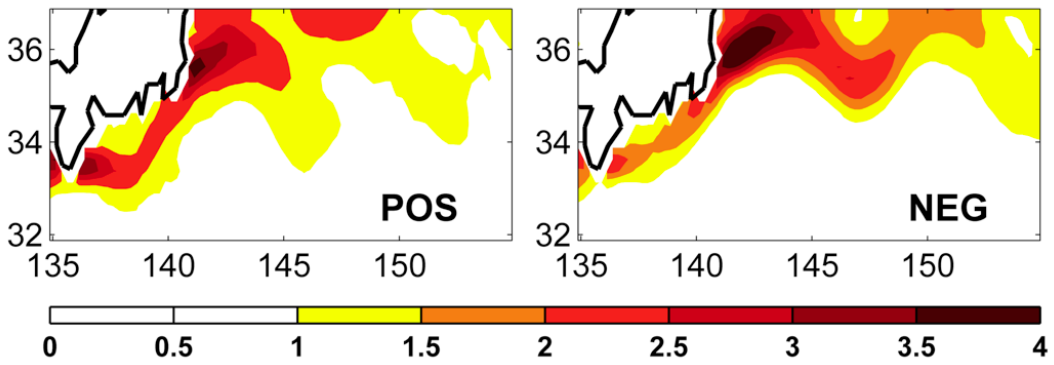


Figure 4.4: The magnitude of the SST gradient, in units of °C/100km, corresponding the positive phase (left) and negative phase (right) of the Kuroshio Extension variability (i.e. the mean plus/minus one standard deviation of the MCA pattern).

that the variability of the front closely follows the velocity field of the KE jet. The first ten singular values of the SVD, also plotted in Figure 4.3, indicate that the first mode is particularly dominant over the other leading modes, accounting for 49% of the total squared covariance. The SST gradient fields corresponding to the positive and negative phases of the dominant mode of variability (i.e. the mean SST gradient magnitude plus/minus one standard deviation of the MCA pattern) are shown in Figure 4.4. The negative anomaly of the SST gradient variability lies along the maximum gradient in the mean field and as such in the negative phase of the variability the SST pattern exhibits a strong, sharp gradient, whereas in the positive phase the SST gradient is weaker and more diffuse. The time series of the first MCA mode (black line in Figure 4.3) is dominated by inter-annual to decadal variability, which is similar to the variability of the KEF strength observed by Chen (2008). From the MCA it is clear that the low frequency variability is related to the state of the KE current: In the positive phase the flow is broader and slower whilst in the negative phase it is narrower and faster, corresponding to the bimodal states of the KE described by Qiu and Chen (2005).

In their analysis of the variability of the Kuroshio Extension jet, Sasaki *et al.* (2013) found that the correlation between the latitude and strength of the jet peaks when its latitude variation leads by 9 months, in previous studies the association between latitude and strength had been reported but not with respect to a lag period (e.g. Qiu and Chen, 2010). To test the dependance of the MCA analysis on the lag period (that is, the response of the SST field a number of days after the velocity field) the MCA analysis was repeated

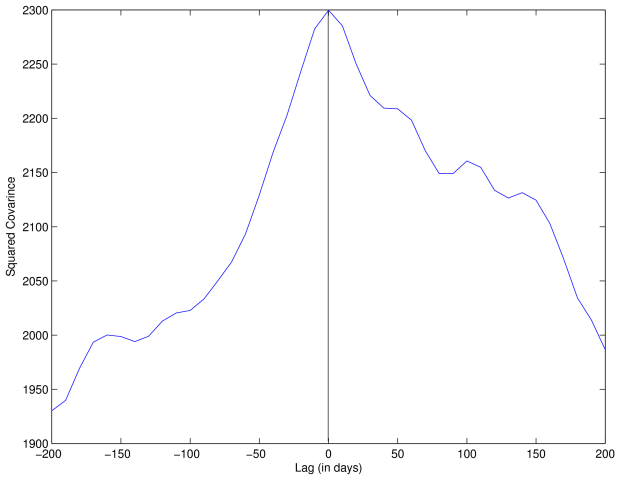


Figure 4.5: Plot of the squared covariance (SC) explained by the first mode of the maximum covariance analysis for the SST field lagging the geostrophic velocity by varying lead-lag periods (i.e. negative lag is where the SST field leads the velocity field)

for increasing lag periods. This is because we are interested in the adjustment of the SST field to changes in the geostrophic currents and the maximum response of the SST field may lag behind the adjustment of the Kuroshio Extension jet. As we increase the lag period the length of the time series from the whole dataset ($\approx$ 3100 days) decreases but this represents a relatively small fraction. The results of this analysis are shown in Figure 4.5, with the SC for the first mode of the MCA plotted for different lead and lag periods. The SC of the first mode is largest at zero lag and then decreases with larger lead and lag periods, implying that the SST gradient and geostrophic velocity fields change in step with one another.

The nature of the covariability between the geostrophic velocity magnitude and the SST gradient magnitude in the Kuroshio Extension region, that emerges from the MCA in this section which peaks at zero lag, seems like a simple thermal wind response in each phase. For a mixed layer in which the temperature and velocity are constant with depth, the thermal wind velocity is related to the temperature gradient as

$$\mathbf{u} \propto \hat{\mathbf{k}} \times \nabla T. \tag{4.9}$$

In the positive phase of the MCA, the velocity along the axis of the Kuroshio Extension is reduced and a weaker SST gradient is observed, whereas in the negative phase the velocity

is larger and the SST gradient is enhanced across the jet.

4.3 Impact of geostrophic advection on anomalous SST fields

The covariance of the geostrophic velocity and SST gradient fields that emerges from the MCA suggests that the changes in the geostrophic currents alters the SST field, which in turn affects the strength and structure of the SST front. The heat budget in the KE region, using satellite altimetry, has previously been analysed by Qiu (2000) over a period during which the Kuroshio Extension moved from a more stable state to a more unstable state and back again. He integrated each of the terms over a larger area than we investigate here (31-37°N and 141-180°E) and used 1° SST resolution. As the Kuroshio moved towards a stable state, the geostrophic advection was found to enhance the SST anomaly in the region and when moving towards the unstable state was found to reduce the SST anomaly. Vivier *et al.* (2002) used a numerical model to study the heat budget over the same region and found similar results for the large-scale SST anomaly.

Following the results of our MCA analysis, we now consider the role of the geostrophic velocity field in determining the nature of the SST *front*. To do so we consider the temperature equation (Frankignoul, 1985) for a simple slab mixed-layer model in which the temperature T and the horizontal current $\mathbf{u}$ are constant throughout a mixed-layer of depth h:

$$\frac{\partial T}{\partial t} + \mathbf{u} \cdot \nabla T = \frac{Q}{h\rho C_p} + \frac{w_{en}(T^- - T)}{h} + \kappa \nabla^2 T. \tag{4.10}$$

The first term on the RHS is the temperature forcing by the heat flux, where Q is the net heat flux into the mixed layer, ρ is the density and C_p is the specific heat of water. The second term is the entrainment of water of temperature T^- into the mixed layer at velocity w_{en} and the third term represents horizontal mixing. From the MCA we anticipate that the anomalous SST field in each phase of the KE variability index will largely be forced by the anomalous geostrophic advection. To simplify the analysis, we only consider the geostrophic contribution to the velocity in the mixed-layer and combine other terms as a residual:

$$\frac{\partial T'}{\partial t} + \overline{\mathbf{u}_g} \cdot \nabla T' + \mathbf{u}_g' \cdot \overline{\nabla T} = -\lambda T' + \text{residual}, \tag{4.11}$$

where λ is a constant damping rate and primes denote departure from a mean value. Here the anomalous surface heat flux term has been approximated as a linear damped function

of the temperature anomaly (e.g. Frankignoul *et al.*, 1998). Defining periods of positive/negative phase as being days on which the KE index in Figure 4.3 is further than plus/minus one standard deviation from zero we can produce composite averages for these phases of the KE index. For these composites, if the average of the residual terms is small, the simplified equation for the temperature anomaly becomes

$$\langle(\mathbf{u}_g \cdot \nabla T)'\rangle_{\text{phase}} = -\lambda\langle T'\rangle_{\text{phase}}, \tag{4.12}$$

where the angled brackets indicate a composite average over a phase of the index.

To test this hypothesis we must first calculate the anomalies, and due to the obvious seasonality in the temperature field we remove a seasonally varying mean. This mean is calculated by producing an annual cycle at each grid point by averaging all the values on each day of the year (e.g. averaging all temperatures on January 1st and so on). The annual cycle is then smoothed by using a 31-day running mean at each point and this is used to generate the time series for the anomalies. This method was used for both the geostrophic velocity and temperature fields, although the seasonal variation was not as significant for the velocity time series. The full advection time series was calculated each day by bilinear interpolation of the velocity field onto the SST grid.

The composite averages of the temperature anomalies for the positive, $\langle T'\rangle_{\text{pos}}$, and negative, $\langle T'\rangle_{\text{neg}}$, phases of the KE index are shown in Figure 4.6. These maps confirm that the MCA index, as we expect, has opposing temperature anomalies in the positive and negative phases but similar patterns. Adding the composite anomalies to the climatological mean of the full SST dataset yields maps for the full composite SST fields and these are shown in Figure 4.7. The full composite SST fields show that the positive and negative phases of the KE index clearly represent a strengthening and weakening of the SST gradient. It is also interesting to note that the KE index does not reflect any particular large-scale SST anomaly but rather a frontal scale variability.

Figure 4.8 shows the composite averaged anomalous geostrophic temperature advection for both phases. The patterns of anomalous advection are large in the vicinity of the KE front and also are opposite in the positive and negative phases, indicating the generation of opposite temperature anomalies in each phase. Visual comparison of the composite averages of the temperature anomalies and the geostrophic advection anomalies suggests that, whilst clearly not a perfect correspondance, the geostrophic advection anomalies are

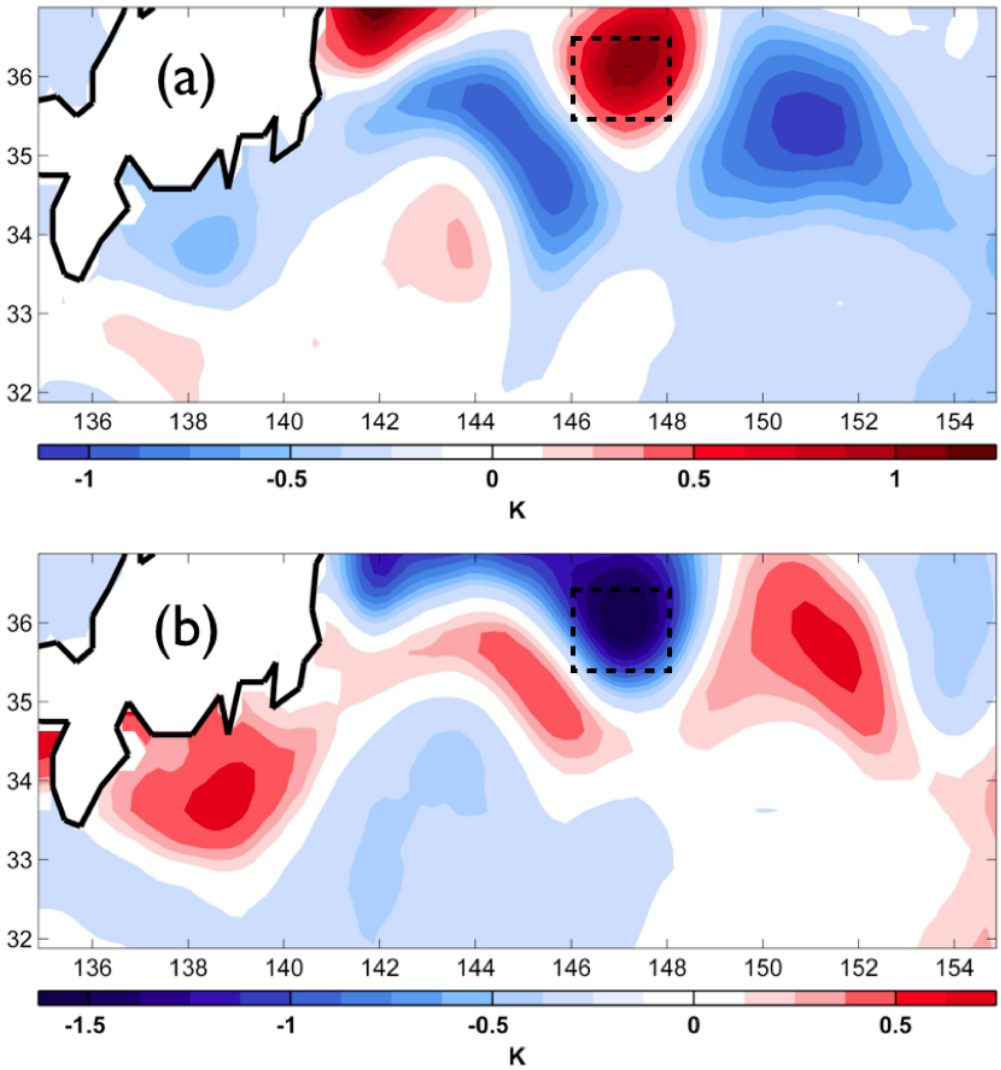


Figure 4.6: The averaged temperature anomaly, $\langle T' \rangle$, in °C (relative to a time-varying mean as defined in the text) for (a) the positive phase and (b) the negative phase of the Kuroshio Extension front index. The box outlined with the bolds dashed line indicated the region of maximum response which was used for the heat flux divergence integral calculation.

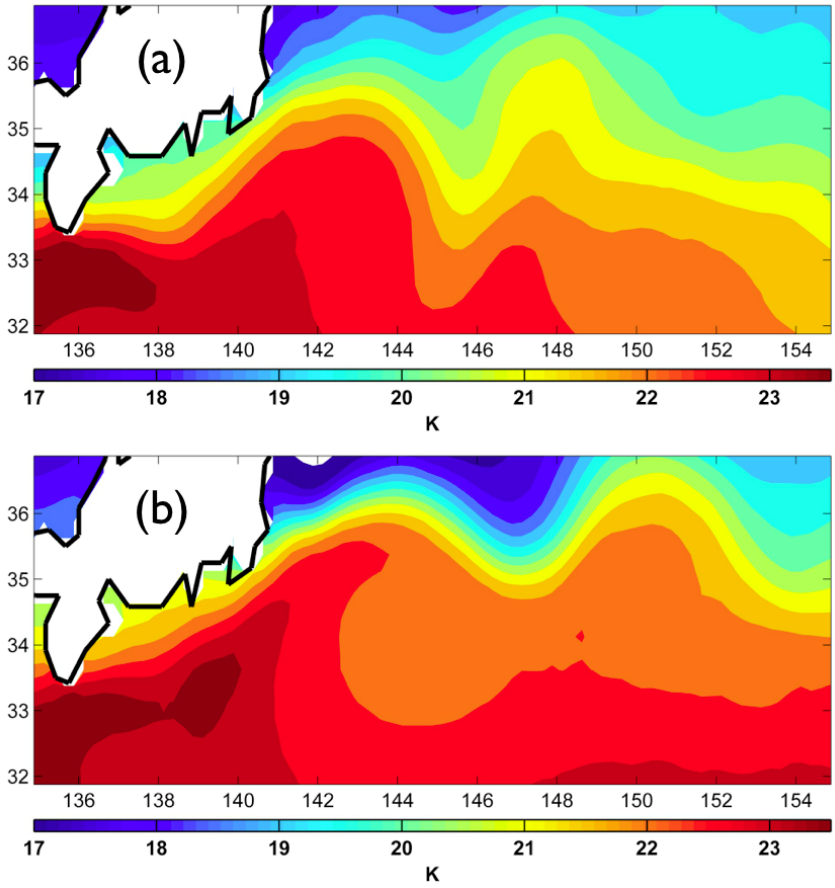


Figure 4.7: The temperature field associated with each phase of the Kuroshio Extension front index generated by adding the temperature anomaly fields shown in Figure 4.6 to the climatology over the SST data period, for (a) the positive phase and (b) the negative phase.

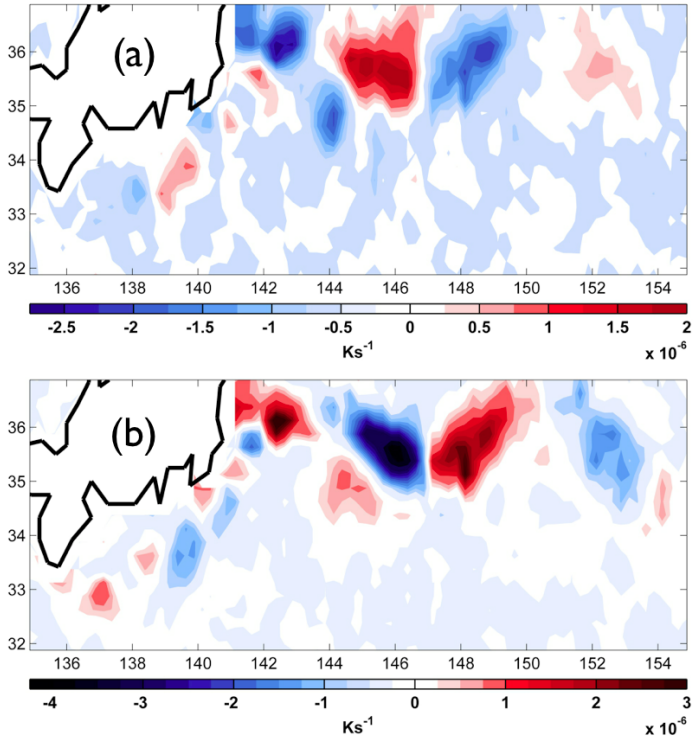


Figure 4.8: The anomalous geostrophic advection term, $\langle(\mathbf{u}\cdot\nabla T)'\rangle$, in K/s averaged over (a) the positive phase and (b) the negative phase of the Kuroshio Extension front index.

anti-correlated with the temperature anomalies in the frontal region which would be the correct sign to maintain the observed SST anomaly. To test this association in the frontal region, 34-37°N and 142-150°E, the values of the temperature anomalies and geostrophic advection anomalies are plotted in Figure 4.9 for both phases of the index. From the cloud of points it is clear the in neither the positive (red crosses) or negative (blue crosses) phases is it appropriate to fit a line of best fit to determine the damping rate. In particular, the cloud of points indicate that the temperature field is somewhat out of phase with the geostrophic anomaly field.

It is perhaps not surprising that the scatter plot in Figure 4.8 is noisy given the small scale of the region of analysis and the finite-differenced approximate derivative used to calculate the advection term. In an attempt to remove the dependence of the results on the spatial derivative, we instead investigate the anomalous heat flux convergence over the region of maximum temperature response, as indicated in Figure 4.6. The integral of the

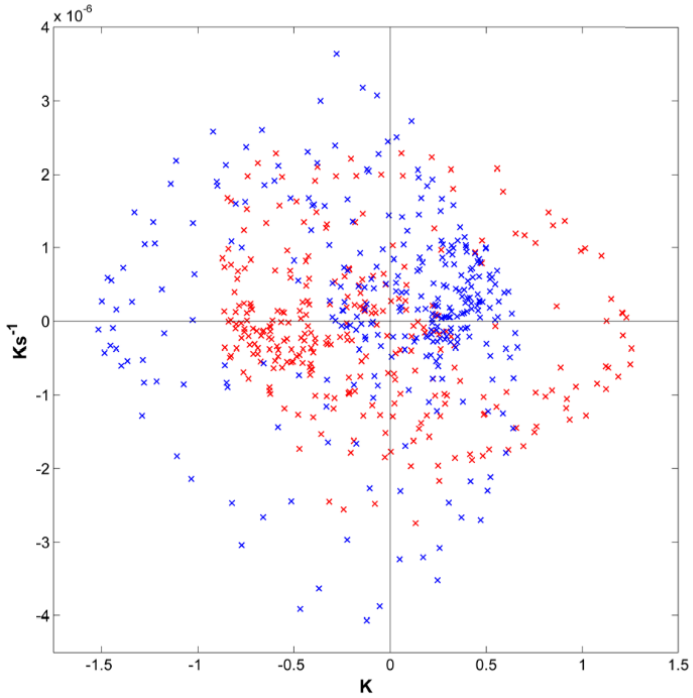


Figure 4.9: Scatter plot of the values of $\langle T' \rangle$ (i.e. Figure 4.6) and $\langle (\mathbf{u}_g \cdot \nabla T)' \rangle$ (i.e. Figure 4.8) at each point in the region 34-37°N and 142-150°E for the positive phase (in red) and the negative phase (in blue).

heat flux advection term over this region is

$$\begin{aligned} \iint \left(\overline{\mathbf{u}_g} \cdot \nabla T' + \mathbf{u}_g' \cdot \overline{\nabla T} \right) dx\, dy &= \iint \nabla \cdot \left(\overline{\mathbf{u}_g} T' + \mathbf{u}_g' \overline{T} \right) dx\, dy \\ &= \oint \left(\overline{\mathbf{u}_g} T' + \mathbf{u}_g' \overline{T} \right) \cdot \hat{\mathbf{n}}\, ds = -\lambda \iint T'\, dx\, dy. \end{aligned} \tag{4.13}$$

Here we have assumed that the geostrophic flow is non-divergent (i.e. $\nabla \cdot \mathbf{u}_g = 0$) and used the divergence theorem to express the heat flux divergence as a contour integral, where s is the distance around the region and $\hat{\mathbf{n}}$ is a unit vector normal to the boundary.

Time series of the contour integral and temperature integral terms were generated and the composite averages for each phase of the first order MCA index are given in Table 4.1. Analysis of anomalous SST damping suggests normal rates of $\lambda \approx 10^{-7} s^{-1}$ (Frankignoul *et al.*, 1998), so an order of magnitude lower than our calculations. This indicates that, whilst a fairly rough estimate, the geostrophic advection term is at least large enough to maintain the observed anomalous temperature field but that some other processes may be acting to

Table 4.1: Average values of the heat flux divergence and the temperature anomaly over the region of maximum temperature response outlined in Figure 4.6 and the associated damping rate for both phases of the MCA index.

Phase	$\langle \nabla \cdot \overline{\mathbf{u}_g} T' + \nabla \cdot \mathbf{u}_g' \overline{T} \rangle$ (in Ks^{-1})	$\langle T' \rangle$ (in K)	$-\lambda$ (in s^{-1})
Positive	-8.0×10^{-6}	0.77	1.04×10^{-5}
Negative	4.62×10^{-6}	-1.04	4.44×10^{-5}

reduce the temperature anomalies, which cannot be explained by thermal damping alone. An obvious candidate for this would be the horizontal diffusion which is in phase with, and acts to damp, the temperature anomaly field.

4.4 Covariability in other western boundary current regions

We have focussed thus far on the Kuroshio region but the MCA was also performed for other western boundary current regions. Figure 4.10 shows the mean geostrophic velocity magnitude and the mean temperature gradient magnitude over the full period of the MCA and Figure 4.11 shows the results of the first mode of the MCA in the Gulf Stream region. The plots of the mean fields indicate that the strongest mean temperature front in the Gulf Stream region is not obviously aligned with the boundary current jet, as in the Kuroshio region. The maximum SST gradient is found roughly along the continental shelf and this reflects a dependance on topography as well as the nature of the boundary current jet.

The MCA response is strongest near to the coastline where there is a strong dipole-like pattern. Comparisons with the mean plots indicate that this is a slight shifting of the front and jet about the mean position is this region. Away from the coast, in the eastern part of the analysis region, the structure in the velocity magnitude variability pattern is a strong positive tongue flanks by negative regions. This is closely mirrored in the SST gradient field and comparison with the mean fields show that the positive tongue in both fields represents a strengthening of both the jet and the front in the positive phase and weakening in the negative phase. The behaviour away from the coast is somewhat similar to that observed in the Kuroshio Extension region. The SCF of the first mode variability in the Gulf Stream is 48%, however because this is not the location of the largest mean SST gradient which is located close to the continental shelf, it is not clear that this represents the dominant variability in the SST gradient field. Snapshots of the Gulf Stream region show there

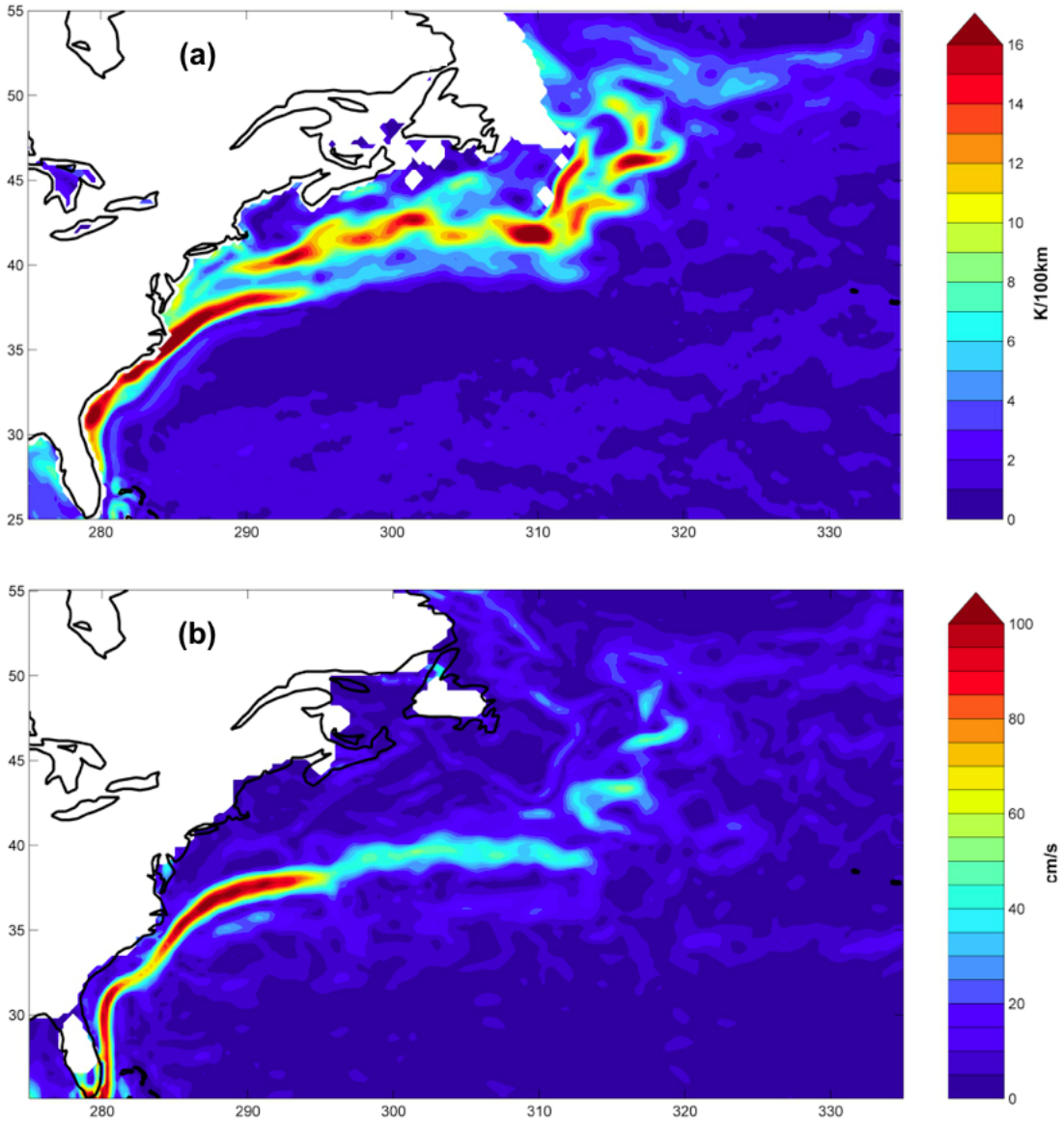


Figure 4.10: (a) The long-term mean SST gradient magnitude, $\overline{|\nabla T|}$, and (b) the long-term mean of the geostrophic velocity magnitude, $|\mathbf{u}_g|$, for the Gulf Stream region over the full MCA period, 2002-2011.

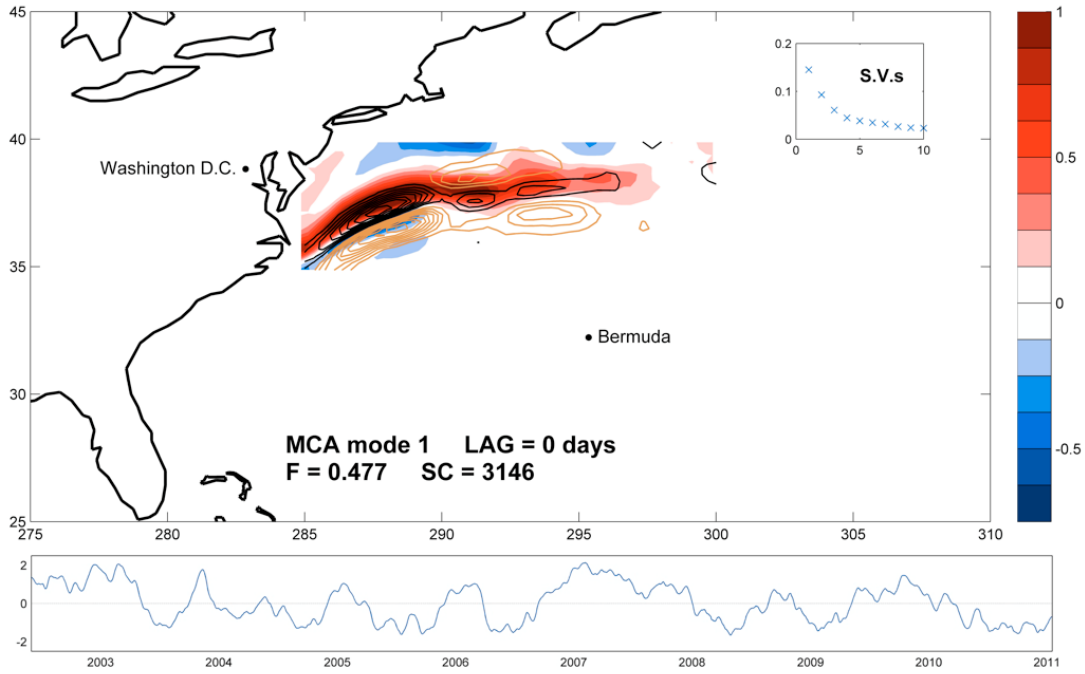


Figure 4.11: As in Figure 4.3 but for the Gulf Stream region. The year labels indicate the beginning of that year.

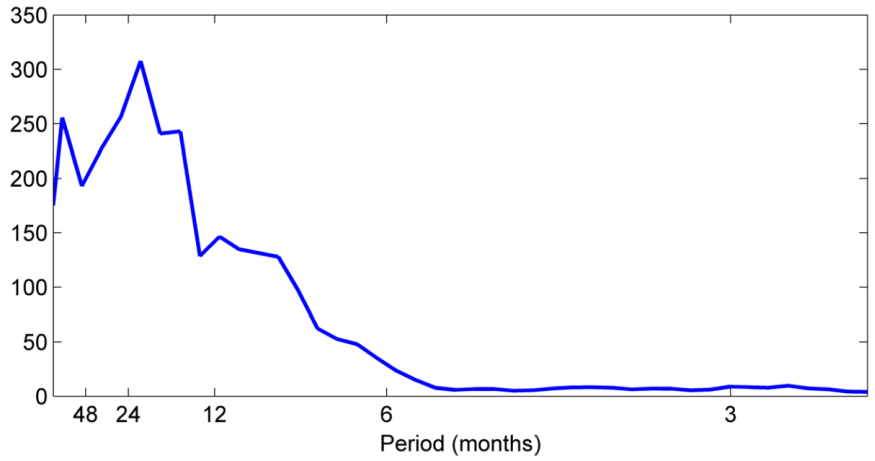


Figure 4.12: Power spectrum of the time series $a_1(t)$ from the Gulf Stream MCA shown in Figure 4.11.

are often two distinct temperature fronts, determined by the shelf and the jet but this is generally rather noisy, unlike the temperature field in the vicinity of the Kuroshio Extension. The time series of the leading order Gulf Stream covariability seems to exhibit a seasonal cycle, with stronger SST gradients present in the winter than in the summer. The power spectrum of the MCA time series, shown in Figure 4.12, indicates some seasonality which may be caused by the relatively shallow shelf water cooling in the winter and generating a stronger SST front than in the summer months.

In an investigation of Gulf Stream fluctuations and associated atmospheric variability, Frankignoul *et al.* (2001) demonstrated that meridional shifts of the Gulf Stream axis are generally preceded by a positive phase of the NAO with a lead time of about 12 months. Their hypothesis is that Rossby waves excited over the central Atlantic propagate westwards and the Gulf Stream adjusts accordingly. To test whether or not the variability of the geostrophic velocity from the Gulf Stream MCA reflects the shifts investigated by Frankignoul *et al.* we produced a lag-correlation plot, shown in Figure 4.13, between the monthly averaged MCA time series and a monthly NAO index[3] (e.g. Hurrell, 1997). The correlation peaks when the NAO leads the MCA time series by 9 months, suggesting that the MCA time series may in part reflect a response of the Gulf Stream to NAO forcing in the same sense as the relationship observed by Frankignoul *et al.* (2001) (i.e. positive NAO

[3]The NAO time series was downloaded from http://www.cgd.ucar.edu/cas/jhurrell/indices.html

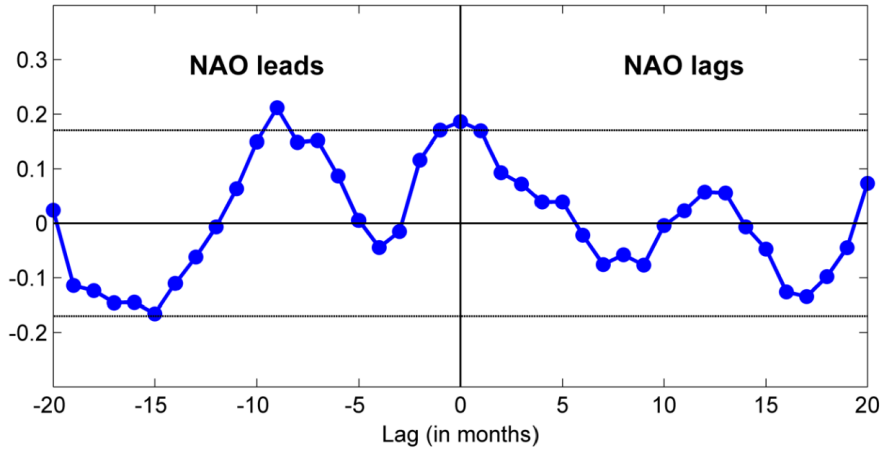


Figure 4.13: Lag correlation between the monthly averaged timeseries $a_1(t)$ from the Gulf Stream MCA and the NAO index, here the dotted line indicates the 5% level for no-correlation and independent samples.

anomaly generally leads a northward shift of the Gulf Stream). However, there is also an additional peak when the NAO lags the MCA index suggesting a clear contamination by the seasonal cycle present in the index.

The MCA for the Agulhas retroflection region, where strong SST gradients are observed (e.g. Figure4.14), is presented in Figure 4.15. The dominant mode of variability in the Agulhas region is much less pronounced than in the Kuroshio and Gulf Stream regions. The velocity and SST fields consist of dominant contributions roughly along the axis of the mean front, however the patterns only explain 14% of the squared covariance and the singular values indicate that this mode is not particularly distinct. These covariability maps largely represent the presence of propagating mesoscale eddies and the first mode has little statistical significance. Plots of the second mode of the MCA reveal similar results so in this region the MCA does a poor job of capturing any low frequency variability that may be present in the frontal region.

4.5 Summary

The aim of this chapter was to investigate the covariability of the western boundary current jets and associated SST front and we have largely focussed on the Kuroshio region. The covariability was investigated by applying the method of maximum covariance analysis

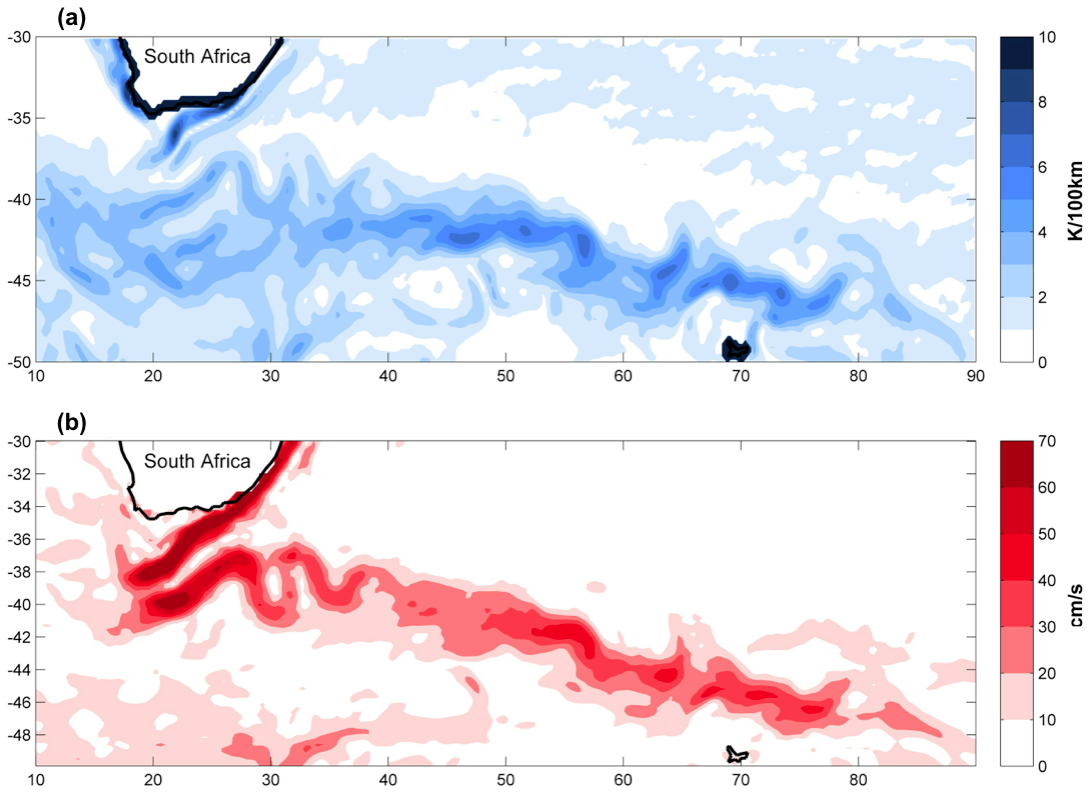


Figure 4.14: (a) The long-term mean SST gradient magnitude, $\overline{|\nabla T|}$, and (b) the long-term mean of the geostrophic velocity magnitude, $|\mathbf{u}_g|$, for the Agulhas region over the full MCA period 2002-2011.

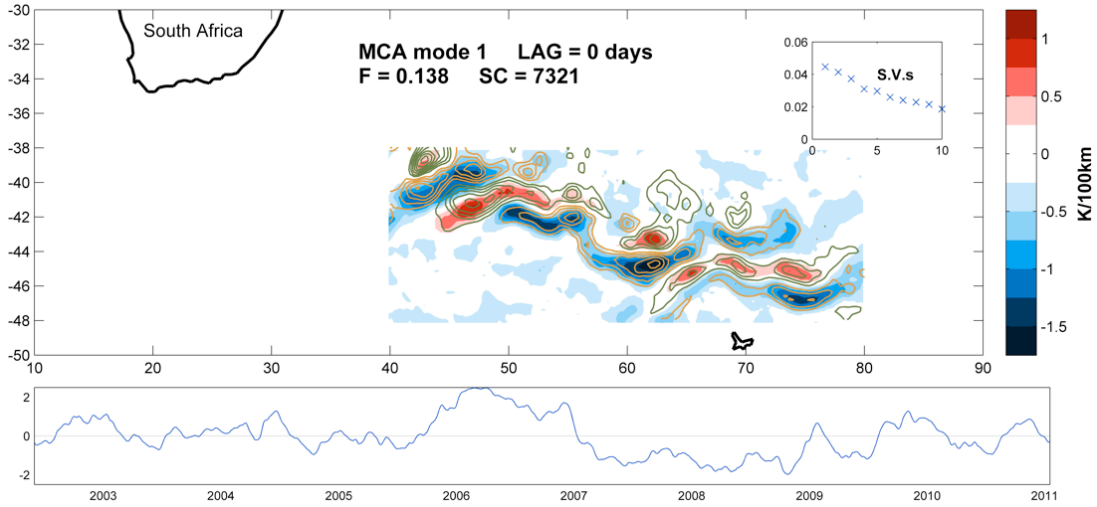


Figure 4.15: As in Figure 4.3 but for the Agulhas region, although here the velocity magnitude contours are every 2.5 cm/s (positive in green, negative in gold and the zero contour is omitted).

(MCA) to the velocity and SST gradient *magnitude* fields. We find that bimodal inter-annual to decadal fluctuations, that have been highlighted in previous studies, dominate the covariability in the Kuroshio region and consists of a strengthening or weakening of the mean features. In the positive phase of our Kuroshio index the velocity field is dominated by a more meandering current and this is associated with a weaker, more diffuse SST gradient. In the negative phase the opposite occurs and the current consists of a sharp narrow jet and the Kuroshio Extension front exhibits a sharp maximum. Composite plots of the temperature anomaly associated with each mode of the variability reveals that the MCA captures a frontal scale variability in the SST and composite maps of the full SST field highlight the sharpening and weakening of the SST front.

The role of the anomalous geostrophic advection in generating the anomalous temperature fields associated with the Kuroshio Extension variability is investigated using a simplified mixed-layer temperature equation. Attempting to match the temperature tendency of the geostrophic advection with the temperature anomaly fields proved to be rather noisy. Analysis of the geostrophic advection term integrated over the region of maximum temperature anomaly, in an attempt to reduce the dependence on spatial derivatives reveals that in this region the heat flux divergence due to geostrophic advection is in the correct sense and at least large enough to produce the observed temperature variations.

Finally, we presented results from the Gulf Stream and Agulhas regions. The Gulf

Stream exhibits a pattern of strengthening and weakening of the mean current and SST front, somewhat similar to the Kuroshio region, but the structure of the temperature front suggest a dependence on the continental shelf as well as the boundary current jet. As a result, the frontal variability that is captured by the MCA cannot be taken as the dominant variability of the SST gradient in this region. The MCA pattern appears to exhibit a weak seasonal cycle, likely due to variations in the SST field, and also exhibits a dependence on the NAO variability, as found in previous studies. In contrast the Agulhas MCA reveals no dominant pattern and the results largely reflects the presence of propagating mesoscale eddies. Due to these various complexities, in the next chapter we investigate the atmospheric response to the Kuroshio Extension variability using the index calculated in this chapter.

Chapter 5

The response of the Pacific storm track and atmospheric circulation to Kuroshio variability

In this chapter we investigate the atmospheric response to the variability in the Kuroshio Extension front (KEF) that was examined in the MCA in the previous chapter. We choose to focus on the Kuroshio region because of the dominant low frequency variability, this was not replicated in the results of the MCA in the Gulf Stream and Agulhas regions which were dominated by a seasonal signal and propagating mesoscale eddies respectively. The hypothesis is that the bimodal variability observed in the strength of the KEF can affect the baroclinicity in the lower-troposphere which could in turn affect the observed Pacific storm track and atmospheric circulation. The analysis in the previous chapter clearly indicates that the anomalous SST pattern associated with the MCA index is a *frontal-scale* SST anomaly (e.g. Figures 4.6 and 4.7) and not a large-scale SST anomaly which has been the focus of previous studies of midlatitude ocean-atmosphere coupling (e.g. Kushnir *et al.*, 2002).

In order to enhance the statistical confidence in the composite analysis that follows, we have extended the time series of the KEF index by projecting the spatial current magnitude pattern (contoured in Figure 4.3) onto the velocity anomaly time series from the previous chapter, over the full length of the SSH time series. The extended time series is from October 1992 to January 2011, which is approximately ten years longer than the optimally

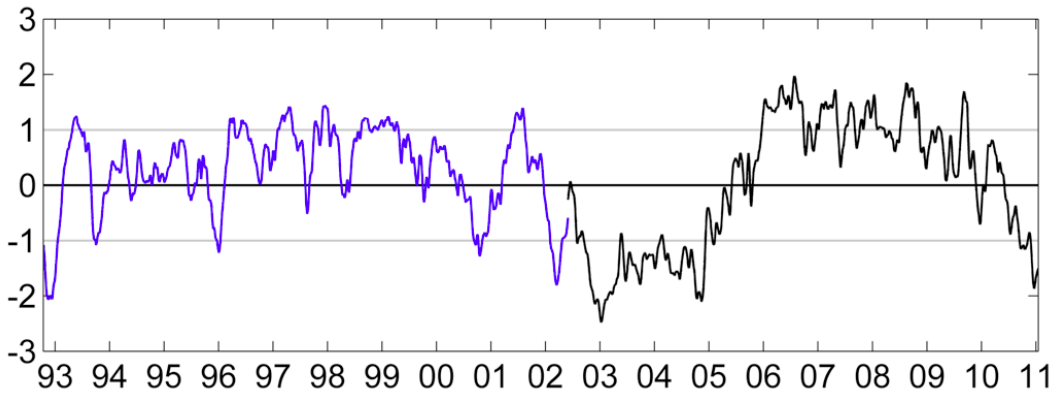


Figure 5.1: Times series of the first mode of the MCA, normalised by one standard deviation, where the original MCA time series is in black and the time series extension (computed by projecting the velocity pattern onto the full time series) is in blue.

interpolated AMSR-AVHRR dataset. The resulting timeseries is shown in Figure 5.1 and is used in the following to composite the atmospheric response.

5.1 Data

To analyse the atmospheric response we use the ERA-Interim reanalysis dataset (Dee *et al.*, 2011; Berrisford *et al.*, 2009) available from the European Centre for Medium Range Weather Forecasts (ECMWF). ERA-Interim covers the period from 1989 to the present day and is supplied on a 0.7° horizontal grid with 60 vertical pressure levels. The dataset is produced by constraining a numerical forecast model with available observational data, including satellite data at well as in situ observations from radiosondes, aircraft and surface stations. A major advantage of a reanalysis using observational assimilation is that the data is available on a consistent grid with full coverage of the globe, however because it is constrained by observations it is less susceptible to model bias.

We use daily values from ERA-Interim of the temperature, T, geopotential, Φ, specific humidity, Q, geopotential height, Z, and sea-level pressure (SLP), P. To measure the storm track response we analyse the eddy heat transport, $\overline{v'h'}$, at the 850mb level where h is the moist static energy, defined as

$$h = C_p T + L_v Q + \Phi, \tag{5.1}$$

where C_p is the specific heat capacity of dry air at constant pressure and L_v is the latent

Table 5.1: Number of days that are used to produce the seasonal and annual phase composites.

Phase	Winter	Spring	Summer	Autumn	Total
Positive	400	404	379	311	1494
Negative	329	202	192	423	1166

heat of vaporisation. The eddy variables are calculated using an 8 day high-pass filter to isolate the synoptic scale baroclinic eddies. We filtered the data using a 31-point Lanczos filter, which is effective at reducing Gibbs effects around the cut-off time scale (Duchon, 1979) and has been used extensively to good effect in the literature. We choose to analyse the eddy transport of moist static energy, as opposed to temperature for example, because of its relevance for the global heat budget (e.g. Czaja and Marshall, 2006). Nonetheless the results presented were generally well reproduced by considering only the temperature field.

5.2 Empirical relations between the Kuroshio Extension front and the atmospheric state

Composites of the eddy heat transport by transient motions on days when the first MCA mode time series is greater (lower) in than (minus) one standard deviation from the mean (indicated by the grey lines in Figure 5.1) were constructed to produce maps for the positive (negative), $\overline{v'h'}_{\text{pos}}$ ($\overline{v'h'}_{\text{neg}}$), phases of the KEF variability. This was performed for each of the three-month seasons separately, along with the annual average for each phase. The number of days that make up the seasonal and annual phase composites are given in Table 5.1. The difference between the composites was also calculated, $\overline{v'h'}_{\text{diff}} = \overline{v'h'}_{\text{pos}} - \overline{v'h'}_{\text{neg}}$, and a statistical significance for the $\overline{v'h'}_{\text{diff}}$ maps was computed using a Monte Carlo method: For each season, 100 random composite pairs were selected from the full data series with the number of constituent days equal to those of the real composites. The difference between each of these composite pairs was then compared with $\overline{v'h'}_{\text{diff}}$ to generate a measure of the significance at each grid point.

The $\overline{v'h'}$ for the northern hemisphere annual average over the whole period of analysis is shown in the upper panel of Figure 5.2. The upper panel of Figure 5.3 shows the annual average of $\overline{v'T'}$ over the analysis period. The pattern of heat transport by the transient eddies is consistent with other studies of the northern hemisphere storm tracks, with a strong

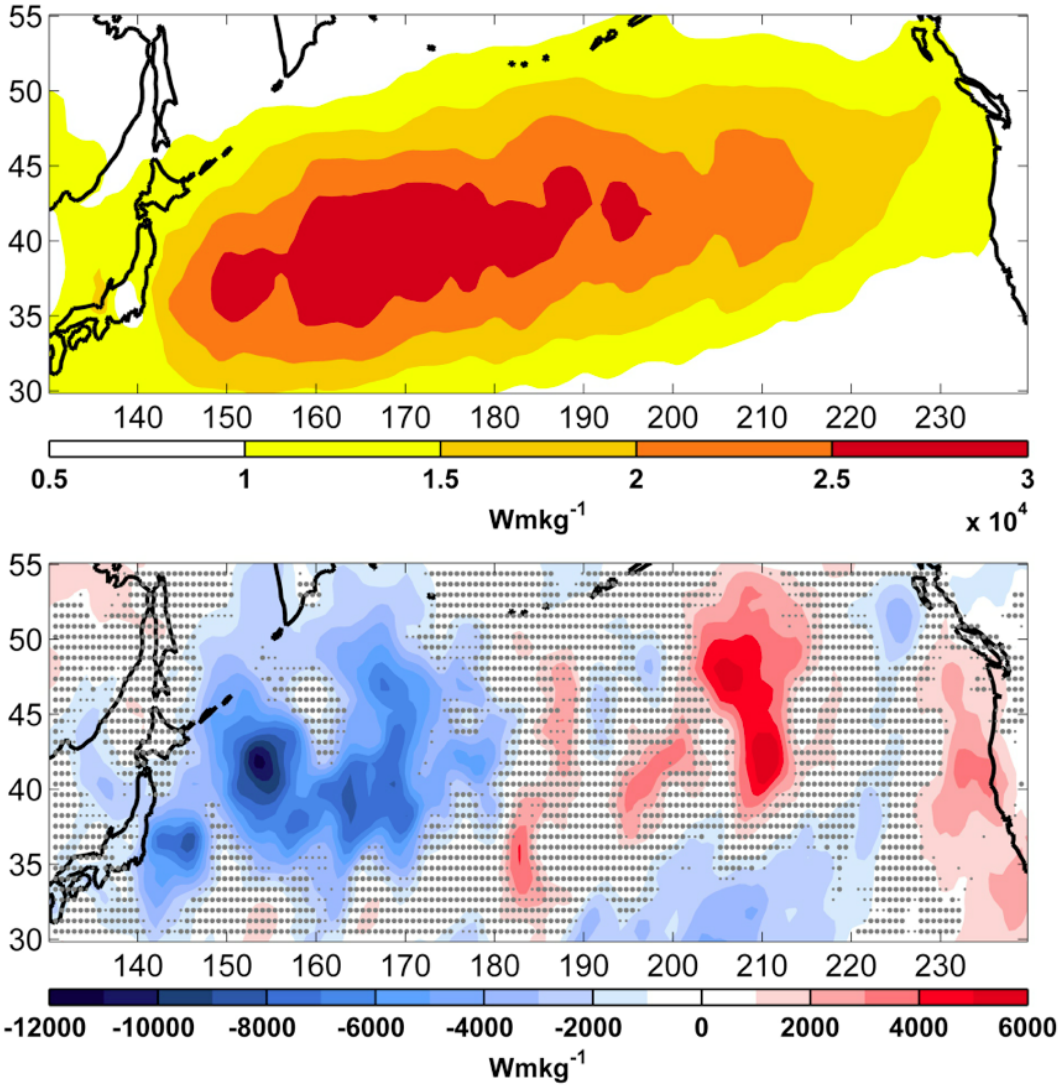


Figure 5.2: (a) The annual average north Pacific storm track, in terms of $\overline{v'h'}$ at 850 hPa, for the length of the KEF time series. (b) The annual average eddy heat transport difference, $\overline{v'h'}_{\text{diff}}$, between the phase composites of the KEF. Regions where the statistical significance of the difference is less than 95% and 90% are indicated by light and heavy stippling respectively.

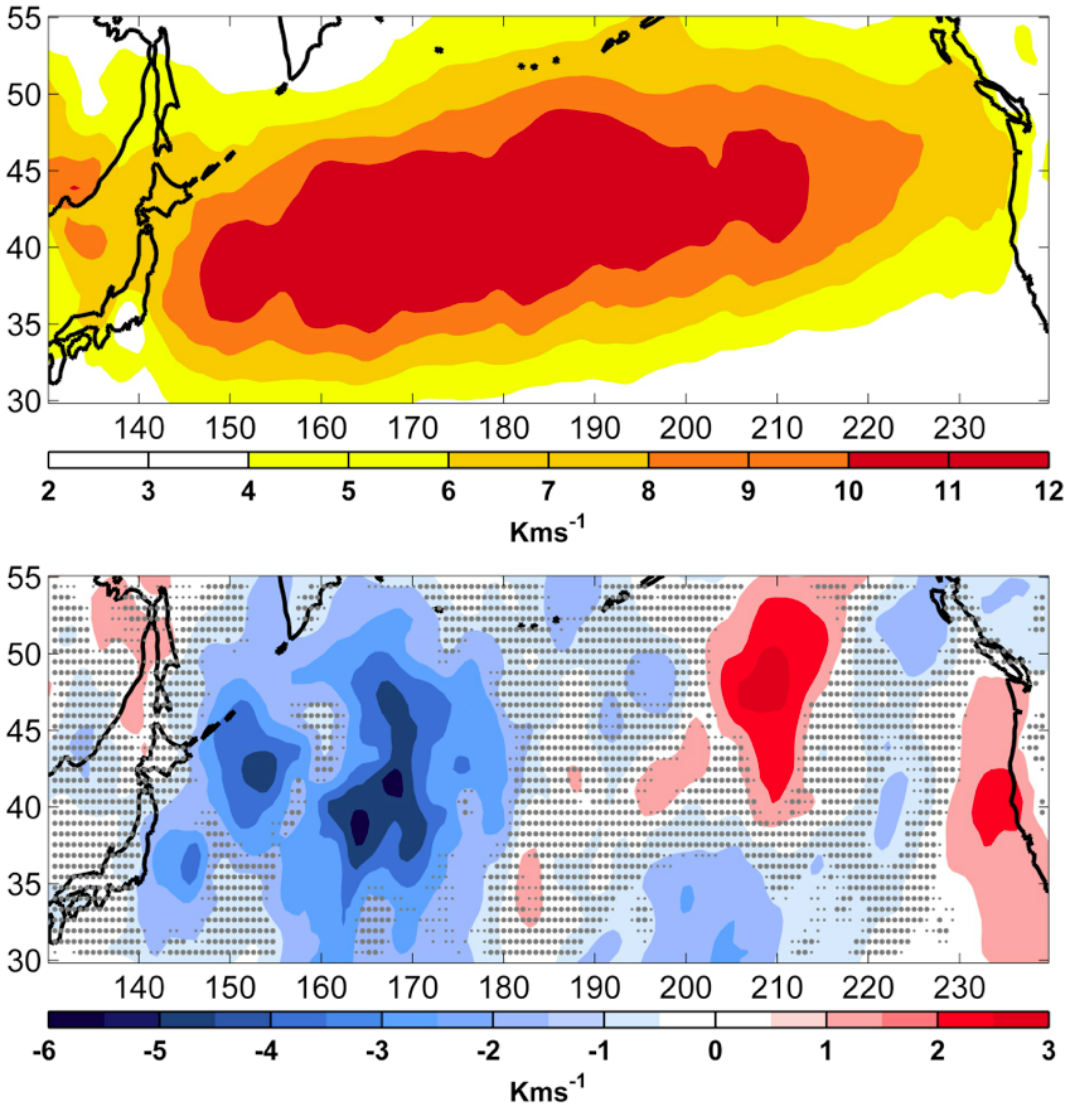


Figure 5.3: As in Figure 5.2 but for $\overline{v'T'}$.

maximum downstream of Japan and a distinct south-west to north-east tilt as the storm track extends eastwards across the Pacific. This represents the lifecycle of a baroclinic wave where growth predominantly occurs over the western Pacific, in the region of peak mean baroclinicity, and the transient eddies develop a significant barotropic component further downstream where the heat transport is reduced (e.g. Simmons and Hoskins, 1978).

The eddy heat transport difference between the two phases, $\overline{v'h'}_{\text{diff}}$, calculated from the annual average composites is shown in the lower panel of Figure 5.2 (for comparison, the equivalent plot for $\overline{v'T'}_{\text{diff}}$ is plotted in the lower panel of Figure 5.3). Here the light stippling indicates regions in which the difference is below 95% statistical significance and heavy stippling indicates regions where the significance is less than 90% from the Monte Carlo analysis. A striking aspect of Figure 5.2 is the large-scale zonal dipole pattern in the eddy heat transport difference, spanning the Pacific. In the positive phase (i.e. when the SSH and SST gradients are weaker over the KE) the eddy heat transport is significantly larger over the entire eastern Pacific, around 40-60° in longitude downstream of the surface baroclinic zone associated with the KEF. In contrast, in the negative phase, when the SSH and SST gradients are largest along the KE, the eddy heat transport peaks further upstream in the western Pacific, in close proximity to the KEF.

Composite maps of the heat transport by transient eddies were also produced for each season separately and the full seasonal $\overline{v'h'}$ plots are shown in Figure 5.4. The maximum in mean eddy heat transport is large and just downstream of the KE in the boreal winter, spring and autumn but in the summer is seen to be much weaker and situated further north of the KE. Figure 5.5 shows $\overline{v'h'}_{\text{pos}}$ for each season and largely resembles the mean seasonal plots except that the region of large transient heat transport appears to extend further downstream in the winter, spring and autumn. Plotted in Figure 5.6 are the composite eddy heat transport in the negative phase of the KEF index, $\overline{v'h'}_{\text{neg}}$. In the winter, spring and autumn the heat transport exhibits a larger maximum value over the western side of Pacific but is reduced further downstream in the eastern Pacific region. The difference between the seasonal composites in Figures 5.5 and 5.6 are plotted in Figure 5.7, where the stippling indicates the statistical significance as before. The zonal dipole pattern in the difference between the annual average composites is strongly reproduced in the winter, spring and to a slightly lesser extent in the autumn. The response in the summer is very weak and there is no particular dipole signal, indicating that the summer does not strongly contribute to the annual average zonal dipole in Figure 5.2.

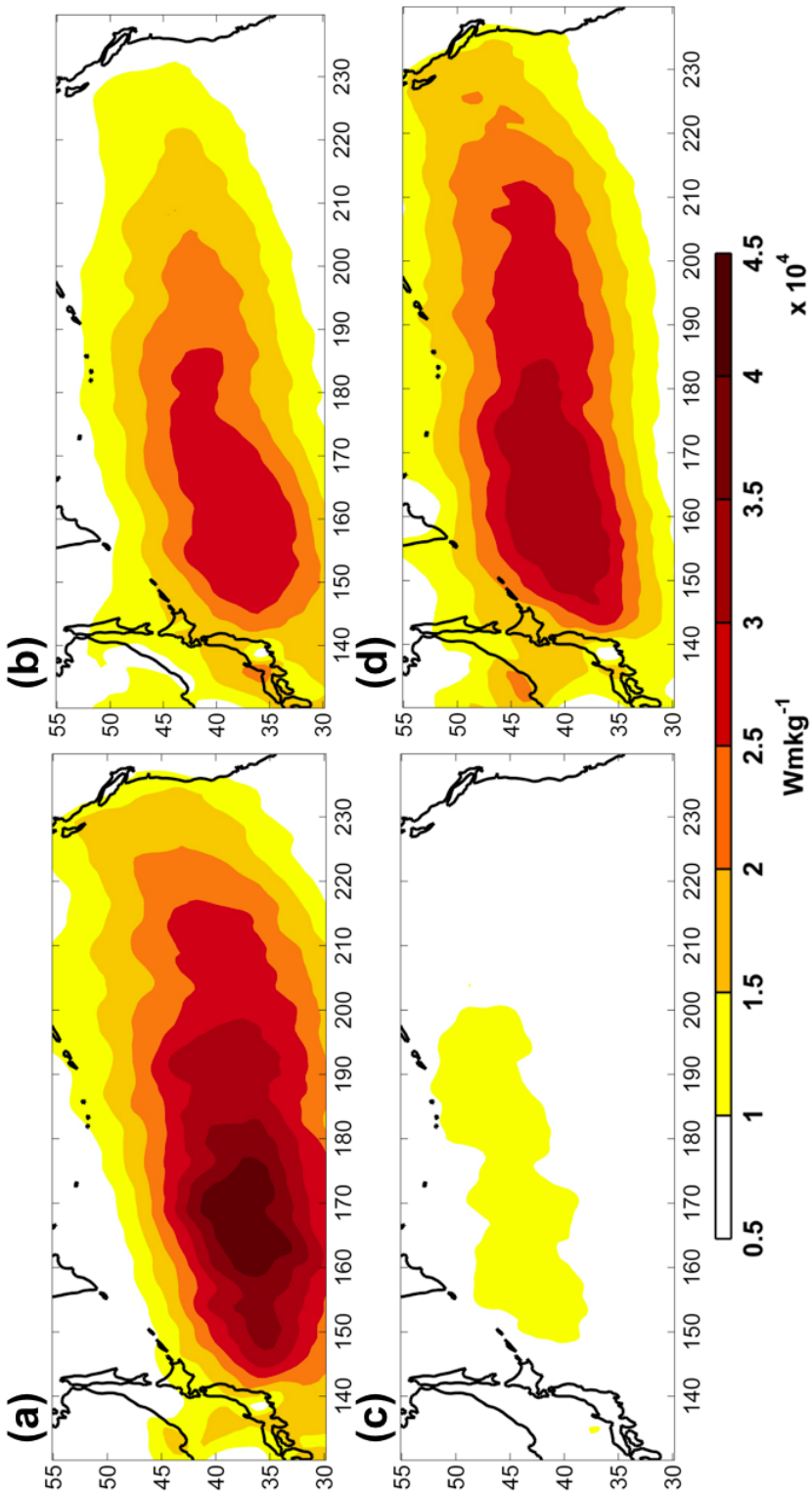


Figure 5.4: The full $\overline{v'h'}$ for (a) the boreal winter (DJF); (b) the boreal spring (MAM); (c) the boreal summer (JJA) and (d) the boreal autumn (SON).

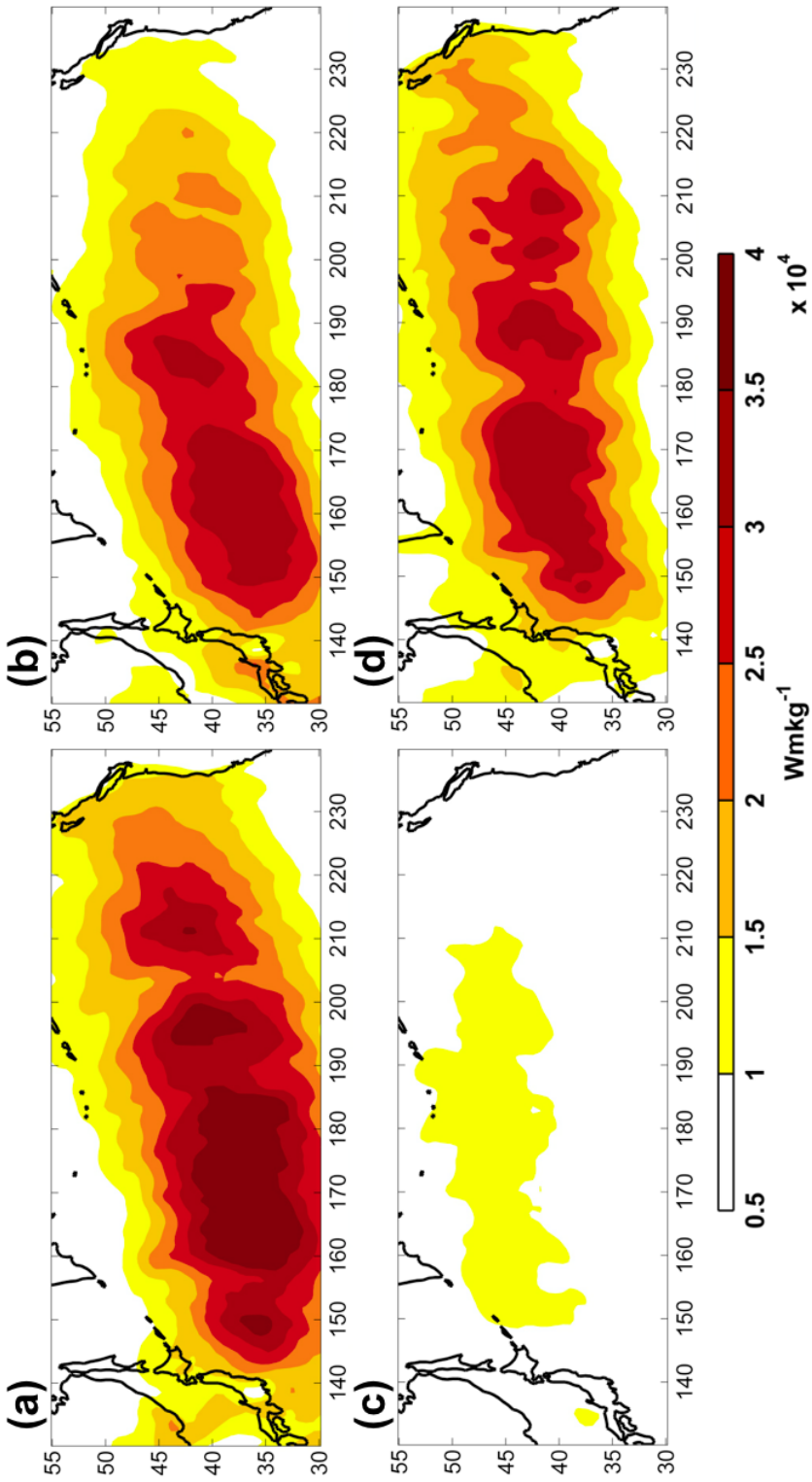


Figure 5.5: The seasonal composite, $\overline{v'h'}_{\mathrm{pos}}$, during the positive phase of the KE index for (a) the boreal winter (DJF); (b) the boreal spring (MAM); (c) the boreal summer (JJA) and (d) the boreal autumn (SON).

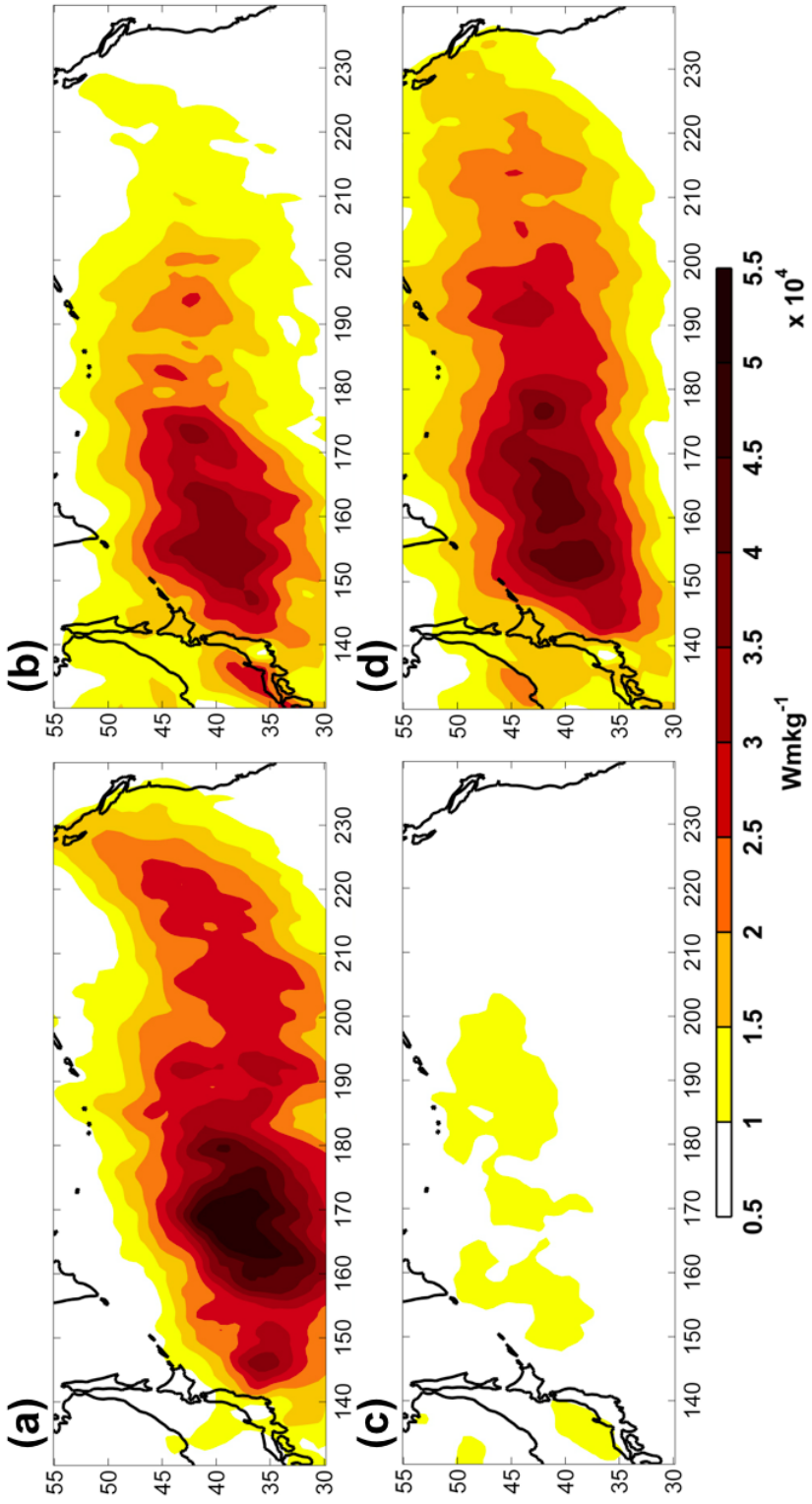


Figure 5.6: As in Figure 5.5 but for $\overline{v'h'}_{\text{neg}}$.

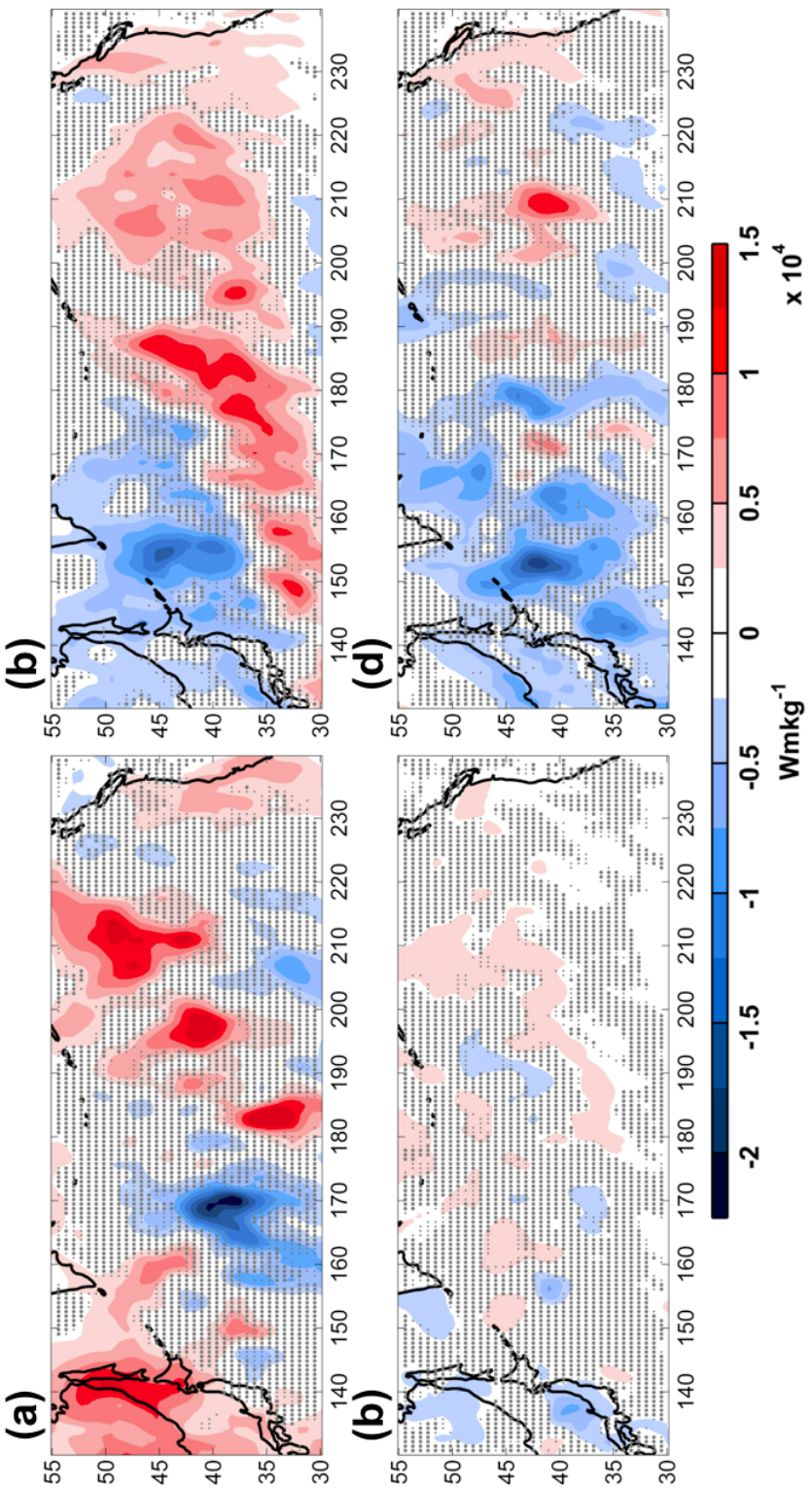


Figure 5.7: The $\overline{v'h'}_{\text{diff}}$ for (a) the boreal winter (DJF); (b) the boreal spring (MAM); (c) the boreal summer (JJA) and (d) the boreal autumn (SON). Regions where the statistical significance of the difference is less than 95% and 90% are indicated by light and heavy stippling respectively.

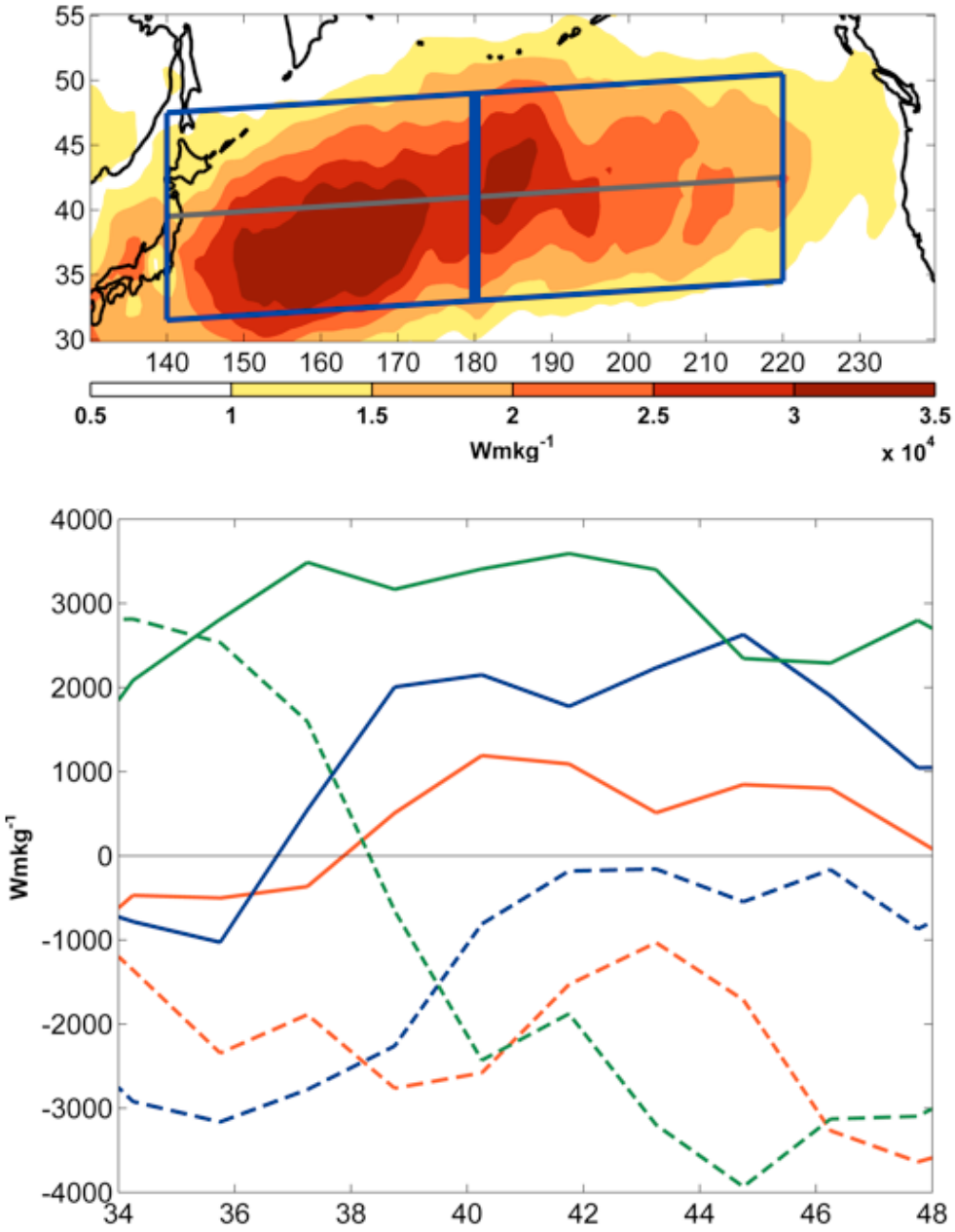


Figure 5.8: Plotted in the lower panel is $\overline{v'h'}_{\text{diff}}$ (where significance is 95% or greater) averaged along the storm track axis (indicated by the grey line in top panel plot, using the $\overline{v'h'}_{\text{pos}}$ from spring as an example) between 140°E and 220°E (the blue outlined region in the top panel) for the boreal spring (in green), boreal winter (in blue) and boreal autumn (in orange). The region is bisected by the thick blue line in the top panel, and averages for the east Pacific region (solid lines) and west Pacific region (dashed lines) are plotted.

In order to be able to make an additional comparison between the composites of $\overline{v'h'}_{\text{diff}}$ across the different seasons (i.e. Figure 5.7) we define a "storm track axis", shown by the thick grey line in the upper panel of Figure 5.8, tilted to approximately follow the mean storm track over the full time series. We averaged along this axis over all points which are at least 95% statistically significant between 140°E and 220°E, as indicated by the region outlined in blue in the upper panel of Figure 5.8. The region is bisected into east and west Pacific storm track regions by the thick blue line in the upper panel of Figure 5.8. This was done for all seasons, with the position of the central cross-section (i.e. the thick blue line in the upper panel of Figure 5.8) remaining fixed, only altering the angle of the storm track axis for each season by visual inspection. The resulting seasonal $\overline{v'h'}_{\text{diff}}$, averaged along the storm track axis for the east and west Pacific, are plotted in the lower panel in Figure 5.8 against the latitude of the central cross-section. The zonal dipole pattern observed in Figures 5.2 and 5.7 is seen to appear in boreal winter, spring and autumn. Note that no similar signal was found during the boreal summer, the summer storm track is much weaker and situated much further north than the KEF and no coherent pattern emerges, as seen in Figure 5.7c.

To measure the variation in the large-scale circulation associated with the KEF state we calculated an annual mean of SLP for both the positive ($\overline{P_{\text{pos}}}$) and negative ($\overline{P_{\text{neg}}}$) phases of the KEF, as well as a climatology of the full data period ($\overline{P_0}$). The annual average for the geopotential height at 500 hPa was also computed for both the positive ($\overline{Z_{\text{pos}}}$) and negative ($\overline{Z_{\text{neg}}}$) phases of the KEF index along with the climatology ($\overline{Z_0}$). The climatologies of both the SLP and geopotential height at 500 hPA over the period of the KEF index are contoured in Figure 5.9 for reference. The annual composites were produced using monthly averages to avoid any particular seasonal bias. Figure 5.10 shows a map of the SLP anomaly, in shading, of the annual average associated with the negative phase of the KEF with respect to the full time series (i.e. $\overline{P_{\text{neg}}} - \overline{P_0}$). On the same map we have superimposed contours of the geopotential height anomaly at 500 hPa associated with the negative phase of the KEF, which was calculated in the same way (i.e. $\overline{Z_{\text{neg}}} - \overline{Z_0}$). The map indicates a strong equivalent barotropic high pressure anomaly over the east Pacific, in the vicinity of Alaska, located to the north of a weaker equivalent barotropic low pressure anomaly. In the western Pacific there is a weaker meridional dipole, with a weaker barotropic component, of opposite sign creating an anomalous quadrupole pattern in the Pacific SLP field during the negative KEF phase. The equivalent plot for the positive phase of the KEF index is shown in Figure

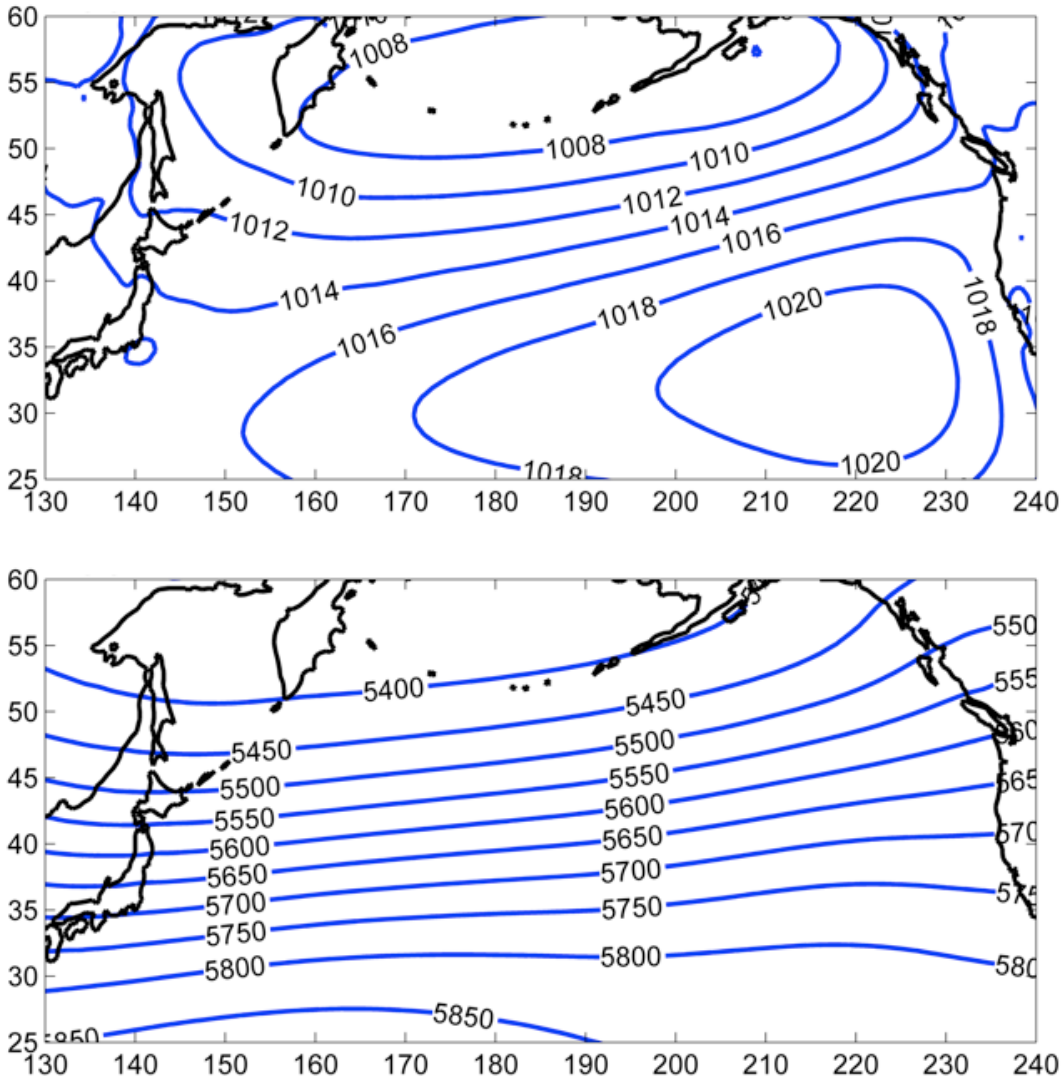


Figure 5.9: Upper panel: Annual average climatology for the mean-sea-level pressure, in hPa, over the period of the KEF index. Lower panel: Annual average climatology for the geopotential height at 500 hPa, in metres, over the period of the KEF index.

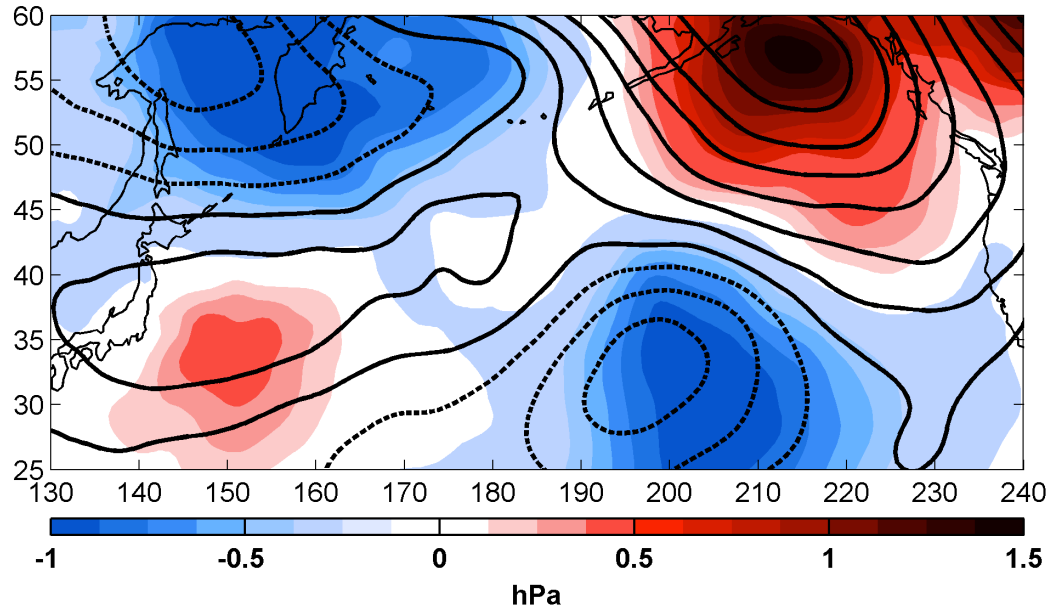


Figure 5.10: Shaded is the annual average SLP anomaly associated with the negative phase of the KEF (i.e. $\overline{P_{\text{neg}}} - \overline{P_0}$). Contoured is the annual average 500 hPa geopotential height anomaly associated with the negative phase of the KEF (i.e. $\overline{Z_{\text{neg}}} - \overline{Z_0}$), from -10 to 26 m with a contour interval of 4 m, where negative values are dashed and positive values are solid.

5.11, where an equivalent dipole structure of opposite sign is observed in the eastern Pacific. In the western Pacific there is no corresponding opposite dipole structure and the signal is weaker.

The seasonal composites of the large-scale circulation were also calculated and are plotted in Figures 5.12 and 5.13. In the positive phase, the eastern Pacific meridional dipole in the annual average map is seen most strongly during the winter but is also present in the spring and autumn. As such, the positive phase exhibits a strengthening of the barotropic westerlies over the eastern Pacific. Over the western region of the Pacific there is no coherent response across the seasons, as might be expected from the annual average plots. In the negative phase, the north-south meridional dipole in the eastern Pacific that is present in the annual average map is a strong feature in the composite maps for the winter and spring but is not apparent in the summer or autumn. The inverse meridional dipole pattern in the western Pacific of the annual negative composite map appears in the autumn and strongly in the spring, to a lesser extent in the summer but not in the winter. The seasonal analysis suggests that the dominant contributions to the annual average composite maps of the

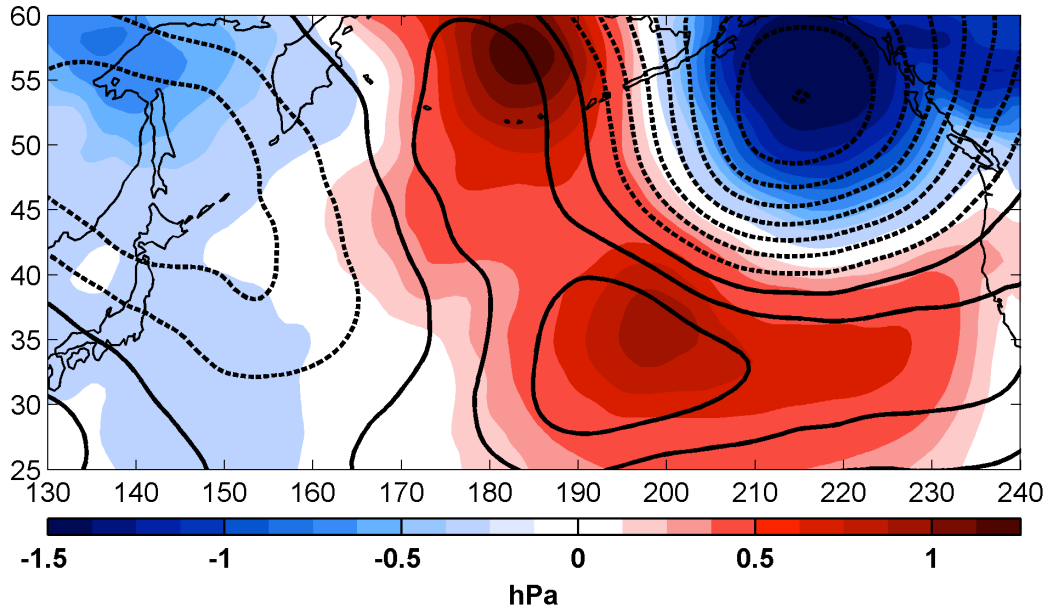


Figure 5.11: As in Figure 5.10 but for the anomaly associated with the positive phase of the KEF. Here the geopotential height contours are from -26 to 10 m with a contour interval of 4 m.

large-scale circulation are occurring during the winter and spring, similar to the seasonal eddy heat transport contributions to the respective annual average.

5.3 Interpretation as evidence of an atmospheric response to ocean variability

The analysis presented above implies correlation between the state of the Kuroshio and the state of the atmosphere but it does not necessarily imply causality. In the midlatitudes, a large part of the oceanic variability is forced by the atmosphere (e.g., Frankignoul, 1985) and it is important to assess whether this could be the case here. Therefore, to be able to discuss the atmospheric response to Kuroshio variability, we must first consider the hypothesis that the observed variability is as a result of the atmosphere forcing the ocean. From the start though, we rule out a thermodynamic forcing (air-sea heat fluxes or anomalous Ekman advection) of the changes in SST gradient displayed in Figure 1c on the basis that the results of the MCA analysis reveal that the strength of the geostrophic velocity is approximately proportional to the strength of the SST front. The change in SST gradient is indeed more

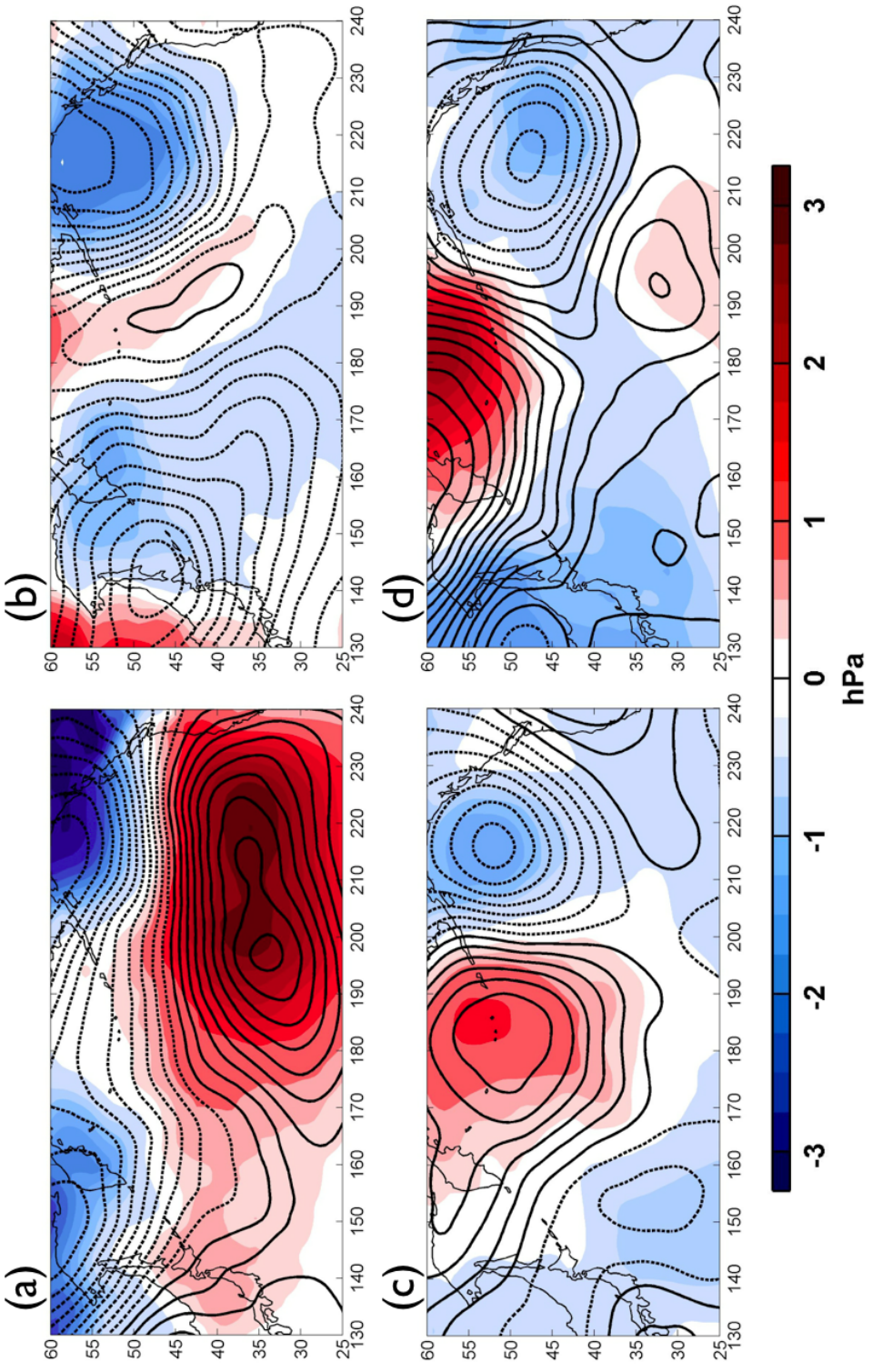


Figure 5.12: The seasonal SLP anomaly (shaded) and 500 hPa geopotential height anomaly associated with the positive phase of the KEF (i.e analogous to Figure 5.11 but for each season) for (a) the boreal winter (DJF); (b) the boreal spring (MAM); (c) the boreal summer (JJA) and (d) the boreal autumn (SON). Negative values are indicated by dashed contours and positive values by negative contours, the contour interval is 4 m (i.e. ..., -10, -6, -2, +2, +6, +10, ...).

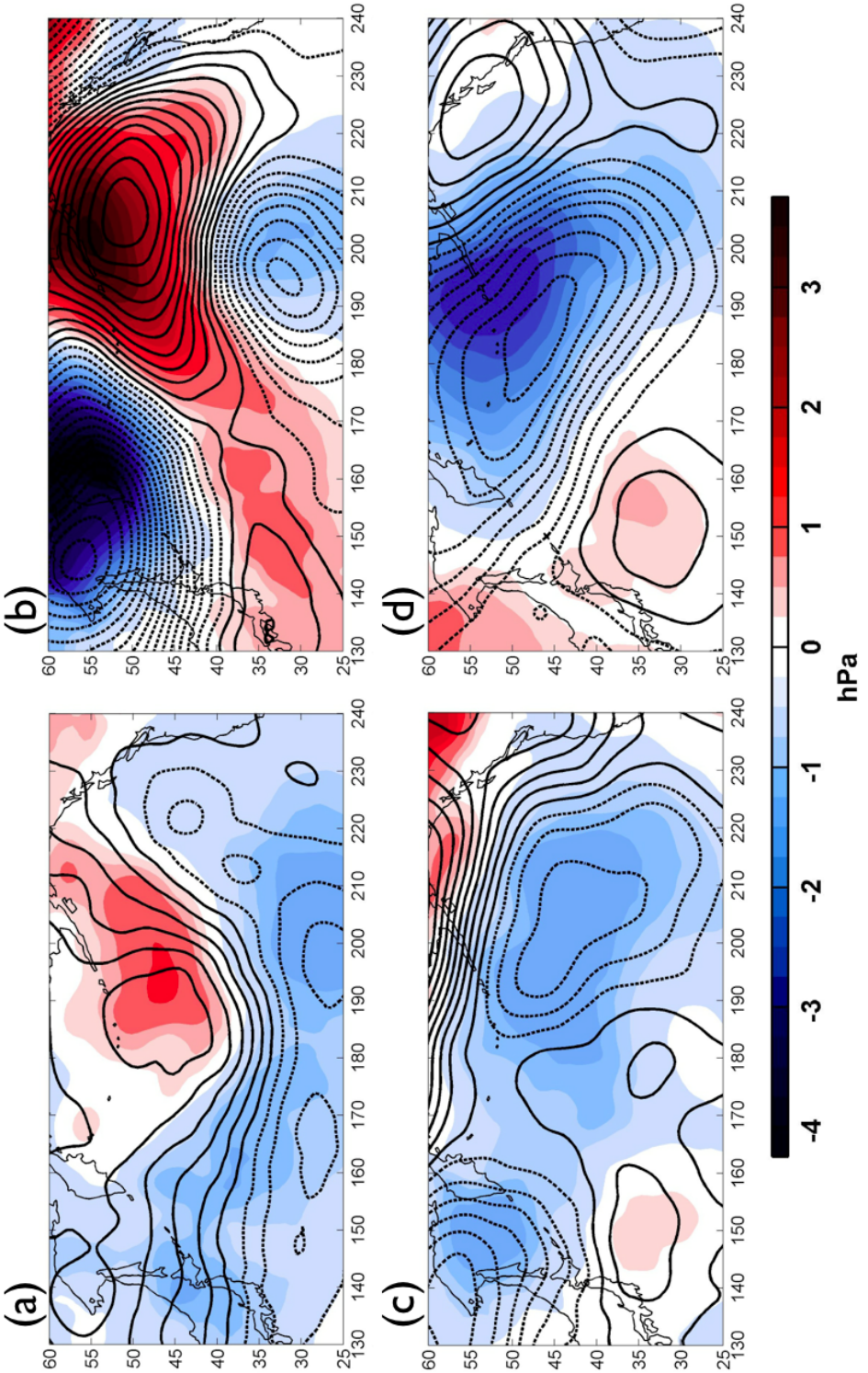


Figure 5.13: As in Figure 5.12 but for the negative phase of the KEF.

readily interpreted as a simple thermal wind response of the upper ocean temperature field to changes in the ocean currents.

We thus must focus on the possibility that the changes in geostrophic currents, captured in determining the KEF index in Figure 5.1, could be a response to changes in surface winds. Deser *et al.* (1999), for example, investigated the mean intensification of the KE flow between the 1970's and the 1980's found it to be consistent with an increase in the wind driven flow across the latitude of the KE. To test the expected response of ocean to the atmospheric forcing we computed the annual average wind-stress, $\overline{\tau}$, (using monthly averages to again avoid seasonal biases) for the positive phase, negative phase and full time series using surface wind-stress data from the ERA-Interim daily dataset. The depth integrated geostrophic streamfunction, Ψ, was calculated from the wind-stress data following the method of Deser *et al.* (1999):

$$\Psi(x) = -\frac{f}{\beta\rho_0}\int_{x_E}^{x} \mathbf{k}\cdot\left(\nabla\times\frac{\overline{\tau}}{f}\right)dx', \tag{5.2}$$

where x is the longitude and x_E is the longitude of the eastern boundary where the streamfunction is assumed to be zero. The streamfunction is evaluated at each latitude separately and the fields for the full time series and the difference between positive and negative phases are plotted in Figure 5.14, along with the wind-stress curl difference (i.e. $\nabla\times\overline{\tau_{\text{diff}}}$).

Comparison between geostrophic streamfunction difference in Figure 5.14c and the full streamfunction in Figure 5.14a reveals that the large-scale oceanic response to the wind forcing associated with the positive phase of the KEF index is an intensification of the circulation in both the subpolar and subtropical gyres, whilst in the negative phase the wind forcing acts to reduce the circulation in both gyres. Since the KE extension flow is increased when the KE is less meandering, in the negative phase of the KEF index, the tendency of the wind field is in the opposite sense to the observed decrease in flow during periods where the KE meanders more. Another feature of Figure 5.14c is that the peak in the streamfunction difference in the subtropical gyre actually occurs towards the centre of the basin and in the region of the KE itself is significantly smaller. This is due to a substantial amount of east-west compensation in the wind-stress curl field shown in Figure 5.14b. This is largely to be expected given the zonal dipole structure of the storm track difference plots in Figure 5.8. These results suggest that the positive and negative phases of the KEF index do not simply reflect the response of the KE to a particular state of

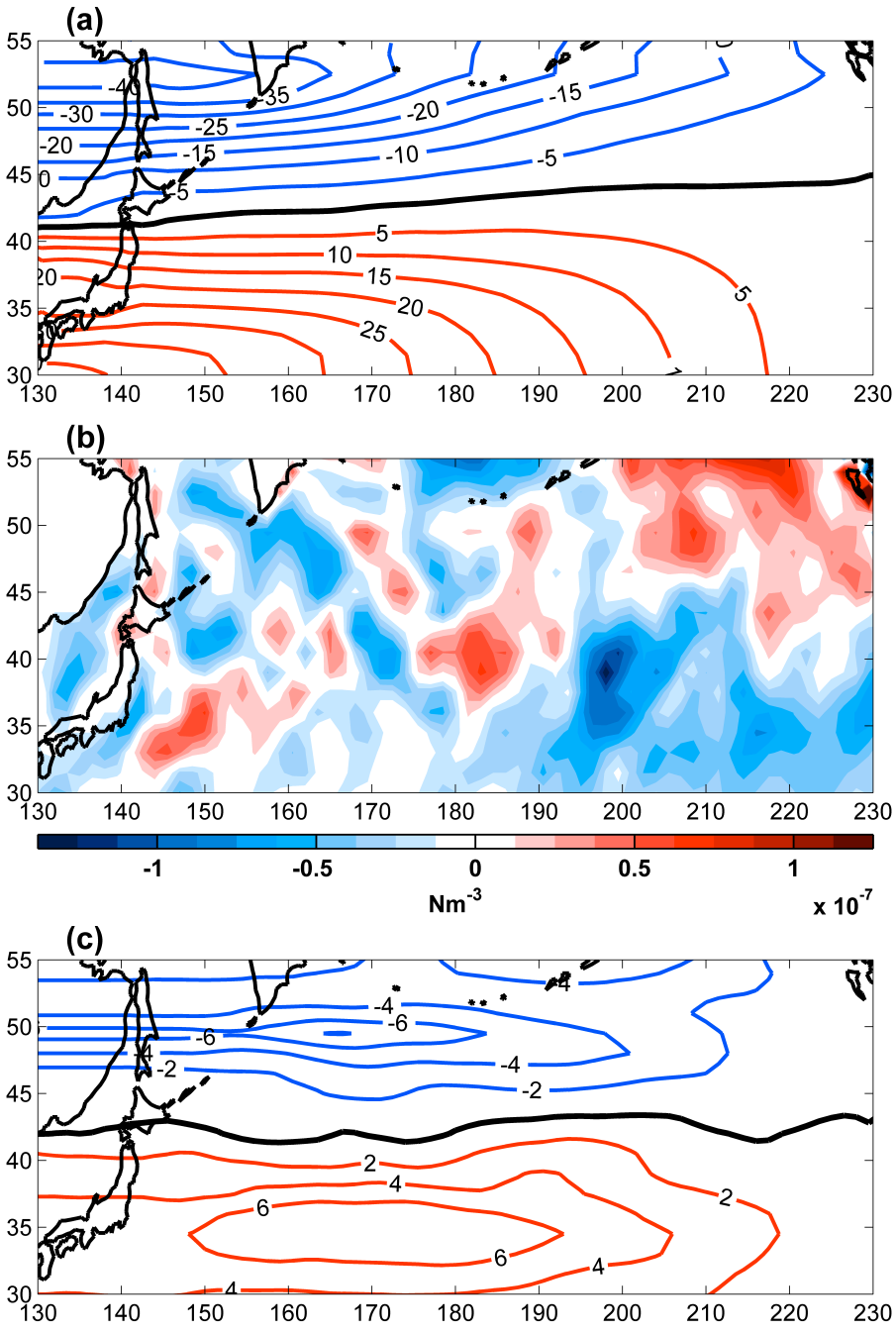


Figure 5.14: The annual averages for: (a) The depth integrated geostrophic streamfunction for the full dataset, $\overline{\Psi_0}$; (b) wind-stress curl difference between the positive and negative phases of the Kuroshio Extension front, $\nabla \times \overline{\tau_{\text{diff}}}$; (c) The difference in depth integrated geostrophic streamfunction between the positive and negative phase, $\overline{\Psi_{\text{diff}}}$, calculated from the wind-stress curl difference in (b). The streamfunction was plotted over the continents but it has obviously no meaning there.

atmospheric forcing.

This conclusion is also supported by observational studies which have suggested that changes in the KE region are partially induced by atmospheric fluctuations following an adjustment period of several years (e.g. Taguchi *et al.*, 2007; Sasaki and Schneider, 2011). Using lagged regression analysis of satellite SSH data, Sasaki *et al.* (2013) demonstrated that the strengthening of the KE jet was driven by large-scale westward propagating SSH signals, originating three-years prior in the eastern Pacific. The positive SSH anomaly is seen to be driven by an anomalous anticyclone spanning the latitudes of the KE region in SLP regression maps, whereas in the negative phase of our KEF index (when the KE jet is strengthened) there is an anomalous cyclone in the eastern Pacific (i.e. Figure 5.11). The opposite sign of these responses in the eastern Pacific opens the possibility of a coupled ocean-atmosphere decadal oscillation. Again, this suggests that our KEF index is not simply an immediate response to the atmospheric forcing but here based purely on observational analysis rather than on the validity of Sverdrup theory.

In addition to extratropical atmospheric forcing, we must also consider the possibility that variability in the tropical Pacific might be driving the atmospheric changes reported above. The values of three El Niño-Southern Oscillation (ENSO) anomaly indices (Trenberth and Stephaniak, 2001), Nino 3, Nino 3.4 and Nino 4[1], are plotted against the monthly averaged values of the KEF index in the scatter plot shown in Figure 5.15. The average values of the Nino 3, Nino 3.4 and Nino 4 indices over the period of the KEF index are -0.04°C, -0.05°C and 0.0°C, respectively. Visual inspection suggests that there is no obvious correlation between any of the indices and our KEF index. The average anomalies of the Nino 3, Nino 3.4 and Nino 4 indices in the positive phase of the KEF are -0.12°C, -0.21°C and -0.27°C, and in the negative phase are -0.01°C, $+0.19$°C and $+0.34$°C, respectively. These values indicate a slight warm El Niño bias in the negative phase and slight cool ENSO bias in the positive phase of the KEF but are modest compared to the standard deviations of the ENSO indices (which are 0.94°C, 0.92°C and 0.74°C, respectively). The impact of ENSO on blocking frequency in the Eastern Pacific was investigated by Renwick and Wallace (1996) who found substantially more blocking in the cool phase. Since we find an enhanced blocking anomaly in the negative phase, which has a slight warm El Niño bias, this suggests no obvious ENSO signal in the above results, consistent with the large scatter

[1]The ENSO indices were downloaded from the Climate Prediction Centre, NOAA (ftp://ftp.cpc.ncep.noaa.gov/wd52dg/data/indices/).

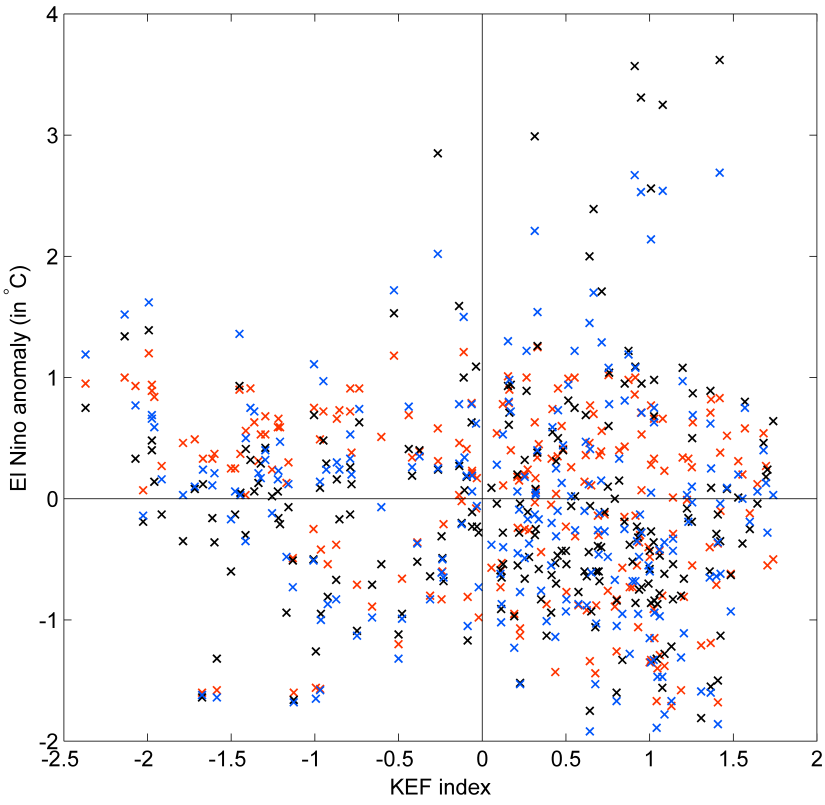


Figure 5.15: A scatter plot of the normalised monthly mean KEF index (i.e. Figure 1b) against the El Niño anomaly for the Nino 3 (in black), Nino 3.4 (in blue) and the Nino 4 (in red) indices, in °C.

in Figure 5.15.

Interpreting the composite maps of the atmospheric state as a response of the atmosphere to the low frequency changes in the strength of the KEF, we will now discuss the associated mechanisms.

5.4 Mechanisms

5.4.1 Zonal dipole in eddy heat transport

Comparisons of $\overline{v'h'}_{\text{diff}}$ for each season, plotted in Figure 5.7 and the lower panel of Figure 5.8, reveal a fairly consistent picture in which the eddy heat transport is enhanced in the western Pacific region during the negative phase of the KEF and is enhanced in the eastern Pacific region during the positive phase. This observed influence of the KEF variability on

the storm track in the overlying atmosphere can largely be interpreted in terms of the low-level baroclinicity and the background westerly flow, the importance of which has previously been indicated in modelling studies (e.g. Brayshaw *et al.*, 2008; Nakamura *et al.*, 2008). In the negative phase of the KEF the sharp SST gradient acts to maintain a large temperature gradient, and hence baroclinicity, at low levels through differential sensible heat flux. This enhances the growth rate of baroclinic eddies and the subsequent restoration of low-level baroclinicity, leading to an increase in the eddy heat transport in the immediate vicinity of the KEF and slightly downstream in the west Pacific region. The key here is that the faster growth of the baroclinic waves means that they become significantly barotropic more quickly and as such cannot be advected very far downstream during their growth phase. As such there is less heat transport by transient baroclinic eddies in the eastern Pacific during the negative phase of the KEF, as seen in Figure 5.2. When the KEF is in a positive phase, however, it has a weaker SST gradient and the atmospheric temperature gradient, and hence the baroclinicity, maintained at lower-levels is reduced. If the growth rate of the baroclinic eddies is slower, the growing eddies are advected further downstream by the background westerly flow during the growth phase of their lifecycle, into the east Pacific, where a increased eddy heat transport is observed.

The zonal dipole seems to be most pronounced in the winter and spring but is still apparent in the autumn. The difference between the response in the autumn and spring is interesting because the nature of the background subtropical flow is similar during these seasons. This indicates that the storm track is less sensitive to the low-level baroclinicity in the autumn than in the spring. The land-sea temperature contrast has been shown to be an important factor in determining the nature of the midlatitude storm tracks (Brayshaw et al., 2009) and this is larger in the autumn than the spring, possibly explaining the relative insensitivity to the strength of the SST front. In the summer, the storm track is much weaker and situated significantly further north than the KEF. As a result, it exhibits no coherent statistically significant response to the KEF variability. Note that whilst the SST front appears to influence the low-level baroclinicity, it is the baroclinicity of the background subtropical jet that is main source of available potential energy upon which the eddies feed, and that ultimately determines the strength of the storm track. The fluctuation of the SST front is interpreted as a perturbation to the mean state, zonally localising the storm track more effectively over the western Pacific when the gradient is strong and having less influence when the SST front is weaker.

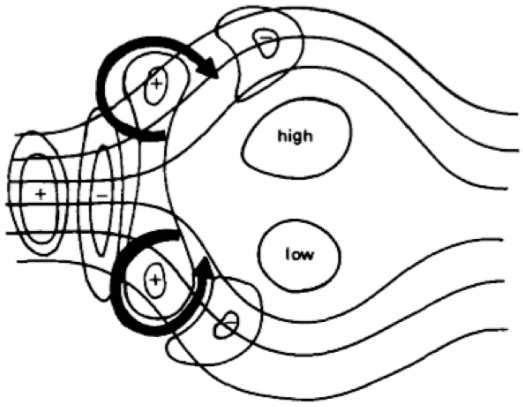


Figure 5.16: Schematic indicating the vorticity tendencies, which act to reinforce the blocking anomaly, in the barotropic eddy-straining mechanism. (From Shutts (1983)).

5.4.2 Blocking effect

The peak in storm track intensity over the western North Pacific during the negative phase of the KEF index is reminiscent of the behaviour preceding the onset of an Alaskan blocking event in the eastern North Pacific observed by Nakamura and Wallace (1990). Using a composite analysis, Nakamura and Wallace analysed an 8-day "envelope function" and observed a distinct increase in baroclinic wave activity upstream of the eastern Pacific blocking pattern in the few days prior to the onset of the latter. The enhanced baroclinic wave activity was found to be generally associated with a large amplitude low pressure system, which when upstream of a subtropical high being advected polewards often generates a cut-off blocking high (e.g. Hoskins *et al.*, 1985). The map of the SLP and 500 hPa geopotential height anomaly found in the negative phase of the KEF, in Figure 5.10, resembles a familiar barotropic blocking pattern with a high pressure anomaly to the north of a low pressure anomaly. This suggests an increased prevalence of blocking flows when the KEF is in the negative phase, whilst the opposite flow pattern in the positive phase is indicative of less blocking. We now show that this hypothesis is consistent with the anomalous zonal dipole observed in $\overline{v'h'}$.

Shutts (1983) outlined a theoretical model for understanding how baroclinic instability can act to reinforce barotropic blocking patterns, as first suggested by Green (1977).

Following the method of Shutts, we use the barotropic vorticity equation on the β-plane:

$$\frac{\partial q}{\partial t} + \mathbf{v} \cdot \nabla q = F_\tau - rq, \tag{5.3}$$

which is the equivalent of the PV equation for the barotropic mode in the two-layer system, (2.23), where here $q = \nabla^2\phi + \beta y$. F_τ is a stirring term (i.e. $\overline{F_\tau} = 0$) representing the generation of the barotropic vorticity by baroclinic instability (i.e. $F_\tau = -(h_1 - h_2)J(\tau, q_\tau)$ in equation (2.23)) and r^{-1} is a damping timescale. By decomposing the terms into their mean and eddy components (denoted by overbars and primes, respectively) the eddy PV equation is

$$\frac{\partial q'}{\partial t} + \overline{\mathbf{v}} \cdot \nabla q' + \mathbf{v}' \cdot \nabla \overline{q} + \mathbf{v}' \cdot \nabla q' = F'_\tau - rq', \tag{5.4}$$

which on multiplying by q' and averaging in time produces the eddy enstrophy equation:

$$\tfrac{1}{2}\overline{\mathbf{v}} \cdot \nabla \overline{q'^2} + \overline{\mathbf{v}'q'} \cdot \nabla \overline{q} = \overline{F'_\tau q'} - \tfrac{1}{2} r \overline{q'^2}, \tag{5.5}$$

where we have assumed that the tendency term and the triple correlation term average to zero for sufficient time-averaging. The first term on the left hand side represents the advection of the mean eddy enstrophy by the mean flow. Marshall and Shutts (1981) showed this is largely cancelled by a rotational (or non-divergent) component of the PV flux, $(\overline{\mathbf{v}'q'})_R$, that is across the mean PV gradient provided the mean potential vorticity is approximately conserved along mean streamlines (i.e., $\overline{q} = \overline{q}\left(\bar{\psi}\right)$):

$$\overline{\mathbf{v}} \cdot \nabla \overline{q'^2} = \left[-\tfrac{1}{2}\mathbf{k} \times \nabla \left(\frac{d\bar{\psi}}{d\bar{q}} \overline{q'^2} \right) \right] \cdot \nabla \overline{q} = (\overline{\mathbf{v}'q'})_R \cdot \nabla \overline{q}. \tag{5.6}$$

Therefore, defining a residual across-gradient PV flux, $(\overline{\mathbf{v}'q'})_* = \overline{\mathbf{v}'q'} - (\overline{\mathbf{v}'q'})_R$, the equation for eddy enstrophy becomes

$$(\overline{\mathbf{v}'q'})_* \cdot \nabla \overline{q} = \overline{F'_\tau q'} - \tfrac{1}{2} r \overline{q'^2}. \tag{5.7}$$

Regions in which the baroclinic forcing term is small and there is net dissipation act as *sinks* of eddy enstrophy and the eddy PV flux is down-gradient:

$$\overline{(\mathbf{v}'q')_*} \cdot \nabla \overline{q} \approx -r\overline{q'^2} \qquad \text{where } \overline{|F'_\tau|} \text{ is small.} \tag{5.8}$$

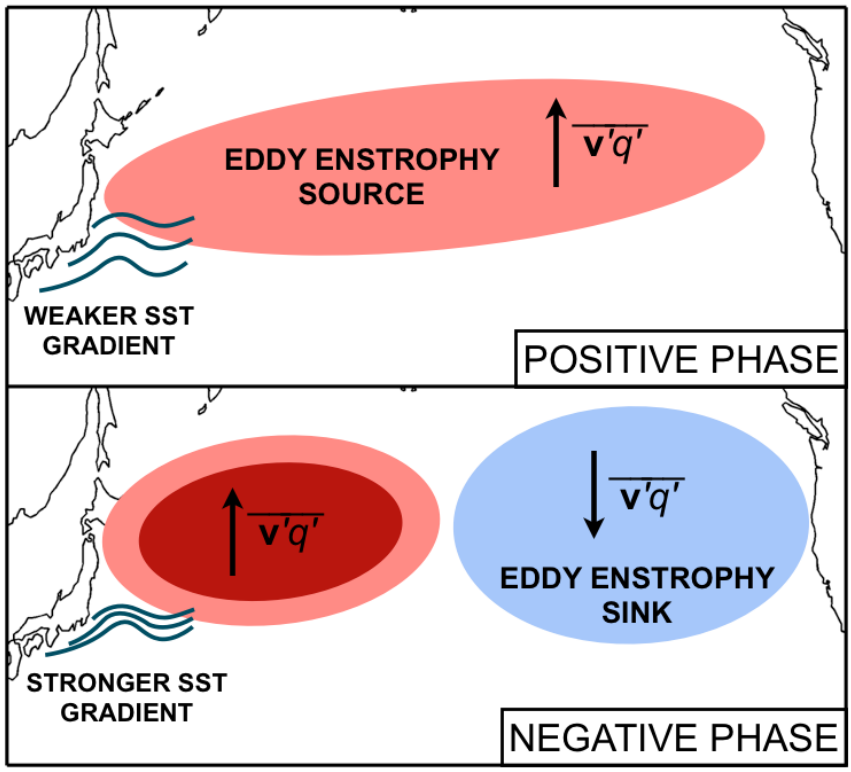


Figure 5.17: Schematic of the barotropic eddy enstrophy sources/sinks and the associated barotropic potential vorticity fluxes in the positive and negative phases of the KEF. In the positive phase, the region of baroclinic growth spans the Pacific and the entire region is a net source of barotropic eddy enstrophy (up-gradient flux of barotropic potential vorticity). In the negative phase, there is enhanced baroclinic growth in the western Pacific and barotropic dissipation in the eastern Pacific. This leads to enhanced down-gradient barotropic potential vorticity fluxes which act to enhance blocking patterns.

In this case the magnitude of the of PV flux down-gradient depends on the amount of eddy enstrophy and in the case of a blocking flow there is an abrupt enstrophy discontinuity due to the straining of barotropic eddies at the upstream edge of the block, as indicated in the schematic shown in Figure 5.16 (reproduced from Shutts, 1983). The down-gradient flux creates a negative eddy PV anomaly to the north and positive PV anomaly to the south which reinforces the PV anomaly of the blocking flow. In contrast, since the forcing term $\overline{F'_\tau q'}$ is positive definite, regions where baroclinic instability is large act as *sources* of eddy enstrophy and the eddy PV flux is up-gradient:

$$\overline{(\mathbf{v}'q')}_* \cdot \nabla\overline{q} \approx \overline{F'_\tau q'} \qquad \text{where } \overline{|F'_\tau|} \text{ is large.} \tag{5.9}$$

Our results can be interpreted in terms of the barotropic model as follows (see also Figure 5.17). In the negative phase, there is enhanced baroclinic growth but this is confined to the western Pacific region and the eddies become highly barotropic by the time they reach the centre of the Pacific (small $\overline{|F'_\tau|}$), consistent with an accelerated lifecycle (e.g. Simmons and Hoskins, 1978). As such, there is increased barotropic dissipation, and hence a sink of barotropic eddy enstrophy in the eastern Pacific. The associated down-gradient barotropic potential vorticity fluxes in turn increase the prevalence of blocking patterns. In the positive phase, the baroclinic growth rate is reduced and the eddies take a longer time to become significantly barotropic. As a result the region of baroclinic growth (large $\overline{|F'_\tau|}$), and hence the source of barotropic eddy enstrophy, spans the Pacific and the entire region is a net source of barotropic eddy enstrophy. The eddy barotropic PV flux is up-gradient, albeit relatively weak, and hence acts to prevent the formation of blocks. From Figures 5.13 and 5.12 it seems that this pattern is best reproduced in the eastern Pacific during the winter and spring and not particularly apparent during the autumn or summer, which is consistent with the stronger zonal dipole found in the winter and spring storm track plots (i.e. Figure 5.7). It is not clear at this stage why there is a disparity between the response in the negative and positive phases between the seasons and it is a point of interest that the winter and spring exhibit a strong response to the index only for the positive and negative phases respectively. Further experiments is necessary to more accurately investigate these different responses.

5.4.3 Eddy-mean flow interaction

The zonal dipole in eddy heat transport and its impact on the large-scale average circulation can alternatively be interpreted in terms of the "**E** vector" of Hoskins *et al.* (1983). The Eliassen-Palm flux was introduced by Andrews and McIntyre (1976) as a diagnostic through which to understand the feedback of eddies onto the zonally averaged flow. The divergence of the zonally-averaged Eliassen-Palm flux vector acts as a forcing term in the zonally averaged momentum equation. Hoskins *et al.* (1983) extended this from the zonally-averaged case to time-averaged three-dimensional quasigeostrophy as a forcing of the x-momentum equation by the divergence of the three dimensional vector **E**. The meridional and vertical components of the **E** vector are the time-averaged equivalent of the Eliassen-Palm flux

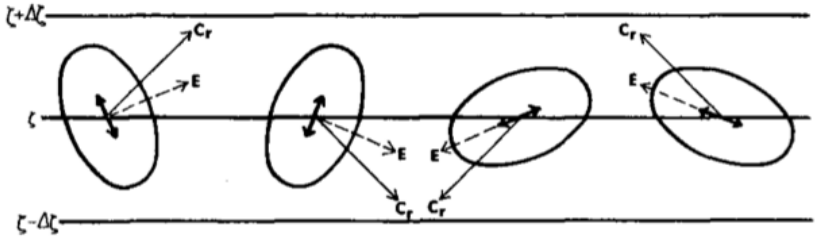


Figure 5.18: An illustration of the eddy anisotropy and the horizontal **E** vector. (From Hoskins *et al.* (1983)).

vector:

$$\mathbf{E} = (E_x, E_y, E_p) = \left(\overline{v'^2 - u'^2}, -\overline{u'v'}, \frac{f}{\frac{\partial \Theta}{\partial p}} \overline{v'\theta'} \right), \tag{5.10}$$

where Θ is a reference potential temperature distribution, here in pressure coordinates.

The application of the **E** vector to the zonal dipole response of the storm track to the Kuroshio variability is immediately clear through the divergence of its vertical component, which is proportional to the eddy heat flux. If we assume that the heat flux is zero at the surface, the acceleration of the westerly flow in the lower part of the troposphere will be approximately proportional to the eddy heat flux at 850 hPa. In the negative phase of the KEF index, the composite eddy heat flux is larger than average over the western part of the Pacific and the westerly flow in the layer between the surface and 850 hPa is accelerated, which is evident in the SLP composite in Figure 5.10 where the meridional SLP gradient is strengthened. The reduced eddy heat transport in the eastern Pacific in the negative phase implies that the eddy-driven flow in the surface layer will be weaker than the climatological mean and this is clearly seen in the reduction in strength of the meridional SLP gradient in this region. Likewise, in the positive phase of the KEF index, the increase in meridional eddy heat transport across the eastern pacific implies a larger divergence of the vertical component of the **E** vector in this region, resulting in an increase in the westerlies near to the surface as seen in Figure 5.11. However, in the positive phase there is no clear acceleration or deceleration of the surface westerlies in the western Pacific region.

The horizontal components of the **E** vector are measures of the eddy anisotropy, where E_x is a measure of the eddy shape and E_y a measure of orientation, as outlined in the schematic shown in Figure 5.18. In a barotropic sense, the **E** vector can be thought of as an equivalent diagnostic through which to determine the implications for blocking fields.

The divergence of the eddy vorticity flux, which describes the eddy forcing the eddies in the mean barotropic vorticity equation, is well approximated in terms of the (horizontal) **E** vector by

$$\nabla \cdot \overline{\mathbf{v}'q'} = \frac{\partial}{\partial y} \nabla \cdot \mathbf{E}. \tag{5.11}$$

The convergence of eastward pointing **E** vectors implies that eddies are being stretched meridionally by a blocking field, which is equivalent to the "eddy-straining" mechanism in Figure 5.16.

Plots of the **E** vector divergence at the 300 hPa level during each phase of the KEF index (during the winter and spring, when the storm-track dipole is strongest, i.e. DJFMAM) is shown in Figure 5.19. Figure 5.19a is the average over the full series. The meridional elongation of barotropic eddies in the entrance and middle of the Pacific storm, due to growing baroclinic waves, is found to generate a divergence of the E vector and an acceleration of the barotropic westerly flow that peaks over the central North Pacific. Whereas in the storm track exit region and on the meridional flanks of the storm track there is convergence of the E vector, indicating a tendency for the eddies to decelerate the westerly flow in these regions.

Figure 5.19b is a composite map of the E vector divergence during the positive phase of the KEF index. The E vector divergence appears slightly larger over the western Pacific region, with a maximum divergence over the eastern region of the storm track. The region of **E** vector divergence extends further into the eastern Pacific region than in the mean. These observations are a reflection of the storm track dipole, and the storm track is stronger over the eastern Pacific during the positive phase of the KEF index, when the SST gradient of the KEF front is weaker. The E vector divergence during the negative phase of the KEF, shown in Figure 7c, is increased over the western Pacific region and instead is reduced over the eastern Pacific region, indicative of decreased barotropic westerlies in this region. The difference between the two phases is shown in Figure 5.19d.

The relation to barotropic blocking was emphasised in a case study of North Atlantic blocking event by Hoskins *et al.* (1983) and in a detailed case study by Shutts (1986), in which the **E** vector of the transient eddies is shown to consistently reinforce the low frequency blocking flow. Therefore, whilst the link of the zonal dipole in eddy heat transport due to Kuroshio variability to the prevalence of blocking is somewhat speculative, the relation to the mean flow is certainly in agreement with the more general **E** vector diagnostic

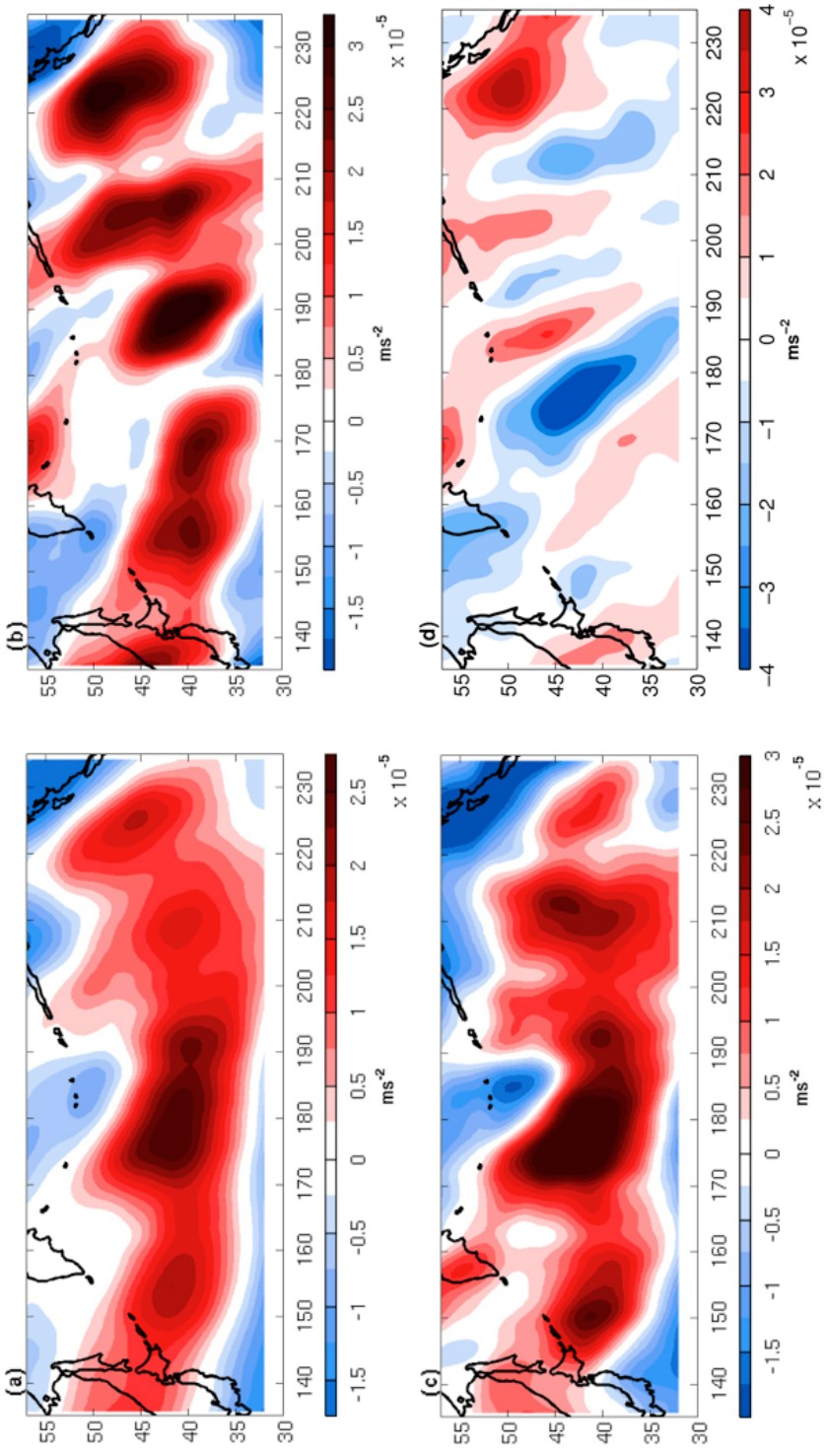


Figure 5.19: a) The **E** vector divergence calculated at 300 hPa over the full boreal winter and spring (the data has been smoothed using a $10° \times 10°$ spatial average calculated at each point as described in the text). (b) As in (a) for the positive phase of the KEF index. (c) As in (a) for the negative phase of the KEF index. (d) The difference between the positive and negative composites.

of eddy-mean flow interaction.

5.4.4 Further effects

Although the storm track response to the KEF variability was primarily described as a zonal dipole, the plot in the lower panel of Figure 5.8 suggests some deviation from this basic structure. The $\overline{v'h'}_{\text{diff}}$ in spring averaged over the west Pacific region is positive at lower latitudes, indicating that there is more eddy heat transport over this region when the KEF is weaker, whereas to the north there is less heat transport which is consistent with the zonal dipole response. The map of $\overline{v'h'}_{\text{diff}}$ for the spring, in Figure 5.7, shows that there is a distinct *meridional* dipole centred at approximately 36°N between 145°E and 160°E, the location of the KEF. Since the mean eddy heat transport is largest at this latitude (as shown in Figure 5.4), this pattern represents a northward shift of the storm track when the KEF is sharper, whilst the western Pacific storm track is located further south when the KEF is weaker. The shift in the observed eddy heat transport is consistent with the idealised aquaplanet studies of Brayshaw *et al.* (2008) (their Figures 5b and 5c) and Nakamura *et al.* (2008) (their Figure 3f), in which the presence of a midlatitude SST gradient was found to generate a poleward shift in the storm track. The sharper SST gradient is more effective at anchoring the storm track further polewards than when it is weaker and the baroclinicity in the lower-troposphere is less important. In this case the storm track is further south in accordance with the maximum in baroclinicity associated with the subtropical jet.

The meridional shift of the storm track about the KEF is not apparent in the autumn, where the storm track is intensified across the whole western Pacific region when the KEF is strong and the zonal dipole pattern dominates. Nor is the meridional shift observed in the winter, where the response to the KEF variability is slightly weaker than in the spring. This might be expected due to the midwinter minimum phenomenon in the Pacific storm track (Nakamura, 1992). Observations suggest that the strong winter subtropical jet often acts to trap anomalies at upper-levels which are then essentially decoupled from the lower-troposheric baroclinic region over the KEF and storm track activity is suppressed (Nakamura and Sampe, 2002). As such, the winter storm track may be somewhat less sensitive to the KEF than in the spring.

5.5 Discussion and summary

In this chapter we have investigated the response of the Pacific storm track to the bimodal variability of the KE. We used the index of the KEF strength calculated in the previous chapter. In the positive phase of the index, the KE is more meandering and the KEF is relatively weak, whereas in the negative phase the KE meanders less and the SST gradient across the KE is strong. This index was used to produce composites of the atmospheric state in its positive and negative phases. We considered the response of the geostrophic ocean circulation to wind changes, previous observational studies of KE response to large-scale atmospheric forcing and also the response of the North Pacific atmospheric circulation to ENSO variability. It was concluded that the composite atmospheric states in the positive and negative phases of the KEF index can be taken as proxies for the response of the North Pacific storm track to weakening/strengthening of the SST gradient along the Kuroshio.

The observed atmospheric response is consistent with the enhancement of low-level baroclinicity across a sharp SST front, confirming what has been previously highlighted in modelling studies. When the Kuroshio is in an unstable state, characterised by more meandering, the SST gradient across the KEF is reduced and eddy heat transport is found to be reduced in the western Pacific region, with more eddy growth occurring downstream in the east Pacific region. However, when the KEF is in its stable phase the eddy growth is enhanced in the western Pacific and weaker eddy growth is observed downstream, the storm track is more zonally localised in this phase of the KE. This reflects the fact that eddies become mostly barotropic in the eastern Pacific when the KE is less meandering, whilst significant baroclinic eddy growth is found to span the entire Pacific when the KE is more unstable. It must be noted that, although we have emphasised SST gradient as being instrumental in controlling the degree of baroclinic instability of the atmosphere, other mechanisms such as convection triggered by large air-sea heat fluxes could also plausibly play a role by lowering the Richardson number over the KE (Sheldon and Czaja, 2013). The role of each of these processes is somewhat unclear but the results presented here show that it is the SST gradient, rather than a large-scale SST anomaly, that is important in determining the zonal dipole in the storm track.

The average response of the large-scale atmospheric circulation to the KEF is suggested to be a barotropic blocking-type pattern in the east Pacific, with enhancement of blocking flows when the KEF is stronger and a reduction of blocking flows when the KEF is weaker.

When considered in terms of the observed zonal dipole response of the transient eddies to the bimodal states of the KE, the impact on prevalence of blocking in the eastern Pacific is in agreement with the barotropic eddy-straining mechanism of Shutts (1983). Specifically, when the growth of eddies in the eastern Pacific is reduced, the dissipation of barotropic eddies dominates and the resulting down-gradient vorticity flux acts to maintain blocking-type patterns. The link between the large-scale circulation patterns to the zonal dipole in eddy heat transport is consistent with the divergence of the vertical component (i.e. the thermal effects of the eddies) of the **E** vector diagnostic of Hoskins *et al.* (1983).

The large-scale flow driven observed in the eastern Pacific suggests that there is the potential for a coupled ocean-atmosphere decadal oscillation over the North Pacific. As previously mentioned, the observational study by Sasaki *et al.* (2013) shows that the broad positive SSH anomalies in the eastern Pacific, driven by an anomalous anticyclonic wind field across the latitudes of the KE region, generate a strengthening of the KE three years later. Similarly, the weakening of the KE is preceded by broad westward propagating negative SSH anomalies in the eastern Pacific three year earlier, generated by an anomalous cyclonic wind field. However, we have shown that when the KE jet is strong, this drives a large-scale *cyclonic* anomaly in the eastern Pacific, which the observational study by Sasaki *et al.* suggests will act to weaken the KE approximately three or so years later. From our study, we expect the weaker KE to drive a large-scale *anticyclonic* anomaly in the eastern Pacific and so on. Coupled decadal modes of variability have been studied in CGCM (e.g. Kwon and Deser, 2007) and in an observationally constrained study using an idealised model by Qiu *et al.* (2007). However, these studies feature coarse SST resolution (e.g. Qiu *et al.* use the 2° resolution Extended Reconstruction SST dataset (Smith and Reynolds, 2004)) , whereas the impact of the Kuroshio Extension on the atmosphere described in this study relies explicitly on frontal-scale SST variability and as a result we can expect that any resultant coupled variability will not be successfully resolved in these previous studies.

The fact that the storm track exhibits a large-scale response to variability in strength of the KEF highlights the importance of WBCs in determining the dynamics of the midlatitude troposphere. In particular, this study suggests that understanding the low frequency variability and potential predictability of the KE could have particular importance in understanding the observed low frequency variability in storm tracks (e.g. Chang and Fu, 2002; Nakamura *et al.*, 2002), decadal variability of blocking flows over the eastern Pacific (e.g. Chen and Yoon, 2002) and associated periods of extreme weather over western North

America (e.g. Knapp *et al.*, 2004). The mechanism highlighted in this study relies primarily on an east-west reorganisation of the storm-track and, as such, it might not be as relevant to the North Atlantic where the ocean basin size is smaller. However, it seems particularly relevant to the Southern Ocean, especially downstream of the Agulhas front, where similar dynamics might influence the prevalence of Australian blocking patterns.

Chapter 6

Summary and future work

6.1 Summary

The results presented in this thesis have mainly focussed on two mechanisms through which oceanic jets can interact with the atmosphere in the midlatitudes. In Chapter 3 we investigated the response of a two-layer quasigeostrophic model to an idealised large-scale stochastic wind forcing, to represent the high frequency forcing of the ocean by the midlatitude storm tracks, which was tuned using observations over the North Atlantic. The stochastic wind forcing excited long baroclinic Rossby waves emanating from the eastern boundary of the basin and these waves are baroclinically unstable. A novel aspect is that the instability leads to a generation of alternating zonal jets but the jets here are wave-like in nature and a direct result of the Rossby wave instability. The jets emerge when averaging the surface flow and their strength decreases with increasing averaging period, which is a characteristic of observed jets in the interior of ocean basins. With only the stochastic forcing component, we find that the jets are fairly insensitive to the strength of the stochastic forcing. In the presence of a mean circulation the jets emerge with less homogeneity. The emerging jets are found to be stronger in the central latitude band and weaker in the north and south, due to the doppler-shift effect of the large-scale mean barotropic flow on the propagation of the baroclinic waves. The mean flow also causes the jets to be tilted slightly by the mean flow, as seen in observations, and largely follow the lower-layer potential vorticity contours in the model. The mechanism of jet generation we have described thereby provides a possible explanation for the recent observations of alternating zonal jets in the midlatitude oceans.

In the second investigation presented in this thesis we assess the impact of a time-varying western boundary current jet, the Kuroshio Extension, on the midlatitude atmospheric storm tracks. In Chapter 4 we used satellite datasets of SSH and SST to assess the covariability of the velocity and SST gradient fields using a maximum covariance analysis. As in previous studies, we found the dominant variability in the jet is a low frequency fluctuation between a strong, narrow current profile in the stable state and a weaker, more meandering current profile in the unstable state. The associated covariability in the SST front is a strengthening and weakening in the stable and unstable states respectively. Analysis of the geostrophic advection term revealed that the anomalous current in each phase of the covariability was easily large enough to generate the observed frontal-scale temperature anomalies. The covariability in both the Gulf Stream and Agulhas regions was found to be more complicated than in the Kuroshio Extension region.

The Kuroshio index developed in Chapter 4 was extended over the full SSH data period and in Chapter 5 we analysed the composite atmospheric response to the positive (i.e. weaker SST front) and negative (i.e. stronger SST front) phases of the index using the ERA-Interim reanalysis dataset. We support our interpretation of the observations as an atmospheric response to Kuroshio variability by considering the geostrophic response of the ocean to the wind-stress in the composite atmospheric states as well as the signal of the El-Niño Southern Oscillation. We showed the anomalous response of the transient eddy heat transport by baroclinic eddies to the strength of the Kuroshio Extension front resembles a zonal dipole structure. When the Kuroshio is more (less) meandering, with a weaker (stronger) SST front, the eddy heat transport is increased in the eastern (western) Pacific region, highlighting the importance of low-level baroclinicity which has previously been investigated in modelling studies. We found the response of the large-scale atmospheric circulation is a barotropic blocking-type pattern in the eastern Pacific. This was interpreted in terms of the storm track dipole and the barotropic "eddy-straining" blocking mechanism, with enhanced (reduced) blocking when the Kuroshio Extension front is stronger (weaker), as well as the extended Eliassen-Palm flux divergence.

As with many studies, the work presented here potentially raises more interesting questions than it does answers. The following section describes specific avenues of further investigation that have been stimulated from the work described in this thesis.

6.2 Future work

6.2.1 Oceanic zonal jets

The mechanism by which zonal jets emerge due to large-scale stochastic atmospheric forcing could clearly be tested more thoroughly using a suite of more complex ocean models, such as MIT GCM (Marshall *et al.*, 1997) and ROMS (Shchepetkin and McWilliams, 2005), in the presence of a more realistic wind forcing profile. However, there is also more scope for idealised studies of this mechanism. As highlighted in the discussion of Chapter 3, the vortcity balance study by Melnichenko *et al.* (2010) using the SSH observational dataset is a useful way to investigate the mechanism generating the zonal jets. It would be informative to reproduce the same vorticity balance using a SSH proxy (i.e. the upper-layer stream function) in further idealised experiments to better characterise the mechanism.

In the idealised studies of Chapter 3, we found the Rossby basin modes to be the dominant variability that emerges in the presence of a large-scale stochastic forcing but did not investigate this further in the mean and stochastic forcing simulations. Therefore, it is not clear from our study the extent to which the emergence of the zonal jets depends on the presence of basin modes in these simulations but it is certainly relevant. It may be that the excitation of basin modes is not important to zonal jet generation in the presence of a mean flow, which itself is a source of available potential energy that the jet growth can feed upon. The basin modes in an idealised two-layer baroclinic ocean in the presence of the barotropic mean flow was investigated by Ben Jelloul and Huck (2005) but the Rossby waves were not subject to baroclinic instability in their study.

6.2.2 Storm track response to other western boundary currents

In Chapter 5 we investigated the response of the Pacific storm track to the variability of the Kuroshio Extension, primarily because in the investigations in Chapter 4 yielded clearer patterns of frontal variability than in other regions. Therefore, it is reasonable to suggest that the nature of the North Atlantic and Southern Hemisphere storm tracks will to some degree be determined by variability of the Gulf Stream and Agulhas return current respectively. In particular, AGCM studies indicate that the zonal asymmetry in the Southern Hemisphere storm track is largely a result of enhanced the low-level baroclinicity associated with the midlatitude SST front (Inatsu and Hoskins, 2004).

Given the difficulties in characterising the frontal variability that were discussed in

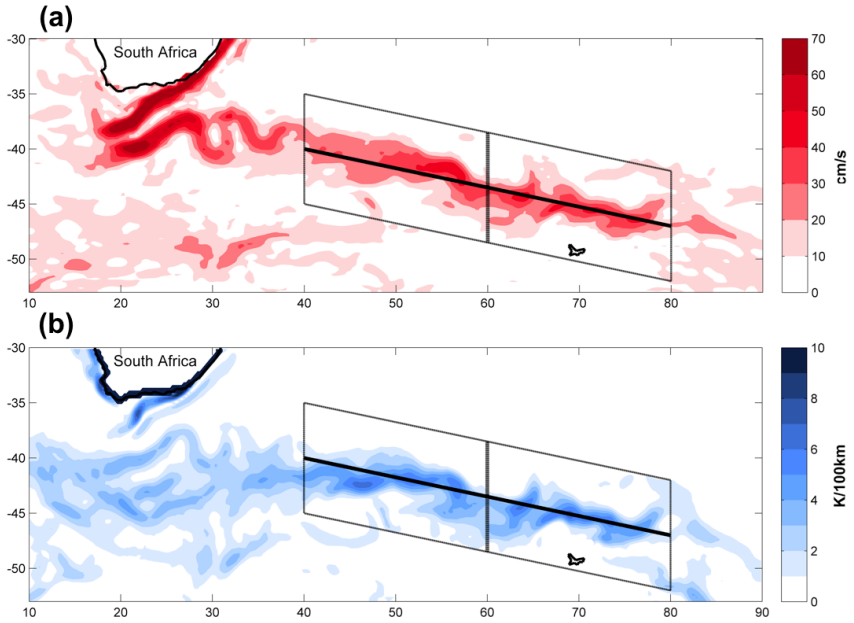


Figure 6.1: Averages of the velocity magnitude and SST gradient magnitude over the period 2002-2011 using the datasets described in Chapter 4. The "along-frontal" axis is marked by the thick black line and the thin grey line marks the area over which the average was taken.

Chapter 4, however, it will be more challenging to assess any potential impact using observations. Though that is not to say that such an approach will be necessarily be fruitless. For example, despite intensely wavy nature of the Agulhas return current and associated SST front, as seen in Figure 4.15, it is possible that it exhibits large scale variations in the SST gradient averaged along the front and preliminary investigations suggest this is the case. Figure 6.1 shows the mean velocity magnitude and mean SST gradient magnitude, as in Figure 4.14, and these maps are superposed with an "along-frontal" axis. Averaging along this axis (in the area marked by the grey lines in Figure 6.1) we obtained an average strength along the front at each day. Following the method in Chapter 4, we carried out an MCA on the frontal average time series and results of the first MCA mode and the SST gradient associated with each phase are shown in Figure 6.2 and Figure 6.3. The dominant variability of the first mode of the MCA therefore represents a sharpening of the SST gradient along the frontal region. Whilst the difference in the SST gradient between the phases is fairly modest ($\approx$1 K/100 km), along the entire length of the frontal region this could be significant and certainly warrants further investigation.

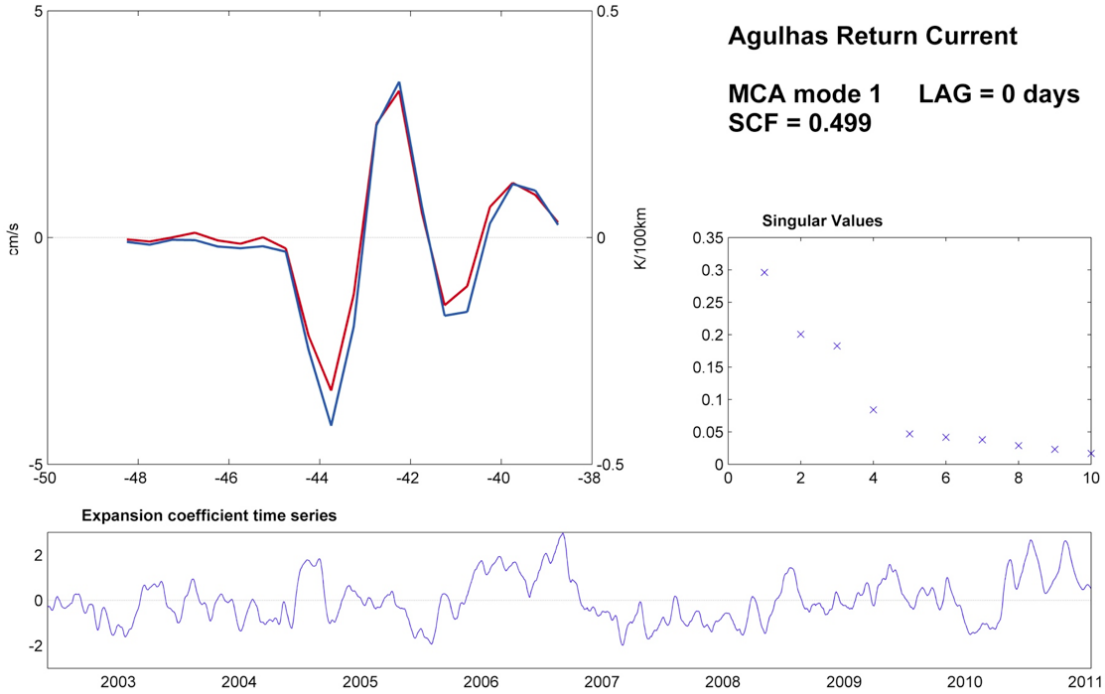


Figure 6.2: Results of the MCA for the "along-frontal" average time series. The variability of the velocity magnitude (in red) and the SST gradient magnitude (in blue) are scaled to be equal to one standard deviation. The singular values, time series and squared covariance fraction (SCF) are also shown.

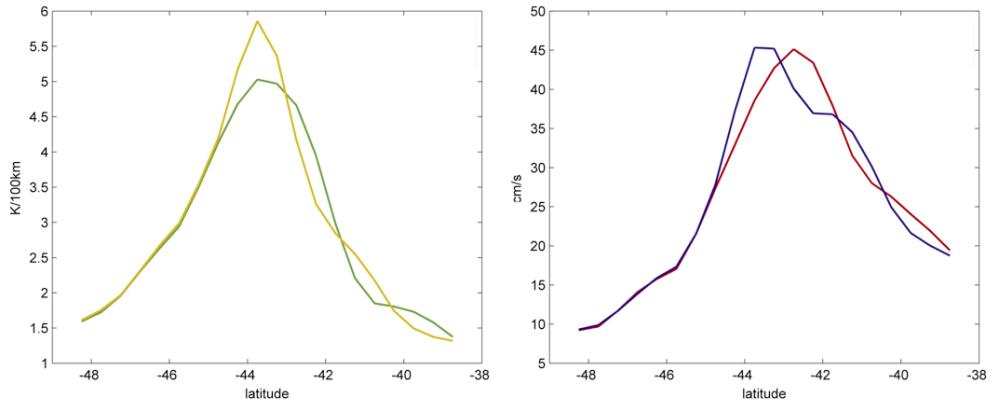


Figure 6.3: "Along-frontal" average for the one standard deviation of the positive phase (in green) and negative phase (in gold) of the first MCA mode(shown in Figure 6.2)

6.2.3 Implications for blocking

An interpretation of the large-scale circulation anomalies due to variability in the Kuroshio Extension was discussed in terms of "eddy-straining" barotropic blocking theory in Chapter 5. However, this remains a working hypothesis and this could be tested using atmospheric reanalysis data or by comparison against common blocking indices. For example, one approach (roughly following the study by Illari and Marshall, 1983) to examine the link of the Kuroshio phase to the eddy vorticity forcing would be to examine the direction of the (high-pass) transient eddy fluxes relative to a "mean" PV gradient (e.g. defined as a 30-day moving average). Our hypothesis suggests that over the eastern Pacific there will be a down gradient eddy flux anomaly in the negative phase, whilst in the positive phase the eddy flux anomaly is expected to be up gradient.

6.2.4 Aquaplanet simulations

The storm track analysis presented in Chapter 5 would also benefit from idealised aquaplanet experiments. These models have been used in the literature to isolate the atmospheric response to prescribed SSTs (e.g. Brayshaw *et al.*, 2008; Sampe *et al.*, 2010). Using an aquaplanet model with a lower boundary SST gradient that is prescribed to the positive and negative SST distributions (i.e. Figure 4.7) would be one way to verify and test the robustness of the zonal dipole storm track response that we describe here. This would also present an opportunity to test the development of blocking fields downstream of the two SST profiles.

6.2.5 Coupled decadal variability in the North Pacific sector

As discussed in Chapter 5, the observation of opposing SLP anomalies in the eastern Pacific in the positive and negative fields suggests that the storm track response to the Kuroshio variability could drive decadal variability in the North Pacific sector. In our study we have shown that frontal-scale variability in the Kuroshio region generates a large scale anomalous circulation in the eastern Pacific. Sasaki *et al.* (2013) demonstrated that large-scale SSH anomalies, generated by large-scale wind circulation, propagate westwards and as the they do so the meridional scale of the signal narrows and intensifies. The most intense response is in the region of the Kuroshio where the signal manifests itself as a strengthening (weakening) of the current for an initial positive (negative) SSH anomaly. The link to our

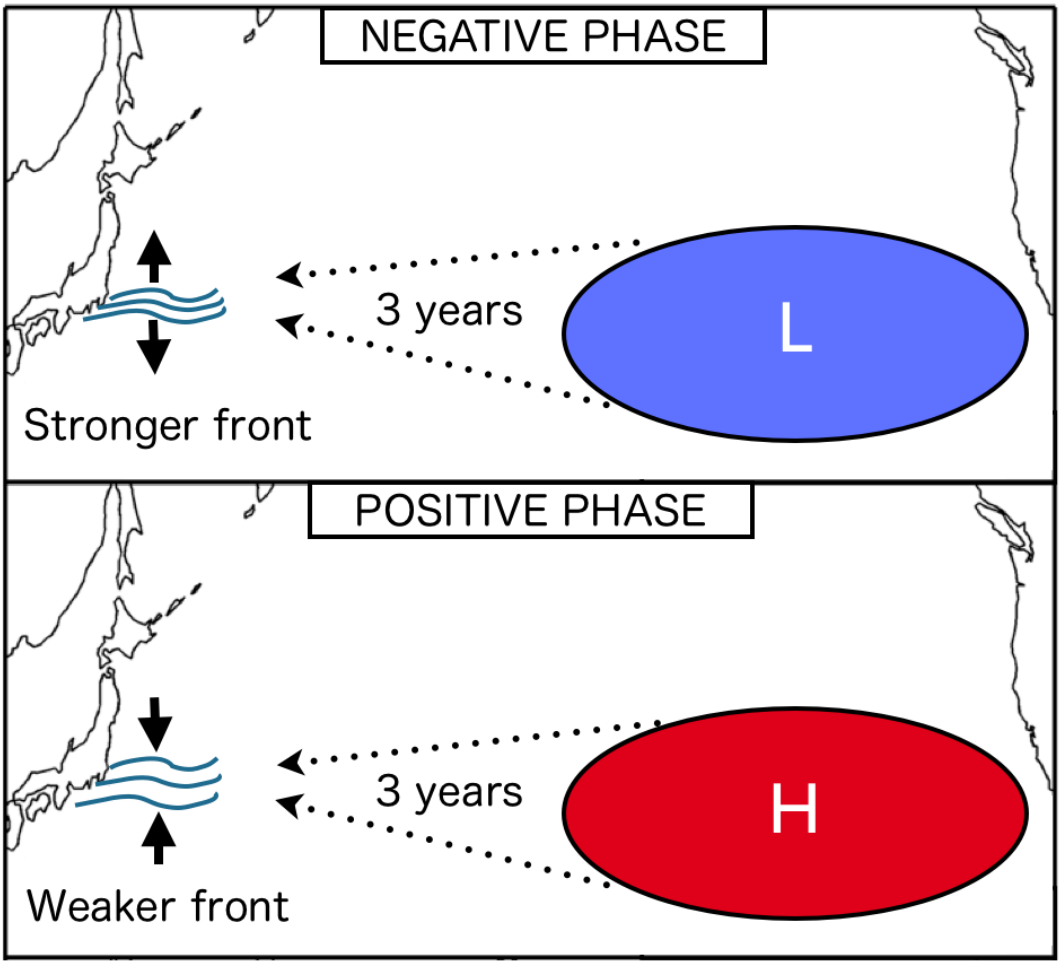


Figure 6.4: Schematic of the coupled ocean-atmosphere decadal variability. The strong SST front (negative phase) drives an anomalous low in the eastern Pacific (as in Figure 5.10). This anomaly then propagates westwards and 3 years later arrives in the Kuroshio region and acts to weaken the Kuroshio Extension and associated SST front. In the positive phase the opposite is true, suggesting the potential for a coupled oscillation.

study is shown by the schematic in Figure 6.4. When there is a strong SST gradient in the Kuroshio region our study indicates that there is an anomalous low in the eastern Pacific, this acts to generate a large-scale SSH anomaly, which from the observations of Sasaki *et al.* is expected to propagate westwards (with a transit time of about 3 years) where it will weaken the jet and SST front. When the SST front is weaker, we expect the opposite and large-scale atmospheric flow will drive a SSH anomaly that will act to strengthen the front some years later.

Given the importance of the strength of the SST front in this mechanism, investigating this coupled feedback is likely to be difficult to assess using observations due to the relatively short period of frontal resolution SST data. The way forward using observations would be to use a proxy for the Kuroshio Extension strength, such as central latitude of the jet (e.g. Qiu and Chen, 2010), which we can use to analyse longer periods of reanalysis datasets. It may also be possible to assess the presence of this feedback in coupled GCM simulations, however due to the importance of the oceanic response this may be difficult in situations where the oceanic component does not capture the frontal-scale variability.

References

Afanasyev, Y., Oleary, S., Rhines, P. & Lindahl, E. (2012), 'On the origin of jets in the ocean', *Geophysical & Astrophysical Fluid Dynamics* **106**(2), 113–137.

Andrews, D. & Mcintyre, M. E. (1976), 'Planetary waves in horizontal and vertical shear: The generalized Eliassen-Palm relation and the mean zonal acceleration', *Journal of the Atmospheric Sciences* **33**(11), 2031–2048.

Arbic, B. K. & Flierl, G. R. (2004), 'Baroclinically unstable geostrophic turbulence in the limits of strong and weak bottom Ekman friction: Application to midocean eddies', *Journal of Physical Oceanography* **34**(10), 2257–2273.

Baldwin, M. P., Rhines, P., Huang, H. & McIntyre, M. (2007), 'Atmospheres: The jet-stream conundrum', *Science* **315**(5811), 467.

Becker, J. M. & Salmon, R. (1997), 'Eddy formation on a continental slope', *Journal of Marine Research* **55**(2), 181–200.

Ben Jelloul, M. & Huck, T. (2005), 'Low-frequency basin modes in a two-layer quasi-geostrophic model in the presence of a mean gyre flow*', *Journal of Physical Oceanography* **35**(11), 2167–2186.

Berloff, P., Kamenkovich, I. & Pedlosky, J. (2009), 'A mechanism of formation of multiple zonal jets in the oceans', *Journal of Fluid Mechanics* **628**(1), 395–425.

Berloff, P., Karabasov, S., Farrar, J. T. & Kamenkovich, I. (2011), 'On latency of multiple zonal jets in the oceans', *Journal of Fluid Mechanics* **686**(1), 534–567.

Berloff, P. S. (2005), 'On rectification of randomly forced flows', *Journal of Marine Research* **63**(3), 497–527.

Berrisford, P., Dee, D., Fielding, K., Fuentes, M., Kallberg, P., Kobayashi, S., Uppala, S. et al. (2009), 'The era-interim archive.', *ERA report series* (1), 1–16.

Boyer, T., Antonov, J., Garcia, H., Johnson, D., Locarnini, R., Mishonov, A., Pitcher, M., Baranova, O., Smolyar, I., Levitus, S. et al. (2006), 'World ocean database 2005', *NOAA Atlas NESDIS* **60**.

Brayshaw, D. J., Hoskins, B. & Blackburn, M. (2008), 'The storm-track response to idealized SST perturbations in an aquaplanet GCM', *Journal of the Atmospheric Sciences* **65**(9), 2842–2860.

Brayshaw, D. J., Hoskins, B. & Blackburn, M. (2009), 'The basic ingredients of the North Atlantic storm track. Part I: Land-sea contrast and orography', *Journal of the Atmospheric Sciences* **66**(9), 2539–2558.

Bretherton, C. S., Smith, C. & Wallace, J. M. (1992), 'An intercomparison of methods for finding coupled patterns in climate data', *Journal of climate* **5**(6), 541–560.

Bretherton, F. P. & Haidvogel, D. B. (1976), 'Two-dimensional turbulence above topography', *Journal of Fluid Mechanics* **78**(1), 129–154.

Centurioni, L., Ohlmann, J. & Niiler, P. (2008), 'Permanent meanders in the California current system', *Journal of Physical Oceanography* **38**(8), 1690–1710.

Cessi, P. & Louazel, S. (2001), 'Decadal oceanic response to stochastic wind forcing', *Journal of Physical Oceanography* **31**(10), 3020–3029.

Cessi, P. & Primeau, F. (2001), 'Dissipative selection of low-frequency modes in a reduced-gravity basin', *Journal of Physical Oceanography* **31**(1), 127–137.

Chang, E. K. & Fu, Y. (2002), 'Interdecadal variations in Northern Hemisphere winter storm track intensity', *Journal of Climate* **15**(6), 642–658.

Chang, E. K., Lee, S. & Swanson, K. L. (2002), 'Storm track dynamics', *Journal of Climate* **15**(16), 2163–2183.

Charney, J. G. (1947), 'The dynamics of long waves in a baroclinic westerly current', *Journal of Meteorology* **4**(5), 135–161.

Chekhlov, A., Orszag, S. A., Sukoriansky, S., Galperin, B. & Staroselsky, I. (1996), 'The effect of small-scale forcing on large-scale structures in two-dimensional flows', *Physica D: Nonlinear Phenomena* **98**(2), 321–334.

Chelton, D. B., DeSzoeke, R. A., Schlax, M. G., El Naggar, K. & Siwertz, N. (1998), 'Geographical variability of the first baroclinic rossby radius of deformation', *Journal of Physical Oceanography* **28**(3), 433–460.

Chelton, D. B., Schlax, M. G. & Samelson, R. M. (2011), 'Global observations of nonlinear mesoscale eddies', *Progress in Oceanography* **91**(2), 167–216.

Chelton, D. B. & Wentz, F. J. (2005), 'Global microwave satellite observations of sea surface temperature for numerical weather prediction and climate research'.

Chen, G., Plumb, R. A. & Lu, J. (2010), 'Sensitivities of zonal mean atmospheric circulation to SST warming in an aqua-planet model', *Geophysical Research Letters* **37**(12).

Chen, S. (2008), 'The Kuroshio Extension front from satellite sea surface temperature measurements', *Journal of Oceanography* **64**(6), 891–897.

Chen, T.-C. & Yoon, J.-h. (2002), 'Interdecadal variation of the North Pacific wintertime blocking', *Monthly Weather Review* **130**(12), 3136–3143.

Cummins, P. F. (1992), 'Inertial gyres in decaying and forced geostrophic turbulence', *Journal of Marine Research* **50**(4), 545–566.

Czaja, A. & Marshall, J. (2006), 'The partitioning of poleward heat transport between the atmosphere and ocean', *Journal of the Atmospheric Sciences* **63**(5), 1498–1511.

Dee, D., Uppala, S., Simmons, A., Berrisford, P., Poli, P., Kobayashi, S., Andrae, U., Balmaseda, M., Balsamo, G., Bauer, P. et al. (2011), 'The ERA-Interim reanalysis: Configuration and performance of the data assimilation system', *Quarterly Journal of the Royal Meteorological Society* **137**(656), 553–597.

Deser, C., Alexander, M. A. & Timlin, M. S. (1999), 'Evidence for a wind-driven intensification of the Kuroshio Current Extension from the 1970s to the 1980s', *Journal of Climate* **12**(6), 1697–1706.

Dritschel, D. & McIntyre, M. (2008), 'Multiple jets as PV staircases: the Phillips effect and the resilience of eddy-transport barriers', *Journal of the Atmospheric Sciences* **65**(3), 855–874.

Ducet, N., Le Traon, P.-Y. & Reverdin, G. (2000), 'Global high-resolution mapping of ocean circulation from TOPEX/Poseidon and ERS-1 and-2', *Journal of Geophysical Research: Oceans (1978–2012)* **105**(C8), 19477–19498.

Duchon, C. E. (1979), 'Lanczos filtering in one and two dimensions', *Journal of Applied Meteorology* **18**(8), 1016–1022.

Eady, E. (1949), 'Long waves and cyclone waves', *Tellus* **1**(3), 33–52.

Feldstein, S. B. (2000), 'The timescale, power spectra, and climate noise properties of teleconnection patterns', *Journal of Climate* **13**(24), 4430–4440.

Ferziger, J. H. & Perić, M. (1996), *Computational methods for fluid dynamics*, Vol. 3, Springer Berlin.

Fjørtoft, R. (1953), 'On the changes in the spectral distribution of kinetic energy for twodimensional, nondivergent flow', *Tellus* **5**(3), 225–230.

Flierl, G. R. (1977), 'Simple applications of McWilliams' "A note on a consistent quasigeostrophic model in a multiply connected domain"', *Dynamics of Atmospheres and Oceans* **1**(5), 443–453.

Fofonoff, N. (1954), 'Steady flow in a frictionless homogeneous ocean', *Journal of Marine Research* **13**(3), 254–262.

Frankignoul, C. (1985), 'Sea surface temperature anomalies, planetary waves, and air-sea feedback in the middle latitudes', *Reviews of Geophysics* **23**(4), 357–390.

Frankignoul, C., Czaja, A. & L'Heveder, B. (1998), 'Air-sea feedback in the North Atlantic and surface boundary conditions for ocean models', *Journal of Climate* **11**(9), 2310–2324.

Frankignoul, C., de Coëtlogon, G., Joyce, T. M. & Dong, S. (2001), 'Gulf stream variability and ocean-atmosphere interactions*', *Journal of Physical Oceanography* **31**(12), 3516–3529.

Frankignoul, C., Müller, P. & Zorita, E. (1997), 'A simple model of the decadal response of the ocean to stochastic wind forcing*', *Journal of Physical Oceanography* **27**(8), 1533–1546.

Galperin, B., Nakano, H., Huang, H.-P. & Sukoriansky, S. (2004), 'The ubiquitous zonal jets in the atmospheres of giant planets and Earth's oceans', *Geophysical Research Letters* **31**(13), L13303.

Gill, A. (1974), 'The stability of planetary waves on an infinite beta-plane', *Geophysical and Astrophysical Fluid Dynamics* **6**(1), 29–47.

Gill, A. E. (1982), *Atmosphere-ocean dynamics*, Vol. 30, Academic press.

Green, J. (1977), 'The weather during July 1976: Some dynamical considerations of the drought', *Weather* **32**(4), 120–126.

Griffa, A. & Salmon, R. (1989), 'Wind-driven ocean circulation and equilibrium statistical mechanics', *Journal of Marine Research* **47**(3), 457–492.

Hart, J. E. (1974), 'On the Mixed Stability Program for Quasi-Geostrophic Ocean Currents', *Journal of Physical Oceanography* **4**, 349–356.

Hecht, M. W., Holland, W. R. & Rasch, P. J. (1995), 'Upwind-weighted advection schemes for ocean tracer transport: An evaluation in a passive tracer context', *Journal of Geophysical Research* **100**(C10), 20763–20.

Held, I. M., Ting, M. & Wang, H. (2002), 'Northern winter stationary waves: theory and modeling', *Journal of Climate* **15**(16), 2125–2144.

Holland, W. R. (1978), 'The role of mesoscale eddies in the general circulation of the ocean-numerical experiments using a wind-driven quasi-geostrophic model', *Journal of Physical Oceanography* **8**(3), 363–392.

Hoskins, B. (1973), 'Stability of the Rossby-Haurwitz wave', *Quarterly Journal of the Royal Meteorological Society* **99**(422), 723–745.

Hoskins, B. J., James, I. N. & White, G. H. (1983), 'The shape, propagation and mean-flow interaction of large-scale weather systems', *Journal of the Atmospheric Sciences* **40**(7), 1595–1612.

Hoskins, B. J. & Valdes, P. J. (1990), 'On the existence of storm-tracks', *Journal of the Atmospheric Sciences* **47**(15), 1854–1864.

Hoskins, B., McIntyre, M. & Robertson, A. W. (1985), 'On the use and significance of isentropic potential vorticity maps', *Quarterly Journal of the Royal Meteorological Society* **111**(470), 877–946.

Hotta, D. & Nakamura, H. (2011), 'On the significance of the sensible heat supply from the ocean in the maintenance of the mean baroclinicity along storm tracks', *Journal of Climate* **24**(13), 3377–3401.

Hristova, H. G., Pedlosky, J. & Spall, M. A. (2008), 'Radiating instability of a meridional boundary current', *Journal of Physical Oceanography* **38**(10), 2294–2307.

Huang, H.-P., Kaplan, A., Curchitser, E. N. & Maximenko, N. A. (2007), 'The degree of anisotropy for mid-ocean currents from satellite observations and an eddy-permitting model simulation', *Journal of Geophysical Research: Oceans (1978–2012)* **112**(C9).

Hurrell, J. W., Kushnir, Y., Ottersen, G. & Visbeck, M. (2003), *The North Atlantic Oscillation: Climatic significance and environmental impact*, Vol. 134, American Geophysical Union.

Hurrell, J. W. & Van Loon, H. (1997), 'Decadal variations in climate associated with the North Atlantic Oscillation', *Climatic Change* **36**(3-4), 301–326.

Illari, L. & Marshall, J. C. (1983), 'On the interpretation of eddy fluxes during a blocking episode.', *Journal of Atmospheric Sciences* **40**, 2232–2242.

Inatsu, M. & Hoskins, B. J. (2004), 'The zonal asymmetry of the Southern Hemisphere winter storm track', *Journal of climate* **17**(24), 4882–4892.

Jones, S. (1979), 'Rossby wave interactions and instabilities in a rotating, two-layer fluid on a beta-plane. Part II: Stability', *Geophysical & Astrophysical Fluid Dynamics* **12**(1), 1–33.

Joyce, T. M., Kwon, Y.-O. & Yu, L. (2009), 'On the relationship between synoptic wintertime atmospheric variability and path shifts in the Gulf Stream and the Kuroshio Extension', *Journal of Climate* **22**(12), 3177–3192.

Kalnay, E., Kanamitsu, M., Kistler, R., Collins, W., Deaven, D., Gandin, L., Iredell, M., Saha, S., White, G., Woollen, J. et al. (1996), 'The NCEP/NCAR 40-year reanalysis project', *Bulletin of the American Meteorological Society* **77**(3), 437–471.

Kamenkovich, I., Berloff, P. & Pedlosky, J. (2009), 'Role of eddy forcing in the dynamics of multiple zonal jets in a model of the North Atlantic', *Journal of Physical Oceanography* **39**(6), 1361–1379.

Kelly, K. A., Small, R. J., Samelson, R., Qiu, B., Joyce, T. M., Kwon, Y.-O. & Cronin, M. F. (2010), 'Western boundary currents and frontal air-sea interaction: Gulf Stream and Kuroshio Extension', *Journal of Climate* **23**(21), 5644–5667.

Kim, K. (1978), 'Instability of baroclinic Rossby waves; energetics in a two-layer ocean', *Deep Sea Research* **25**(9), 795–814.

Knapp, P. A., Soulé, P. T. & Grissino-Mayer, H. D. (2004), 'Occurrence of sustained droughts in the interior Pacific Northwest (ad 1733-1980) inferred from tree-ring data', *Journal of Climate* **17**(1), 140–150.

Kramer, W., van Buren, M., Clercx, H. & van Heijst, G. (2006), 'β-plane turbulence in a basin with no-slip boundaries', *Physics of Fluids* **18**(2), 026603–026603.

Kushnir, Y., Robinson, W., Bladé, I., Hall, N., Peng, S. & Sutton, R. (2002), 'Atmospheric GCM response to extratropical SST anomalies: Synthesis and evaluation*', *Journal of Climate* **15**(16), 2233–2256.

Kwon, Y.-O. & Deser, C. (2007), 'North Pacific decadal variability in the community climate system model version 2', *Journal of climate* **20**(11), 2416–2433.

LaCasce, J. (2000), 'Baroclinic rossby waves in a square basin*', *Journal of Physical Oceanography* **30**(12), 3161–3178.

LaCasce, J. (2002), 'On turbulence and normal modes in a basin', *Journal of Marine Research* **60**(3), 431–460.

LaCasce, J. & Brink, K. (2000), 'Geostrophic turbulence over a slope', *Journal of Physical Oceanography* **30**(6), 1305–1324.

LaCasce, J. & Pedlosky, J. (2004), 'The instability of rossby basin modes and the oceanic eddy field*', *Journal of Physical Oceanography* **34**(9), 2027–2041.

Lee, W.-J. & Mak, M. (1996), 'The role of orography in the dynamics of storm tracks', *Journal of the Atmospheric Sciences* **53**(12), 1737–1750.

Leonard, B. (1988), 'Universal limiter for transient interpolation modeling of the advective transport equations: The ULTIMATE conservative difference scheme', *NASA Technical Memorandum* **100916**.

Levitus, S., Burgett, R. & Boyer, T. P. (1994), World ocean atlas 1994. volume 3. salinity, Technical report, National Environmental Satellite, Data, and Information Service, Washington, DC (United States).

Longuet-Higgins, M. (1965), 'Planetary waves on a rotating sphere. II', *Proceedings of the Royal Society of London. Series A. Mathematical and Physical Sciences* **284**(1396), 40–68.

Lorenz, E. N. (1955), 'Available potential energy and the maintenance of the general circulation', *Tellus* **7**(2), 157–167.

Lorenz, E. N. (1972), 'Barotropic instability of Rossby wave motion.', *Journal of Atmospheric Sciences* **29**, 258–265.

Maltrud, M. & Vallis, G. (1991), 'Energy spectra and coherent structures in forced two-dimensional and beta-plane turbulence.', *Journal of Fluid Mechanics* **228**, 321–342.

Marcus, P. S. (1993), 'Jupiter's Great Red Spot and other vortices', *Annual Review of Astronomy and Astrophysics* **31**, 523–573.

Marshall, J. (1984), 'Eddy-mean-flow interaction in a barotropic ocean model', *Quarterly Journal of the Royal Meteorological Society* **110**(465), 573–590.

Marshall, J., Adcroft, A., Hill, C., Perelman, L. & Heisey, C. (1997), 'A finite-volume, incompressible Navier Stokes model for studies of the ocean on parallel computers', *Journal of Geophysical Research: Oceans (1978–2012)* **102**(C3), 5753–5766.

Marshall, J., Johnson, H. & Goodman, J. (2001), 'A study of the interaction of the North Atlantic Oscillation with ocean circulation', *Journal of Climate* **14**(7), 1399–1421.

Marshall, J. & Shutts, G. (1981), 'A note on rotational and divergent eddy fluxes', *Journal of Physical Oceanography* **11**(12), 1677–1680.

Maximenko, N. A., Bang, B. & Sasaki, H. (2005), 'Observational evidence of alternating zonal jets in the world ocean', *Geophysical Research Letters* **32**(12).

Maximenko, N. A., Melnichenko, O. V., Niiler, P. P. & Sasaki, H. (2008), 'Stationary mesoscale jet-like features in the ocean', *Geophysical Research Letters* **35**(8), L08603.

McWilliams, J. C. (1977), 'A note on a consistent quasigeostrophic model in a multiply connected domain', *Dynamics of Atmospheres and Oceans* **1**(5), 427–441.

McWilliams, J. C. (2006), *Fundamentals of geophysical fluid dynamics*, Cambridge University Press.

Melnichenko, O. V., Maximenko, N. A., Schneider, N. & Sasaki, H. (2010), 'Quasi-stationary striations in basin-scale oceanic circulation: vorticity balance from observations and eddy-resolving model', *Ocean Dynamics* **60**(3), 653–666.

Milliff, R. F. & McWilliams, J. C. (1994), 'The evolution of boundary pressure in ocean basins', *Journal of Physical Oceanography* **24**(6), 1317–1338.

Nadiga, B. & Straub, D. (2010), 'Alternating zonal jets and energy fluxes in barotropic wind-driven gyres', *Ocean Modelling* **33**(3), 257–269.

Nadiga, B. T. (2006), 'On zonal jets in oceans', *Geophysical Research Letters* **33**(10).

Nakamura, H. (1992), 'Midwinter suppression of baroclinic wave activity in the Pacific.', *Journal of Atmospheric Sciences* **49**, 1629–1642.

Nakamura, H., Izumi, T. & Sampe, T. (2002), 'Interannual and decadal modulations recently observed in the Pacific storm track activity and East Asian winter monsoon', *Journal of Climate* **15**(14), 1855–1874.

Nakamura, H., Nishina, A. & Minobe, S. (2012), 'Response of storm tracks to bimodal Kuroshio path states south of Japan', *Journal of Climate* **25**(21), 7772–7779.

Nakamura, H. & Sampe, T. (2002), 'Trapping of synoptic-scale disturbances into the North Pacific subtropical jet core in midwinter', *Geophysical Research Letters* **29**(16), 8–1.

Nakamura, H., Sampe, T., Goto, A., Ohfuchi, W. & Xie, S.-P. (2008), 'On the importance of midlatitude oceanic frontal zones for the mean state and dominant variability in the tropospheric circulation', *Geophysical Research Letters* **35**(15).

Nakamura, H., Sampe, T., Tanimoto, Y. & Shimpo, A. (2004), 'Observed associations among storm tracks, jet streams and midlatitude oceanic fronts', *Geophysical Monograph Series* **147**, 329–345.

Nakamura, H. & Wallace, J. M. (1990), 'Observed changes in baroclinic wave activity during the life cycles of low-frequency circulation anomalies.', *Journal of Atmospheric Sciences* **47**, 1100–1116.

Nonaka, M., Nakamura, H., Taguchi, B., Komori, N., Kuwano-Yoshida, A. & Takaya, K. (2009), 'Air-sea heat exchanges characteristic of a prominent midlatitude oceanic front in the South Indian Ocean as simulated in a high-resolution coupled GCM', *Journal of Climate* **22**(24), 6515–6535.

Ogawa, F., Nakamura, H., Nishii, K., Miyasaka, T. & Kuwano-Yoshida, A. (2012), 'Dependence of the climatological axial latitudes of the tropospheric westerlies and storm tracks on the latitude of an extratropical oceanic front', *Geophysical Research Letters* **39**(5).

O'Reilly, C. H., Czaja, A. & LaCasce, J. (2012), 'The emergence of zonal ocean jets under large-scale stochastic wind forcing', *Geophysical Research Letters* **39**(11).

Panetta, R. L. (1993), 'Zonal jets in wide baroclinically unstable regions: Persistence and scale selection', *Journal of the Atmospheric Sciences* **50**(14), 2073–2106.

Pedlosky, J. (1982), 'Geophysical fluid dynamics', *New York and Berlin, Springer-Verlag, 1982. 636 p.* **1**.

Pedlosky, J. (1996), *Ocean circulation theory*, Springer Verlag.

Phillips, N. A. (1954), 'Energy transformations and meridional circulations associated with simple baroclinic waves in a two-level, quasi-geostrophic model1', *Tellus* **6**(3), 273–286.

Pierini, S., Dijkstra, H. A. & Riccio, A. (2009), 'A nonlinear theory of the Kuroshio Extension bimodality', *Journal of Physical Oceanography* **39**(9), 2212–2229.

Qiu, B. (2000), 'Interannual variability of the Kuroshio Extension system and its impact on the wintertime SST field', *Journal of Physical Oceanography* **30**(6), 1486–1502.

Qiu, B. (2003), 'Kuroshio Extension variability and forcing of the Pacific decadal oscillations: Responses and potential feedback', *Journal of Physical Oceanography* **33**(12), 2465–2482.

Qiu, B. & Chen, S. (2005), 'Variability of the Kuroshio Extension jet, recirculation gyre, and mesoscale eddies on decadal time scales', *Journal of Physical Oceanography* **35**(11), 2090–2103.

Qiu, B. & Chen, S. (2010), 'Eddy-mean flow interaction in the decadally modulating Kuroshio Extension system', *Deep Sea Research Part II: Topical Studies in Oceanography* **57**(13), 1098–1110.

Qiu, B., Schneider, N. & Chen, S. (2007), 'Coupled decadal variability in the North Pacific: An observationally constrained idealized model*', *Journal of Climate* **20**(14), 3602–3620.

Renwick, J. A. & Wallace, J. M. (1996), 'Relationships between North Pacific wintertime blocking, El Niño, and the PNA pattern', *Monthly Weather Review* **124**(9), 2071–2076.

Reynolds, R. W., Smith, T. M., Liu, C., Chelton, D. B., Casey, K. S. & Schlax, M. G. (2007), 'Daily high-resolution-blended analyses for sea surface temperature', *Journal of Climate* **20**(22), 5473–5496.

Rhines, P. B. (1975), 'Waves and turbulence on a beta-plane', *Journal of Fluid Mechanics* **69**(3), 417–443.

Rhines, P. B. (1979), 'Geostrophic turbulence', *Annual Review of Fluid Mechanics* **11**(1), 401–441.

Richards, K., Maximenko, N., Bryan, F. & Sasaki, H. (2006), 'Zonal jets in the Pacific Ocean', *Geophysical Research Letters* **33**(3).

Rossby, C.-G. et al. (1939), 'Relation between variations in the intensity of the zonal circulation of the atmosphere and the displacements of the semi-permanent centers of action', *Journal of Marine Research* **2**(1), 38–55.

Salmon, R. (1978), 'Two-layer quasi-geostrophic turbulence in a simple special case', *Geophysical & Astrophysical Fluid Dynamics* **10**(1), 25–52.

Sampe, T., Nakamura, H., Goto, A. & Ohfuchi, W. (2010), 'Significance of a midlatitude SST frontal zone in the formation of a storm track and an eddy-driven westerly jet*', *Journal of Climate* **23**(7), 1793–1814.

Sasaki, Y. N., Minobe, S. & Schneider, N. (2012), 'Decadal response of the Kuroshio Extension jet to Rossby waves: Observation and thin-jet theory', *Journal of Physical Oceanography* (2012).

Sasaki, Y. N. & Schneider, N. (2011), 'Decadal shifts of the Kuroshio Extension Jet: Application of thin-jet theory*', *Journal of Physical Oceanography* **41**(5), 979–993.

Schlax, M. G. & Chelton, D. B. (2008), 'The influence of mesoscale eddies on the detection of quasi-zonal jets in the ocean', *Geophysical Research Letters* **35**(24).

Schneider, N., Miller, A. J. & Pierce, D. W. (2002), 'Anatomy of North Pacific decadal variability', *Journal of Climate* **15**(6), 586–605.

Scott, R. B. & Arbic, B. K. (2007), 'Spectral energy fluxes in geostrophic turbulence: Implications for ocean energetics', *Journal of Physical Oceanography* **37**(3), 673–688.

Scott, R. B., Arbic, B. K., Holland, C. L., Sen, A. & Qiu, B. (2008), 'Zonal versus meridional velocity variance in satellite observations and realistic and idealized ocean circulation models', *Ocean Modelling* **23**(3), 102–112.

Shchepetkin, A. F. & McWilliams, J. C. (2005), 'The regional oceanic modeling system (ROMS): a split-explicit, free-surface, topography-following-coordinate oceanic model', *Ocean Modelling* **9**(4), 347–404.

Sheldon, L. & Czaja, A. (2013), 'Seasonal and interannual variability of an index of deep atmospheric convection over western boundary currents', *Quarterly Journal of the Royal Meteorological Society* .

Shutts, G. (1983), 'The propagation of eddies in diffluent jetstreams: Eddy vorticity forcing of blocking flow fields', *Quarterly Journal of the Royal Meteorological Society* **109**(462), 737–761.

Shutts, G. (1986), 'A case study of eddy forcing during an Atlantic blocking episode', *Advances in Geophysics* **29**, 135–162.

Simmons, A. J. & Hoskins, B. J. (1978), 'The life cycles of some nonlinear baroclinic waves', *Journal of the Atmospheric Sciences* **35**(3), 414–432.

Smith, K. S. & Vallis, G. K. (2002), 'The scales and equilibration of midocean eddies: Forced-dissipative flow', *Journal of Physical Oceanography* **32**(6), 1699–1720.

Smith, T. M. & Reynolds, R. W. (2004), 'Improved extended reconstruction of SST (1854-1997)', *Journal of Climate* **17**(12), 2466–2477.

Sokolov, S. & Rintoul, S. R. (2007), 'Multiple jets of the Antarctic Circumpolar Current south of Australia*', *Journal of Physical Oceanography* **37**(5), 1394–1412.

Son, S.-W., Ting, M. & Polvani, L. M. (2009), 'The effect of topography on storm-track intensity in a relatively simple general circulation model', *Journal of the Atmospheric Sciences* **66**(2), 393–411.

Taguchi, B., Nakamura, H., Nonaka, M. & Xie, S.-P. (2009), 'Influences of the Kuroshio/Oyashio Extensions on air-sea heat exchanges and storm-track activity as revealed in regional atmospheric model simulations for the 2003/04 cold season*', *Journal of Climate* **22**(24), 6536–6560.

Taguchi, B., Xie, S.-P., Schneider, N., Nonaka, M., Sasaki, H. & Sasai, Y. (2007), 'Decadal variability of the Kuroshio Extension: Observations and an eddy-resolving model hindcast*', *Journal of Climate* **20**(11), 2357–2377.

Thompson, A. F. & Young, W. R. (2007), 'Two-layer baroclinic eddy heat fluxes: Zonal flows and energy balance', *Journal of the Atmospheric Sciences* **64**(9), 3214–3231.

Treguier, A. & Panetta, R. (1994), 'Multiple zonal jets in a quasigeostrophic model of the Antarctic Circumpolar Current', *Journal of Physical Oceanography* **24**(11), 2263–2277.

Trenberth, K. E. & Caron, J. M. (2001), 'Estimates of meridional atmosphere and ocean heat transports', *Journal of Climate* **14**(16), 3433–3443.

Trenberth, K. E. & Chen, S.-C. (1988), 'Planetary waves kinematically forced by Himalayan orography', *Journal of the Atmospheric Sciences* **45**(20), 2934–2948.

Trenberth, K. E. & Stepaniak, D. P. (2001), 'Indices of El Niño evolution', *Journal of Climate* **14**(8), 1697–1701.

Valdes, P. J. & Hoskins, B. J. (1989), 'Linear stationary wave simulations of the time-mean climatological flow', *Journal of the Atmospheric Sciences* **46**(16), 2509–2527.

Vallis, G. K. (2006), *Atmospheric and oceanic fluid dynamics: fundamentals and large-scale circulation*, Cambridge University Press.

Vallis, G. K. & Maltrud, M. E. (1993), 'Generation of mean flows and jets on a beta plane and over topography', *Journal of Physical Oceanography* **23**, 1346–1346.

van Sebille, E., Kamenkovich, I. & Willis, J. K. (2011), 'Quasi-zonal jets in 3-D Argo data of the northeast Atlantic', *Geophysical Research Letters* **38**(2), L02606.

Veronis, G. (1970), Effect of fluctuating winds on ocean circulation, *in* 'Deep Sea Research and Oceanographic Abstracts', Vol. 17, Elsevier, pp. 421–434.

Visbeck, M., Chassignet, E. P., Curry, R. G., Delworth, T. L., Dickson, R. R. & Krahmann, G. (2003), 'The ocean's response to North Atlantic Oscillation variability', *Geophysical Monograph - AGU* **134**, 113–146.

Vivier, F., Kelly, K. A. & Thompson, L. A. (2002), 'Heat budget in the Kuroshio Extension region: 1993-99', *Journal of Physical Oceanography* **32**(12), 3436–3454.

Wang, J., Spall, M. A., Flierl, G. R. & Malanotte-Rizzoli, P. (2012), 'A new mechanism for the generation of quasi-zonal jets in the ocean', *Geophysical Research Letters* **39**(10).

Wang, J. & Vallis, G. K. (1994), 'Emergence of fofonoff states in inviscid and viscous ocean circulation models', *Journal of Marine Research* **52**(1), 83–127.

Wunsch, C. (1999), 'The interpretation of short climate records, with comments on the North Atlantic and Southern Oscillations', *Bulletin of the American Meteorological Society* **80**, 245–256.

Appendices

Appendix A

Numerical quasigeostrophic basin model

The numerical basin model used in this study is the same as that used by LaCasce and Pedlosky (2004), written by Joe LaCasce[1]. The model solves the two-layer non-dimensional modal potential vorticity equations, (2.24) and (2.23), with forcing due to a (non-dimensional) wind-stress curl forcing in the surface layer, W_{Ek}, and dissipation via bottom friction in the lower layer, with damping coefficient r_2, and a weak Rayleigh damping in the upper layer, with damping coefficient r_1. With these terms the modal potential vorticity equations take the form

$$\begin{aligned}\frac{\partial q_\phi}{\partial t} + J(\phi, q_\phi) + h_1 h_2 J(\tau, q_\tau) + \beta\frac{\partial \phi}{\partial x} = \\ W_{Ek} + h_1 h_2 (r_2 - r_1)\nabla^2\tau - (h_1 r_1 + h_2 r_2)\nabla^2\phi,\end{aligned} \tag{A.1}$$

$$\begin{aligned}\frac{\partial q_\tau}{\partial t} + J(\phi, q_\tau) + J(\tau, q_\phi) + (h_1 - h_2)J(\tau, q_\tau) + \beta\frac{\partial \tau}{\partial t} = \\ \frac{W_{Ek}}{h_1} + (r_2 h_1 - r_1 h_2)\nabla^2\tau + (r_2 - r_1)\nabla^2\phi.\end{aligned} \tag{A.2}$$

The model is a square basin model with N^2 grid points, the non-dimensional scale of the basin is π.

At each time step the potential vorticities is inverted to solve for the corresponding streamfunction. To do this the potential vorticities and streamfunctions are decomposed

[1]Thanks Joe!

using discrete sine transforms, as shown here for the baroclinic mode:

$$q_\tau^{n,m} = \frac{2}{N} \sum_{k=1}^{N-1} \sum_{l=1}^{N-1} \hat{q}_\tau^{k,l} \sin\left(\frac{nk}{N}\right) \sin\left(\frac{ml}{N}\right), \tag{A.3}$$

$$\tau^{n,m} = \frac{2}{N} \sum_{k=1}^{N-1} \sum_{l=1}^{N-1} \hat{\tau}^{k,l} \sin\left(\frac{nk}{N}\right) \sin\left(\frac{ml}{N}\right), \tag{A.4}$$

where the indices n, m are the grid point in the x, y directions respectively, and similarly the indices k and l are the integer wave numbers in the x and y directions. The hat indicates the Fourier transform in wavenumber space. The streamfunction is obtained from the potential vorticity by solving equation (2.26). Using finite differences, the Laplacian is represented by a five-point stencil around each grid point,

$$\begin{aligned} q_\tau^{n,m} &= (\nabla^2 - F)\tau^{n,m} \\ &= \frac{1}{(\Delta x)^2}(\tau^{n+1,m} + \tau^{n-1,m} + \tau^{n,m+1} + \tau^{n,m-1} - (4 + (\Delta x)^2 F)\tau^{n,m}), \end{aligned} \tag{A.5}$$

where Δx is the uniform grid spacing. Inserting the Fourier decompositions, (A.3) and (A.4), into equation (A.5), rearranging and equating the terms within the summation gives the Fourier transform of the streamfunction in terms of the Fourier transform of the potential vorticity,

$$\hat{\tau}^{k,l} = \left(\frac{(\Delta x)^2}{2\cos(k/N) + 2\cos(l/N) - 4 - (\Delta x)^2 F}\right) \hat{q}_\tau^{k,l}. \tag{A.6}$$

Thus, once the the Fourier transform of the potential vorticity is computed (using a standard "Fast Fourier Transform" algorithm), the components are multiplied by the factor in equation (A.6) and then the inverse Fourier transform is computed to return the streamfunction. The process is repeated for the barotropic potential vorticity.

The advection terms are calculated using an "upwinding" scheme (e.g. Leonard, 1988), which has been used in several previous idealised basin studies (e.g. Becker and Salmon, 1997; LaCasce, 2002). To simplify the calculation the modal streamfunctions are converted to the layer streamfunctions, using the relations in (2.21) and (2.22), so the terms which we compute are $\mathbf{u}_1 \cdot \nabla q_1$ and $\mathbf{u}_2 \cdot \nabla q_2$. In one-dimension the advection term is $u\frac{\partial q}{\partial x}$, where the velocity is calculated by finite differencing the streamfunction field. The derivative of the potential vorticity is estimated by fitting a cubic polynomial using the grid points on either side of the grid point, n, and a fourth grid point in the upstream direction, this

is a third-order "upwind" scheme (e.g. Ferziger and Peric, 1996). In one dimension the approximation of the advective term, for positive u, at grid point n is

$$\begin{aligned} u^n \left(\frac{\partial q}{\partial x}\right)^n &= u^n \left(\frac{2q^{n+1} + 3q^n - 6q^{n-1} + q^{n-2}}{6(\Delta x)}\right) \\ &= u^n \left(\frac{q^{n+1} - q^{n-1}}{2(\Delta x)} - \frac{q^{n+1} - 3q^n + 3q^{n-1} - q^{n-2}}{6(\Delta x)}\right) \end{aligned} \tag{A.7}$$

and similarly, where u is negative,

$$u^n \left(\frac{\partial q}{\partial x}\right)^n = u^n \left(\frac{q^{n+1} - q^{n-1}}{2(\Delta x)} - \frac{q^{n+2} - 3q^{n+1} + 3q^n - q^{n-1}}{6(\Delta x)}\right). \tag{A.8}$$

The first term on the right hand side of equations (A.7) and (A.8) is the first-order central difference approximation to the first derivative and the second term is a truncation error essentially corresponding to a fourth derivative term:

$$u^n \left(\frac{\partial q}{\partial x}\right)^n = u^n \left(\frac{q^{n+1} - q^{n-1}}{2(\Delta x)}\right) + \kappa \left(\frac{\partial^4 q}{\partial x^4}\right). \tag{A.9}$$

The truncation error therefore corresponds to an implicit biharmonic diffusion term on the potential vorticity, with the coefficient scaling with the velocity and grid spacing:

$$\kappa = \frac{|u|(\Delta x)^3}{16}. \tag{A.10}$$

The implicit biharmonic diffusion removes potential vorticity at small scales and ensures numerical stability. As a result, it is not necessary to apply an eddy diffusion term explicitly in any of the simulations carried out for the present study. To some extent this is an advantage of using this advection scheme because an explicit eddy diffusion term requires the application of additional boundary conditions, for example "no-slip", "free slip" or "hyper-slip", as in many idealised model studies. The circulation properties in idealised basin simulations has been shown to be sensitive to the application of a specific boundary condition (e.g. Cummins, 1992; Wang and Vallis, 1994; Pedlosky, 1996). Hecht *et al.* (1995) demonstrated that third-order upwind advection proves more accurate than advective schemes with explicit harmonic and biharmonic eddy diffusivity at advecting a tracer in an idealised barotropic QG basin. For our 256×256 grid simulations presented in this thesis typical values of the diffusion coefficient are $\kappa \approx 2 \times 10^{10}\mathrm{m}^4\mathrm{s}^{-1}$, which is comparable

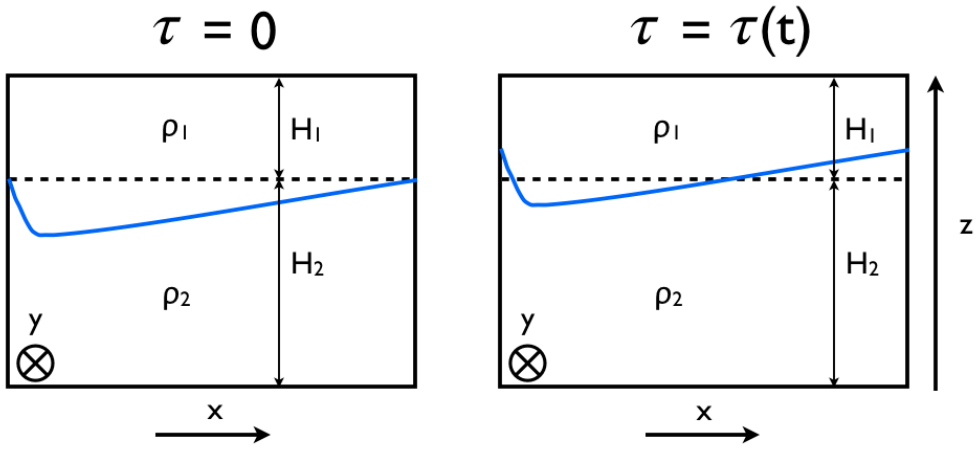


Figure A.1: Schematic cross-section through the centre of a 2-layer mean subtropical gyre, where the blue line is the interface. On the left, the $\tau = 0$ boundary condition means the volume (and hence mass) of each layer is not conserved. On the right, the interface height is allowed to vary on the boundary and mass is conserved for the same mean flow.

with other idealised QG basin studies that employ emphexplicit biharmonic diffusion (e.g. Holland, 1978).

Following their calculation, the advection terms are converted to their equivalent modal values and the potential vorticity equations are stepped forward in time. A third-order Adams Bashforth time stepping method is employed to calculate the potential vorticity at time step i, denoted q^i:

$$q^{i+1} = q^i + \frac{\Delta t}{12}\left(23f^i - 16f^{i-1} + 5f^{i-2}\right), \tag{A.11}$$

where Δt is the model time step and the forcing terms, f^i, represent the forcing, dissipation and advection terms in equations (A.1) and (A.2) grouped together at time step i. This has the effect of fitting a cubic polynomial interpolation in time and acts to smooth the progression and ensure numerical stability.

In addition to the no-flow condition on the walls of the basin, we must also include a boundary condition on the baroclinic streamfunction. McWilliams (1977) identified that the interfacial layer in a two-layer model must be allowed to vary on the boundary to be dynamically consistent will the principles of mass conservation. Previous QG basin studies (e.g. Longuet-Higgins, 1965) assumed $\tau = 0$ on the boundary, which fails to conserve the total mass in each layer of the model, as illustrated in Figure A.1. The correct "mass-

conserving" boundary condition on the baroclinic streamfunction is

$$\frac{\partial}{\partial t} \iint_{\text{basin}} \tau \, dxdy = 0, \tag{A.12}$$

and $\tau = \tau(t)$ on the boundary, to ensure there is no normal flow through the boundary. The rigid-lid approximation implies that the boundary condition on the barotropic streamfunction can be set to zero.

To implement the condition along the boundary, the model follows the method of Milliff and McWilliams (1994). The streamfunction is partitioned as

$$\tau = \tau_{\text{int}} + c(t)\tau_{\text{bound}} \tag{A.13}$$

where the interior streamfunction, τ_{int}, is determined from the basin potential vorticity as previously described. On the boundary $\tau_{\text{int}} = 0$ (which is guaranteed through use of sine transforms to determine the streamfunction) and the boundary function, τ_{bound}, is found by solving

$$\left(\nabla^2 - F\right) \tau_{\text{bound}} = 0, \tag{A.14}$$

where $\tau_{\text{bound}} = 0$ on the boundary. Therefore, τ_{bound} decreases away from the boundary with a length scale of the deformation radius. From the boundary condition in A.12, the time variability must be

$$\frac{\partial}{\partial t} \iint_{\text{basin}} \left(\tau_{\text{int}} + c(t)\tau_{\text{bound}}\right) dxdy = 0. \tag{A.15}$$

The time evolution of the boundary streamfunction, which is initally zero at rest, is then calculated from

$$\frac{dc(t)}{dt} = -\frac{\dfrac{\partial}{\partial t} \iint_{\text{basin}} \tau_{\text{int}} \, dxdy}{\iint_{\text{basin}} \tau_{\text{bound}} \, dxdy}. \tag{A.16}$$

Milliff and McWilliams (1994) showed that the fluctuation of the baroclinic streamfunction at the boundary can be thought to effectively parameterise the pressure adjustment by kelvin waves along the boundary. Kelvin waves are infinitely fast in the QG approximation but Milliff and McWilliams found the characteristics of the evolution due to boundary

fluctuation to be comparable to a shallow water model that resolves Kelvin waves.

Appendix B

Rossby wave instability

Rossby wave instability was first investigated by Lorenz (1972) in an attempt to explain the unpredictable nature of large-scale atmospheric motion in numerical simulations. Lorenz found a stationary Rossby wave to be susceptible to barotropic instability in a homogenous fluid on the β-plane, the governing equation being the barotropic QG PV equation

$$\frac{\partial}{\partial t}\nabla^2\psi + J(\psi, \nabla^2\psi) + \beta\frac{\partial\psi}{\partial x} = 0. \tag{B.1}$$

In the corresponding problem on a sphere, Rossby-Haurwitz waves were shown to be similarly unstable by Hoskins (1973). Gill (1974) extended Lorenz's study to investigate the stability of propagating barotropic Rossby waves and found them to be unstable regardless of the scale or amplitude. The nature of the instability was found to depend strongly on the parameter M which describes the ratio of the velocity scale of the Rossby wave, U, to its phase velocity, c_ϕ:

$$M = \frac{U}{c_\phi} = \frac{U}{\beta L^2}, \tag{B.2}$$

where L is the Rossby wave scale. The ratio M is therefore a measure of the relative effect of the non-linear inertial effects to the β-effect. Gill found that for large M, the barotropic Rossby waves are susceptible to barotropic instability due to the strong horizontal velocity shear, whereas for small M the Rossby waves become unstable through a resonant interaction between a triad of Rossby waves[1]. The barotropic instability feeds off the kinetic energy of the Rossby waves, which can be illustrated by constructing the energy equation for

[1]Referred to as "Rayleigh type" and "resonant type" instability by Gill.

the perturbation of the barotropic Rossby wave. Taking the basic state to be the barotropic Rossby wave

$$\Psi = \frac{U}{k}\sin(k[x - C_\phi t]), \tag{B.3}$$

then, linearising (B.1) around this basic state, following the procedure from (2.42) for the two-layer model, gives the perturbation equation for the barotropic Rossby wave instability:

$$\frac{\partial}{\partial t}\nabla^2\psi + V(x)\frac{\partial}{\partial y}(\nabla^2\psi + k^2\psi) + \beta\frac{\partial\psi}{\partial x} = 0, \tag{B.4}$$

where ψ is the perturbation streamfunction as before and $V(x)$ is the velocity of the basic state,

$$V(x) = U\cos(k[x - C_\phi t]). \tag{B.5}$$

Multiplying (B.1) by $-\psi$ and integrating over one cycle of the Rossby wave, presuming the perturbation to be periodic in space (or dying away from a central region), yields the perturbation energy equation:

$$\frac{\partial}{\partial t}\iint\limits_{\text{cycle}}\frac{1}{2}(\nabla\psi)^2\,dx\,dy = \iint\limits_{\text{cycle}}\frac{dV(x)}{dx}\frac{\partial\psi}{\partial x}\frac{\partial\psi}{\partial y}\,dx\,dy = -\iint\limits_{\text{cycle}}u'v'\frac{dV(x)}{dx}\,dx\,dy \tag{B.6}$$

The left hand side is kinetic energy of the perturbation, which is also the total energy of the perturbation since there is no stratification and hence no potential energy in the single-layer barotropic model. The right hand side is the product of the perturbation velocities, the so-called Reynolds stresses, and the horizontal velocity shear of the Rossby wave. The perturbation velocities works on the velocity shear of the basic state to extract kinetic energy. When the velocity shear is weak the term on the right hand side is small and the perturbation growth is limited to the triad sets of Rossby waves described by Gill.

The work on the stability of barotropic Rossby waves of Lorenz and Gill was extended to include stratification in a two-layer system by Kim (1978) and Jones (1979). Both authors considered the stability of a baroclinic Rossby plane wave using the two-layer QG equations, (2.18) and (2.19). Following Gill, Jones demonstrated that for very weak waves with $M \ll 1$ baroclinic Rossby waves are always unstable to resonant triads of Rossby waves. Kim considered the instability of larger amplitude baroclinic Rossby waves, in the limit $M \geq 1$, which is dominated by a mixed mode instability, consisting of a combination of barotropic and baroclinic instability mechanisms. An important non-dimensional parameter in deter-

mining the instability characteristics of baroclinic Rossby waves is F, as defined in (2.33), but here we take L to be the length scale of the wave. With $F < 1$, barotropic instability occurs in both layers independently and simultaneously, with both layers essentially being decoupled and the instability characteristics are those found by Gill for barotropic Rossby waves in each layer. For $F > 1$, the coupling between the layers becomes important and the flow is baroclinically unstable. The barotropic interaction becomes less significant with increasing F. The "mixed mode" nature of the instability, when $F \approx 1$ was the focus of Kim and Jones' studies but both authors noted that in the large F limit the instability tends towards the baroclinic instability of the uniform meridional baroclinic flow, described in section 2.1.5. It is useful to note that the "mixed mode" instability refers to the type of instability mechanism and not the type of instability wave generated. It is clear from section 2.1.5 that the most baroclinically unstable wave will have both baroclinic and barotropic wave components.

The scale partition between barotropic and baroclinic instability, as highlighted by Hart (1974), is best illustrated in the perturbation energy equation (following Kim (1978)) that has been linearised around a meridionally orientated baroclinic Rossby wave:

$$\Psi_1 = \frac{U}{k}\sin(k[x - C_\tau t]), \tag{B.7}$$

$$\Psi_2 = -\frac{U}{k}\sin(k[x - C_\tau t]). \tag{B.8}$$

The velocity fields of the basic state are $V_1 = -V_2 = U\cos(k[x - C_\tau t])$. Following the method leading to equation (2.63), by integrating over one cycle of the basic wave and presuming the perturbation to be periodic, the energy equation for the perturbation is obtained:

$$\begin{aligned}\frac{\partial}{\partial t}\iint\limits_{\text{cycle}}\left(\frac{1}{2}(\nabla\psi_1)^2 + \frac{1}{2}(\nabla\psi_2)^2 + \frac{F}{2}(\psi_1 - \psi_2)^2\right)dx\,dy \\ = \iint\limits_{\text{cycle}} F(V_1 - V_2)(\psi_1 - \psi_2)\frac{\partial\psi_2}{\partial x}\,dx\,dy \\ + \iint\limits_{\text{cycle}}\left(\frac{dV_1}{dx}\frac{\partial\psi_1}{\partial x}\frac{\partial\psi_2}{\partial y} + \frac{dV_2}{dx}\frac{\partial\psi_2}{\partial x}\frac{\partial\psi_2}{\partial y}\right)dx\,dy.\end{aligned} \tag{B.9}$$

Where $F = L^2/{L_d}^2$ here is the ratio of the Rossby wave scale to the deformation radius. This equation is similar to the perturbation energy equation (2.63), the integral on the

left hand side describes the rate of change of the combined kinetic and potential energy. The first integral on the right hand side is the rate at which the instability is extracting available potential energy from the basic state Rossby wave through baroclinic instability, equivalent to the integral on the right hand side of (2.63). The second integral on the right hand side is the rate at which energy is being extracted from the horizontal velocity shear of the Rossby wave, each layer being equivalent to the right hand side of the equivalent energy equation for a barotropic Rossby wave described by equation (B.6). For $F \ll 1$, the barotropic instability of the Rossby waves dominates and the perturbations in each layer are essentially decoupled. The case where $F \approx 1$ is the case studied by Kim in which there is a strong component of both baroclinic and barotropic instability mechanisms. For $F \gg 1$ the barotropic instability is negligible and equation (B.9) becomes equivalent to the energy equation (2.63), which describes the instability of a uniform baroclinic flow.

The large F limit was the focus of the study by LaCasce and Pedlosky (2004). In their study, LaCasce and Pedlosky considered the instability of large-scale Rossby basin modes and the subsequent eddy field. The results complemented the previous studies of Kim and Jones and considered the importance of the non-dimensional parameter Z, which is the ratio between the time for a baroclinic Rossby wave to cross the ocean basin and the characteristic unstable growth time. For small Z, the instability is weak the waves are able to cross the basin before succumbing to the instability, while for large Z the instability closely resembles baroclinic instability and the growth time is short enough for the instability to significantly distort the waves. Figure B.1 is from LaCasce and Pedlosky (2004) and shows the evolution of a two-layer basin model initialised with the $n = 3$ basin mode for $Z = 5$. The wave quickly succumbs to baroclinic instability and at later times there is a significant barotropic eddy field and no trace remains of the initial basin mode. The similarity of the Rossby basin mode instability, for $F \gg 1$, to the baroclinic instability of uniform meridional background shear (as discussed in section 2.1.5) is confirmed by the linear scaling of the measured growth rate with $F^{1/2}$, which is in agreement with the maximum growth rate predicted by equation (2.59), as shown in Figure 3.14.

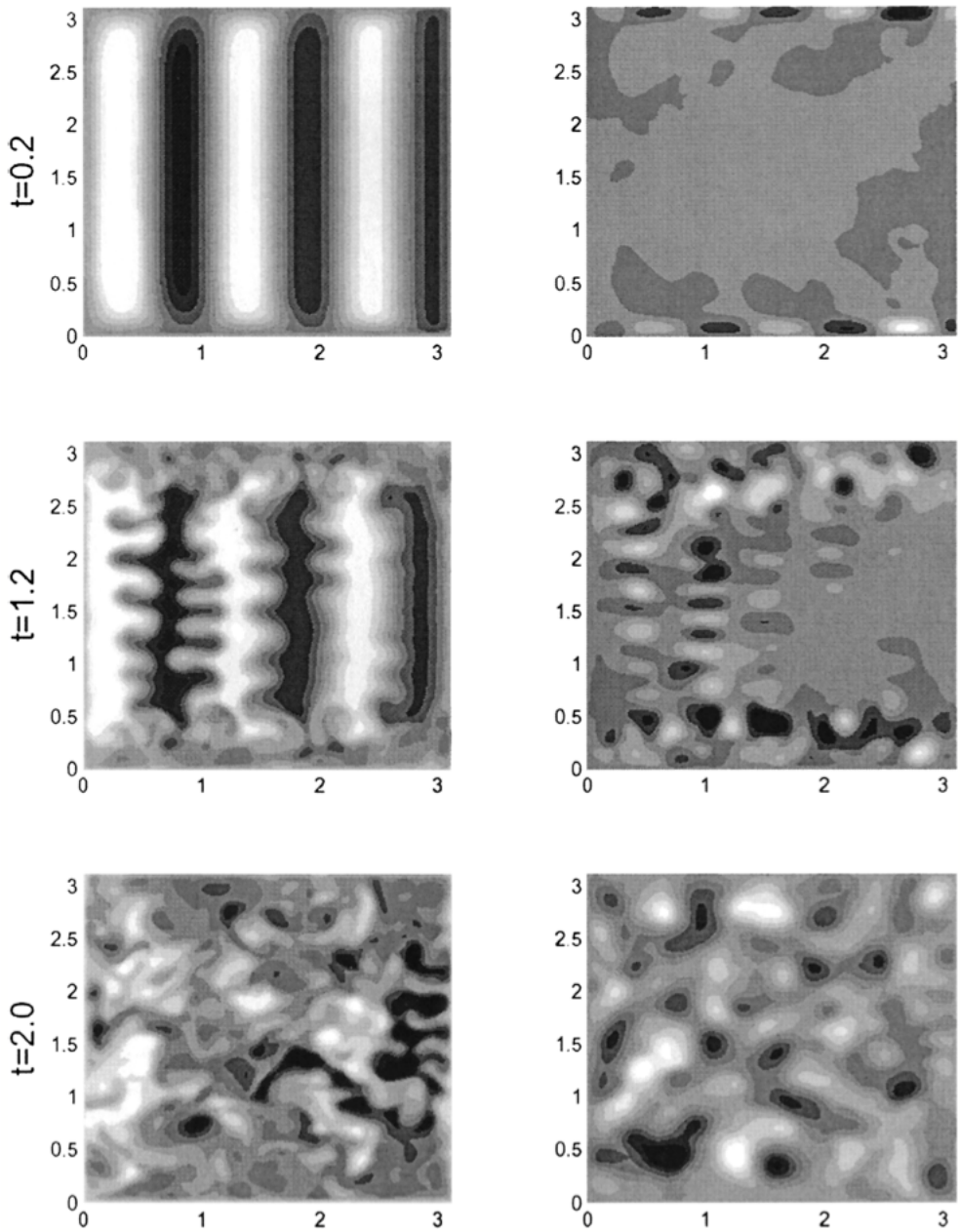


Figure B.1: The plots show the evolution of the spin-down simulations of the instability of the $n = 3$ basin mode for $Z = 5$. The baroclinic streamfunction is on the left and the barotropic streamfunction on the right. The instability of the initial baroclinic basin mode generates a field of deformation scale barotropic eddies. All units are non-dimensional. (From LaCasce and Pedlosky (2004)).